DEPARTAMENTO DE FÍSICA
UNIVERSIDAD TÉCNICA FEDERICO SANTA MARIA

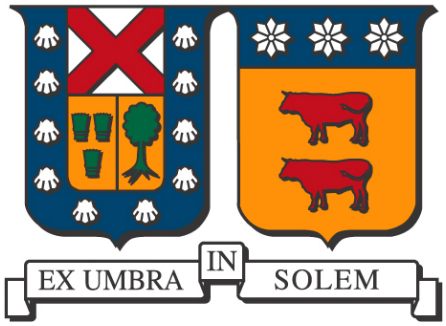

A thesis submitted to the
Physics Department as part of the requirements for the degree of
Doctor en Ciencias, mención en Física

Modern detectors to study the Standard Model and beyond

Author:
Gerardo Vásquez Arenas

Supervisor:
Professor Sergey Kuleshov

Valparaiso 2018

Abstract

The needs for experimental proof of physics beyond the Standard Model (SM) and the Dark Matter theories leads us to develop new detectors for high energy and high luminosity experiments. In this context, ATLAS with the muon upgrade (New Small Wheel project in particular) is an example of new detector technology designed for the High Luminosity LHC (HL-LHC). A big challenge is imposed on the conventional gaseous detectors used for muon tracking and triggering. The high rate environment conditions prevailing in HL-LHC will push the detectors to fulfill stringent requirements in terms of time and spatial resolution.

A search for Dark Matter experiment, called NA64 and located in one of the exit lines from the Super Proton Synchrotron (SPS) facilities at CERN, provides another example of the need for a new generation of detectors. The NA64 is looking specifically for Dark Matter on invisible or visible decays of dark photons. Such detection requires a delicate understanding of every single event and a highly pure electron beam.

For these two experiments, a team from the Physics Department of the Universidad Santa Maria (USM) has built two detectors; a small-Strip Thin Gap Chamber (sTGC) and a compact calorimeter with fast scintillator crystals LYSO.

In this dissertation, we first present the novel gaseous detector sTGC and the construction method. A gain uniformity measurement is shown as well as its stability under a high rate environment condition. These two tests are presented as a quality control after the sTGC Module 0 is built. Two beam tests are carried out to study spatial resolution of the 3.2 mm strips and pad timing performance. Both are new features to provide fast trigger for the Region of Interest.

In the second part, we focus on spectroscopy studies on the new Gamma Irradiation Facility (GIF++) at CERN. A method of peak identification using Wavelets is shown as well as fast algorithm to reconstruct pile-up events. Spectra of different attenuation filters from GIF++ are shown with estimated attenuation factors.

In the last chapter, we present a particle identification technique as a solution to the beam contamination in the NA64 experiment. A brief explanation of the dark photon measurements is shown. Afterwards we show results of hadron suppression level from different detectors using synchrotron radiation as particle identification technique. Lastly we show the first measurements of dark photon invisible decays where no dark photon-strahlung interaction is found so far with 10^9 events on target.

To my parents, who tougth me that the power of will is everything.
A mi padres, quienes me enseñaron que el poder de la voluntad lo es todo.

“ Fais de ta vie un rêve et d’un rêve, une réalité”
- Antoine de Saint-Exupéry (Le petit prince)

Agradecimientos

Todo el presente trabajo no seria posible sin el financiamiento por CONICYT con su programa Doctorado Nacional 2013, beca DGIP de estadia, programa CONICYT Anillo ACT1410 y beca PIIC.

Quisiera agradecer a mi tutor Sergey Kuleshov por la oportunidad que me brindo de poder trabajar en el desarrollo de estos detectores, asi tambien como la participacion en la etapa temprana del experimento NA64. Tambien quisiera agradecer por todos los consejos profesionales a George Mikenberg y sus ensenanzas acerca de su mas grande tesoro (TGC). Del mismo modo no puedo dejar afuera a Vladimir Poliakov quien siempre estuvo para ayudarme en todo lo que quisiera saber sobre el experimento NA64 y cada uno de los detectores presentes. A Sergey Gninenko por discusiones de fisica y el futuro de las nuevas generaciones.

Quisiera incluir a tantos personajes que conoci en CERN, tantas experiencias compartidas. Quisiera agradecer la paciencia y la grata compania de Renat Dusaev durante los 3 meses que estuvimos ensamblando los calorimetros hadronicos.

Respecto a mis colegas de laboratorio no puedo decir mas que muchas gracias por cada una de sus enseñanzas de electronica, han sido muchos anos desde que entre a la puerta del laboratorio con ansias de poder aprender que hacian todas aquellas maquinas. Agradecer a Rimsky Rojas, Pablo Ulloa, Rene Rios, David Kujumyiam (o como se escriba) y a Orlando Soto, han sido parte fundamental de mi desarrollo como fisico experimental.

Quiero agredecer a mis amigos Jorge Lopez, Sebastian Tapia y Victor Vergara por tantos consejos y por ayudarme a ganar confianza en mi mismo. Agredecer a mis amigos de Rancagua que de una u otra forma han aportado a continuar mis estudios, siempre han estado presente en todo momento.

No tengo forma de poder agradecer en palabras por el enorme apoyo que he sentido desde pequeño por mi gran hermano y amigo Patricio Vasquez, aquel que siempre ha creido en mi y me a empujado a continuar cada una de las metas de mi vida. Quiero dar las gracias a mis padres que con mucho esfuerzo hicieron posible que este niño nunca dejara de soñar y menos de hacerlo en grande. Agradecer por todo ese amor y apoyo que me ha permitio creer en mi. Por ultimo y no por eso menos importante, quisiera agradecer a esa persona que ha estado presente desde el comienzo de esta tesis. Quisiera agredecer por toda su paciencia y apoyo. Quisiera agradecer por todos sus consejos profesionales como personales. Quisiera agredecer al descubrimiento mas importante de mi tesis... aquella niña del vestido azul que esta en el faro del lago esperando. Gracias por todo tu apoyo mi querida Claire Holman.

Contents

1. Introduction

The successful discovery of the Higgs boson[1, 2] dit not only confirm once again the Standard Model, it also opened a new era of particle physics and let us wonder what is beyond. This new era has pushed the physicists to think on new interactions, new particles and to build new accelerators and detectors. The new technology must be able to search for signatures of new particles within a large background. Many interactions of particles per second hide in the deepest, portals to new discoveries. We have entered a new era in search of small details of a large painting.

The Large Hadron Collider, which helped to discover the Higgs boson, will increase its luminosity to a $5 \times 10^{34}\,\mathrm{cm}^{-2}\mathrm{s}^{-1}$, 5 times higher than its design value. This increase in luminosity represents a new challenge for the muon triggering and tracking with ATLAS spectrometer. High energy and high luminosity collisions mean that detectors will be exposed to high radiation background, especially in the forward region. The detector system in charge of this task is the muon spectrometer (MS), a key component to search for new particles via lepton channels. These channels are very important and of a great concern as they provide clean signals over enormous QCD background.

Currently the ATLAS MS plays an important role for the Level-1 Trigger, the first level selection of important collisions. The MS covers the η region of $|\eta| < 1.0$ (barrel) whereas the end-cap system covers the $1.0 < |\eta| < 2.7$ for muon tracking and $1.0 < |\eta| < 2.4$ for Level-1 trigger. The Level-1 muon trigger in the end-cap region is based on track segments in the TGC chambers of the middle muon station (End-cap Middle Layer, EML) located after the end-cap toroid magnet (see Figure 1.1a).

The transverse momentum, p_T, of the muon is determined by the angle of the segment with respect to the direction pointing to the interaction point. A significant part of the muon trigger rate in the end-caps is background. Low energy particles, mainly protons, generated in the material located between the Small Wheel and the EM station, produce fake triggers by hitting the end-cap trigger chambers at an angle similar to the one of real high p_T muons. An analysis of 2012 data demonstrates that approximately 90% of the muon triggers in the end-caps are fake[3]. As a consequence, the rate of the Level-1 muon trigger in the end-cap is eight to nine times higher than the one in the barrel region. The Figure 1.1b shows the muon track segments reconstructed via Level-1 trigger compared with segments reconstructed off-line. Only less than 10% of triggered muons are associated with off-line muons. The situation cannot be extended to the high luminosity condition, as the Level-1 trigger bandwidth cannot exceed 100 kHz (including calorimeter trigger) and simultaneously select high momentum muons in an effective way.

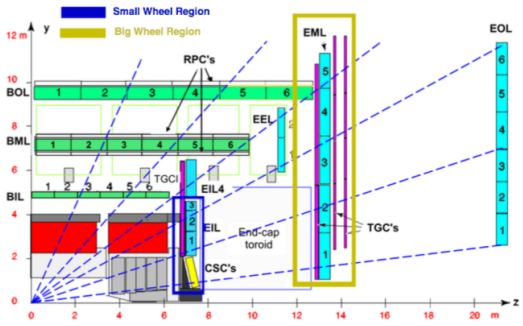

(a) A side view of 1/4 of ATLAS detector

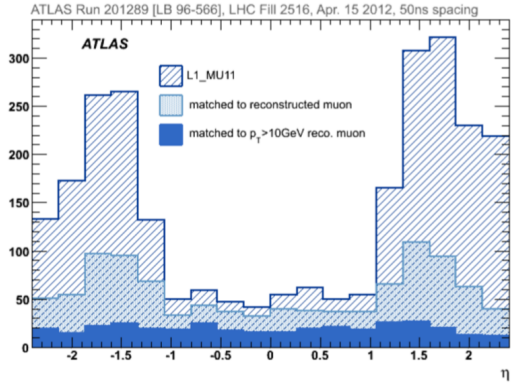

(b) Distribution of Lv-1 RoI η passing the Muon $p_T > 10$ threshold.

Figure 1.1

To benefit from the LHC upgrades and to face the aforementioned challenges in muon tracking and trigger system, ATLAS will upgrade part of the end-cap region detectors, precisely the Small Wheel, and it will be replaced by the New Small Wheel (NSW) to fulfill the followings criteria:

- Efficiency $> 97\%$ at $p_T > 10\,\text{GeV}$.
- Online pointing accuracy of 1 mrad (currently 10 mrad).
- Timing: Capable of LHC bunch crossing identification (25 ns).
- Operate with radiation background up to $15\,\text{kHz}\,\text{cm}^{-2}$.
- Ageing: No degradation up to an accumulated charge of $1\,\text{C/cm}^2$ (for the $3000\,\text{fb}^{-1}$ integrated luminosity).

The NSW employs eight layers of MicroMegas detectors (MM) and eight layers of small-strip Thin Gap Chambers (sTGC). This configuration copes with the highest rates expected after the LHC upgrade (Phase-II) and enhances the performance of the forward muon system by adding trigger functionality to the first muon station. The newly developed MM detector[4] will be the primary precision tracker with spatial resolution lower than 100 µm independent of track incident angle. The sTGC will be the primary trigger detector featuring bunch crossing (BC) identification capability and angular resolution for online reconstructed segments lower than 1 mrad[5]. The detector is also characterized by good spatial resolution for the offline tracking using the precision coordinate (readout strips) and is based on proven TGC technology, adding pads for muon track identification and readout region definition.

In Chapter 2, we focus on the characterization of the novel gaseous detector sTGC and shows the results of several tests to prove the characteristics requested by the ATLAS upgrade. Related to the same upgrades on the LHC, Chapter 3 is focused on the new

Gamma Irradiation Facility (GIF++) where spectroscopy studies were performed. This new facility has been designed to test all the new gaseous detectors which will be part of the upgrades. It features a high intensity Cesium-137 source of 13.3 TBq, easily capable of reproducing the high background expected for the HL-LHC.

In Chapter 4 we move to a new experiment located in one of the exit lines of the LHC pre-accelerator, the Super Proton Synchrotron (SPS).

The SPS can provide an electron beam of 10-300 GeV from the primary proton beam at 400 GeV. To produce such type of particles, $\simeq 10^{12}$ protons hit a Beryllium target (T2), charged and neutral particles are produced, charged ones are deflected by magnets and the neutral particles (mostly photons) are converted into electron-positron pairs by hitting a thin lead layer. Afterwards the electrons are selected by another dipole magnet with an intensity of $\simeq 10^6$. The electron beam is planned to be used by the NA64 experiment (formerly proposal P348), an experiment searching for a light boson (< 1 GeV) which can interact with ordinary and dark matter.

The biggest mystery in modern physics is definitely Dark Matter where comprehensive searches are conducted in different experiments with various theoretical foundations. The NA64 experiment is committed to the search of Dark Photon; a new gauge boson which could mix with photons [6]. The theory behind this experiment is based on the existence of a very weak interaction between the ordinary and the dark matter which is transmitted by $U'(1)$ gauge boson A' (dark photons) mixing with photons. If such interaction exists, dark photons can be reproduced by the emission of A'-strahlung in the reaction $eZ \to eZA'$ of electrons scattering on nuclei due to $\gamma - A'$ mixing (photon-dark photon)[7], afterwards the A' would decay in visible mode (SM particleS) or invisible mode (Dark Matter particleS). The reaction is produced on an active target and the Dark photon is detected by missing energy events, if it decays on invisible mode. Such reaction is suppressed by a factor of 10^9 to 10^{12} compared to the normal bremsstrahlung $eZ \to eZ\gamma$ depending on the mixing strength $10^{-5} < \epsilon < 10^{-3}$ and masses $M_{A'} < 100$ MeV [8]. It means that for a minimum of 10^9 electrons on target, 1 bremsstrahlung process would reveal a dark photon.

Therefore a high intensity and high purity electron beam is needed for such reaction. It is difficult to achieve a contamination level below a fer percent, even with the latest improvement of beam lines. This represents a challenge for the experiment and it is tackled by using non-common techniques of particle identification.

In chapter 4 we describe how the synchrotron radiation can help the experiment to tag the incoming electrons and simultaneously to reject the presence of hadrons. The detection of the synchrotron radiation is performed by two scintillator crystal types and their performance of hadron suppression is compared. This suppression helps to obtain the first results for dark photon decay searches on invisible mode (dark matter particles).

2. Small-strip Thin Gap Chamber characterization

The aim of this chapter is to show the characteristics of new detectors to be used as part of the ATLAS experiment upgrade, and how to achieve the requirements of the high luminosity operation. The results of each test to characterize the detector are presented.

2.1. High Luminosity Large Hadron Collider

The Large Hadron Collider (LHC), located at the European Organization for Nuclear Research (CERN, derived from *Conseil Européen pour la Recherche Nucléaire*) at the Franco-Swiss border near Geneva is a circular accelerator of 27km circunference of acceleration pipes and constitutes the largest scientific instrument ever designed and built for scientific research. It has been successfully commissioned in March 2010 for proton-proton collision with a 7 GeV center-of-mass energy.

The LHC is pushing the limits of human knowledge, enabling physicists to go beyond the Standard Model (SM): the enigmatic Higgs boson, the mysterious Dark Matter and the world of super symmetry are just three of the long-awaited mysteries that the LHC is working to unveil.

The announcement given by CERN on 4 July 2012 about the discovery of a new boson at 125-126GeV[1, 2], almost certainly the long awaited Higgs particle, is the first fundamental discovery, hopefully the first of a series, that the LHC can deliver.
Such discovery was made possible thanks to the general-purpose detectors ATLAS and CMS, both located at 2 interaction regions, complemented by the specialized detectors ALICE and LHCb.

	Period	Energy $\sqrt{s}$	Luminosity $\mathcal{L}$	Integrate $\mathcal{L}$
Run I	2010-2012	7-8 TeV	$6 \times 10^{33}\,\mathrm{cm^{-2}s^{-1}}$	$25\,\mathrm{fb^{-1}}$
LS1	2013-2014	LHC: Go to design energy, nominal luminosity, bunch spacing 25ns		
Phase 0	2015-2018	14 TeV	$1 \times 10^{34}\,\mathrm{cm^{-2}s^{-1}}$	$75\,\mathrm{fb^{-1}}$ to $100\,\mathrm{fb^{-1}}$
LS2	2019-2020	ATLAS: Upgrade μ spectrometer; NSW, LAr Calorimeter & FTK		
Phase 1	2021-2023	14 TeV	$2 \times 10^{34}\,\mathrm{cm^{-2}s^{-1}}$	$\sim$350 $\mathrm{fb^{-1}}$
LS3	2024-2025	ATLAS: New Inner Tracker and trigger architecture		
Phase 2	2026-2030	14 TeV	$5 \times 10^{34}\,\mathrm{cm^{-2}s^{-1}}$	$\sim$3000 $\mathrm{fb^{-1}}$

Table 2.1: LHC Schedule & upgrades for ATLAS detector.

The LHC baseline program until 2030 is shown in Table 2.1. After entering into the nominal energy regime of 13 TeV to 14 TeV center-of-mass energy in 2015, it is expected that the LHC will reach the design luminosity of $1 \times 10^{34}\,\mathrm{cm}^{-2}\mathrm{s}^{-2}$. This peak value should give a total integrated luminosity of about $40\,\mathrm{fb}^{-1}$ per year. In the period 2019-2023 the LHC will hopefully further increase to two times the peak luminosity, reaching at the end of 2023 an integrated luminosity of about $350\,\mathrm{fb}^{-1}$.

After the Long Shutdown 3 (LS3) the machine will be re-launched in the High Luminosity configuration (HL-LHC). For its successful realization, a number of key novel technologies have to be developed, validated, and integrated, accompanied with upgrades from the general purpose detectors such as ATLAS.

2.2. ATLAS Detector

The ATLAS detector is a general-purpose experiment, designed to explore proton-proton collisions at center of mass up to $\sqrt{s}$ =14GeV in the Large Hadron Collider (LHC) at the European Laboratory for Particle Physics (CERN). It is aiming to understand the foundations of matter and forces, in particular the nature of mass in a broad physics program. The ATLAS detector was built with the ability to discover the Higgs boson over a wide mass range. It can also perform searches for the production of heavy particles that would indicate physics beyond the Standard Model, such as super symmetric particles, as well as searches for other massive objects.

The ATLAS experiment includes complex detector systems. The central part is a cylindrical Inner Detector, to detect charged particles produced in the collisions, and as such, it is a compact and highly sensitive component. It consists of three different systems of sensors, all immersed in a magnetic field parallel to the beam axis. The **Inner Detector** measures the direction, momentum, and charge of electrically-charged particles produced in each proton-proton collision. The next part is the Calorimeter (red and green on figure 2.1), which measures the energy of a particle when it loses its energy as it passes through the detector. It is usually designed to stop entirely or to "absorb" most of the particles coming from a collision, forcing them to deposit all of their energy within the detector. Calorimeters typically consist of layers of "passive" or "absorbing" high-dense material -for example, lead-interleaved with layers of an "active" medium such as scintillator or liquid argon.

Electromagnetic calorimeters measure the energy of electrons and photons as they interact with matter. Hadronic calorimeters sample the energy of hadrons (particles that contain quarks, such as protons and neutrons) as they interact with atomic nuclei. The components of the ATLAS calorimetry system are: the **Liquid Argon (LAr) Calorimeter** and the **Tile Hadronic Calorimeter**.

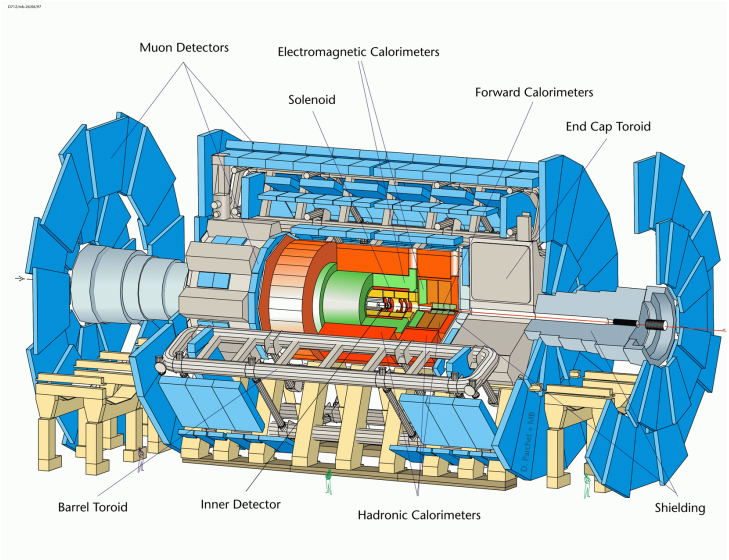

Figure 2.1: ATLAS detector, Muon Spectrometer (in blue)

Calorimeters can stop most known particles except muons and neutrinos. Muons are charged particles that pass through the Inner Detector and Calorimeter interacting only by ionization, they can penetrate through large amount of material without any strong interaction, they have long lifetime, therefore can be considered as stable particles within the detector's volume, and provide a good tagging for the lepton's decays channels.

To trigger and detect these particles, the ATLAS experiment uses the **Muon Spectrometer**, made up of 4.000 individual muon chambers (different types of gas chambers) which are in charge of identify each one of these muons. It is only possible to measure their momentum with the help of the **Magnet System**, made of three sections; the **Central Solenoid Magnet** with a 2T magnetic field that bends the charged particles for momentum measurement near the interaction points, helping the Inner Tracker system, the **Barrel Toroid** bends the muon particles in the low rapidity region, and the **Endcap Toroid** with a 4T magnetic field that bends the muons in the high rapidity region.

2.2.1. Coordinate system

A common coordinate system is used through ATLAS. The interaction point is defined as the origin of the coordinate system. The z-axis runs along the beam line. The x-y plane is perpendicular to the beam line and is referred to as the transverse momentum, p_T. The positive x-axis points from the interaction point to the center of the LHC ring; the positive y-axis points upward to the surface of the earth. The detector which is located half at positive z-values is referred to as the "A-side", to the other half the "C-side". The transverse plane is often described in terms of $r - \phi$ coordinates. The azimuthal angle ϕ is measured from the x-axis, around the beam. The radial dimension, r, measures the distance from the beam line. The polar angle θ is defined as the angle from the positive z-axis. The polar angle is often reported in terms of pseudorapidity, defined as $\eta = -\ln\tan(\theta/2)$. The distance ΔR is defined in $\eta - \phi$ space as $\Delta R = \sqrt{\Delta\eta^2 + \Delta\phi^2}$.

2.2.2. Detector Upgrade

To fulfill the LHC program (in table 2.1), and in order to benefit from the expected high luminosity performance that will be provided by the Phase-I upgraded LHC, the first station of ATLAS muon end-cap system (Small Wheel, SW) will need to be replaced. The **New Small Wheel (NSW)** will have to operate in a high background providing a radiation region (up to 15 kHz/cm^2 of photons, and 75 Hz/cm^2 of neutrons is expected) while reconstructing muon tracks with high precision as well as furnishing information for the Level-1 trigger. These performance criteria are demanding. In particular, the precision reconstruction of tracks for offline analysis requires a spatial resolution of about 100 µm, and the Level-1 trigger track segments have to be reconstructed online with an angular resolution of approximately 1mrad.

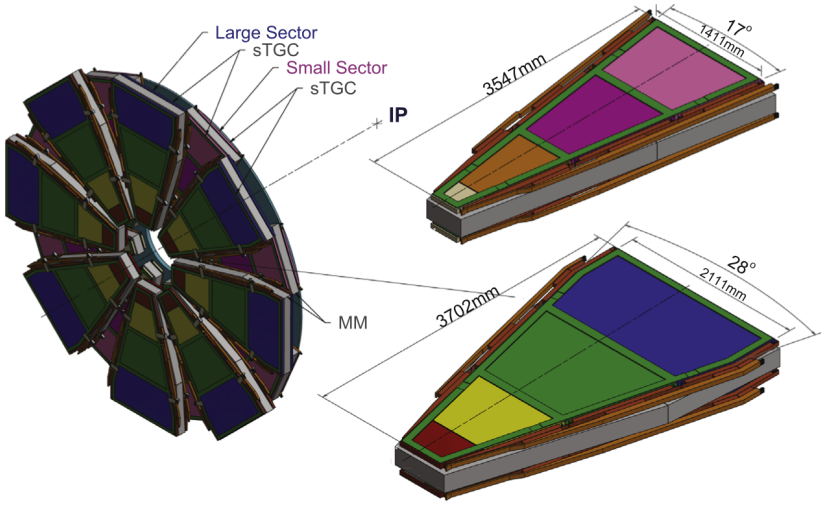

Figure 2.2: New Small Wheel

The NSW will have a two-chamber technology, one primarily devoted to the Level-1 trigger function (Small-strip Thin Gap Chambers, sTGC) and the other one dedicated to precision tracking (Micromegas detectors, MM). The sTGC is deployed for triggering given its single bunch crossing identification capability, a fast response and good position resolution.

The MM detectors have exceptional precision tracking capabilities due to their small gap (5mm) and strip pitch (approximately 0.5mm). Such a precision is crucial to maintain the current ATLAS muon momentum resolution in the high background environment of the upgraded LHC. The MM chambers can, at the same time, confirm the existence of track segments found by the muon end-cap middle station (Big Wheels) online. The sTGC has the additional ability to measure offline muon tracks with good precision, so the sTGC-MM chamber technology combination forms a fully redundant detector system for triggering and tracking both for online and offline functions. This detector combination has been designed to be able to provide excellent performance for the eventual High Luminosity LHC upgrade.

2.3. sTGC Description

The small-strip Thin Gap Chamber (sTGC) is a kind of multi-wire proportional chamber (MWPC) which works in a high gain mode (limited proportional region). The successful introduction of MWPC to detector systems in 1968 has earned Georges Charpak the Nobel prize in Physics 1992. These devices have been a major ingredient to detector systems since they can achieve spatial resolution of tenths microns, and have typical time resolution of about 50 ns.

The sTGC has been designed to exploit these features, working with a cathode-anode pitch smaller than the anode-anode pitch, mostly based on the design of the Thin Gap Chamber[9], with thinner strips as the main improvement from the previous version. The TGC technology has been used since 1988 in the OPAL experiment[10] and is currently part of the muon spectrometer in ATLAS.

This new chamber has the advantage of having a 3.2mm strip-pitch compared with the 6mm from the previous TGC, which explains the *small-strip* prefix.

Chambers with different strips sizes were built and tested under pion beams, and the 3.2mm pitch was chosen as the best option to provide a resolution better than 100 µm[5]. This change will improve the measurement of charge centroid position by charge interpolation.

To improve the time response, the cathode surface resistivity has been reduced by a factor 10, to reduce charge accumulations on the cathode when chamber operates at high rate, lowering from 1MΩ/□ to 100-200kΩ/□ resistivity on the graphite layer. At the same time, cathode-readout plane (strips or pads) distance was reduced to 100 µm(400 µm before) to increase the capacitive coupling by 4, therefore $\tau = RC$ is reduced by 60%, leading to a fast response from cathode readout.

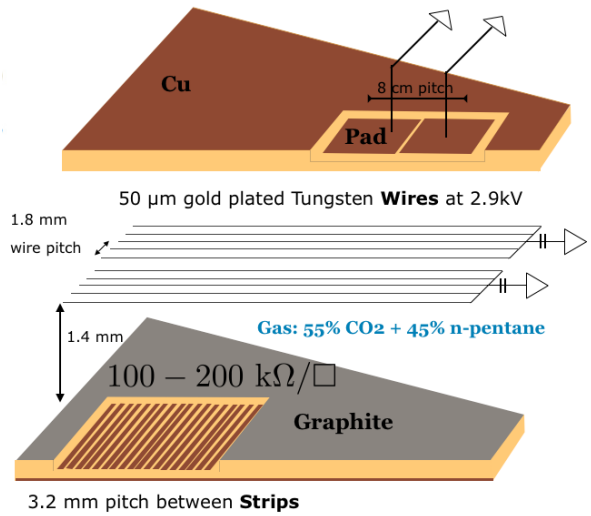

Figure 2.3: Single plane sTGC

The sTGC is made of two resistive cathodes planes, with copper readout plane with strips on one layer and the other one with pads, with 8x12cm^2 area used for fast pat-

tern recognition of tracks to select strips for read out. This represents a big advantage compared to the TGC, which does not have this feature.

The cathodes are made of FR4 with 1.4 mm of thickness, where 17 µm of copper is etched for strips (pads), pressed with a 100 µm of FR4 over it and then sprayed with graphite to provide superficial resistivity.

The anodes are golden tungsten wires of 50 µm diameter, distributed at 1.8 mm of distance between each other and a gas gap of 2.8 mm. To work with such geometry, several tests were made to find the proper gas mixture[11]. The most suitable mixture has been found to be 55% (CO_2) and a quenching gas, a primary ingredient is 45% of n-pentane(n-C_5H_{12}), which allows the chamber to work in a limited proportional region[12]. The latest ingredient; n-pentane, can absorb UV photons due to its many molecular degree of freedom, hence preventing the chamber from going into a Geiger mode.

2.3.1. Electric field simulation

Motivated by gaining better understanding of the detector operational mechanisms, dedicated simulations studies using gaseous detector simulation tools have been performed. The main simulation tool used is Garfield a software package[13, 14]. This set of libraries allows to calculate the electrical field with geometrical configuration as drift chambers.

The simulation uses a coordinate system where x is along the strips, y defines the chamber depth and z is along the wires.

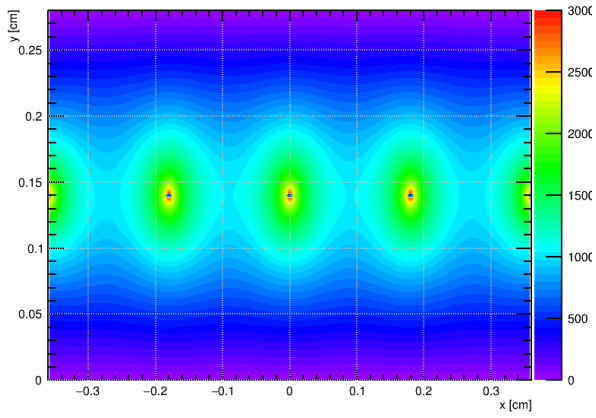

Figure 2.4: Equipontential lines, anode at 2900V

Both contour plots on figure 2.5 represent the magnitude of the electrical field with scale of 1×10^3 V/cm to 1×10^5 V/cm with 50 steps. At the working potential 2.9 kV, it is possible to observe a field strength of more than 1×10^4 V/cm over a 97% of the gas gap. The weakest field is only in a small region in the middle of two neighboring wires, leading to less than 5% of long drifting electrons.

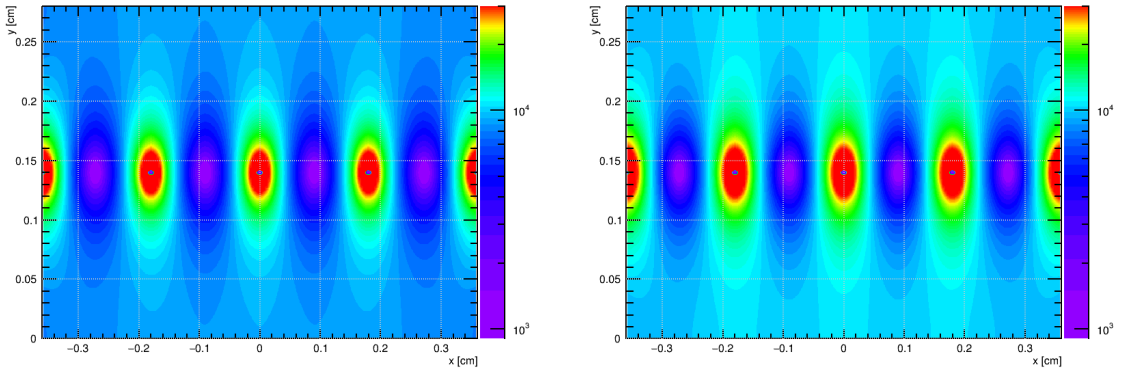

(a) Electrical field, anodes at 2500V **(b)** Electrical field, anodes at 2900V

Figure 2.5: The electric field map in the x-y plane for a typical operating high voltage 2900 V and 2500 V.

2.4. Construction process

The main novelty on this detector is the high resolution obtained on x-axis due to the strip boards and the alignment between each chamber to get precision of about 50 µm and 30 µm respectively.

It is important to discuss the process which makes it possible to achieve these numbers. Everything relies on how well these chambers are built and also how the cathodes boards (strips and pads) are fabricated.

The size of each chamber varies from 0.7 m^2 to 2.5 m^2 with around 1m long, where over 300-400 strips must be etched with a precision of 50 µm. A standard length for printed circuit boards (PCB) is 70 cm. Extreme precaution must be taken to provide the precision and parallelism between each strip, in one of the biggest PCB board ever made.

The attempt of this section is to provide an overview of how the sTGC Quadruplets are built, mostly on the first module 0 produced by UTFSM, which is the QS1 (Quadruplet Small sector, part 1). Being the smallest detector to be produced for the NSW has some pros and cons. The main cons are related to the position of the QS1 inside the NSW; it is the closest one to the interaction point and as such, it gets the highest rate of particles. For the same reason, the position resolution is a key point and the high efficiency response under a high rate environment is a must.

Some pros are related to its size; with approximately 1.3 m long, 35 cm the small base and 75 cm the large one of the trapezoidal shape, the sTGC QS1 can be handled without any problems during its construction.

Quality Control of cathode boards

The cathodes for the module 0 were made by an Italian company MDT, and since it was the first production, the review was done on-site.

The thickness of the board is measured in 19 points around the perimeter with a micrometer. The values of theses measurements must be within 1.5 mm±25 µm. Exceeding

this numbers leads to the partial rejection of the cathode boards, however if there is a single point deviation of less than 35 µm from the average, it could be used in combination with another cathode board that does not have the same local deviation.

An electrical test is done with a multimeter, to check if there is any short circuit between strips or pads depending on the cathode board.

The last step and the most important is the dimensional control; it is performed on a granite table, with 2 pins that match the brass inserts on the cathode and a special caliper.

An aluminum-ruler (Al-ruler) machined (see Figure 2.6a) with a precision of 30 µm at 20 Celsius degrees is used as caliper. Above the cathode board the misalignment is measured. It has the same strip pitch for the first and the last five strips as well as two intermediate regions, and to avoid any parallax, the thickness of the edge for these strips is 1 mm. Looking with a magnifying glass around 4 regions allows to detect some misalignment between theses strips (caliper and cathode board). A photography is taken and analyzed to calculate this misalignment. For such distance (about 1 m long) some precautions must be taken, considering the expansion coefficient for both material.

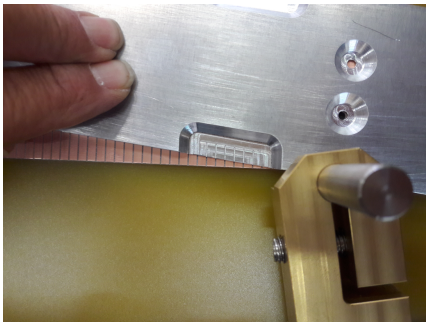

(a) Al-ruler used to check shift over the last strips.

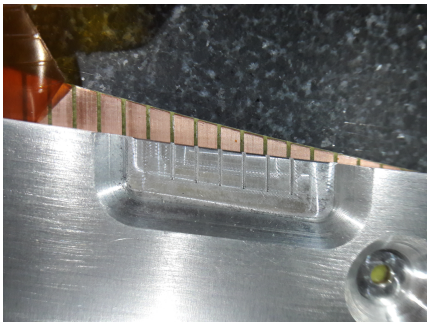

(b) Zoom-in Comparing strip position

Figure 2.6: Strip control with **Al** ruler

Cathode preparation

Once the cathodes pass all the dimensional control, they have to be cleaned with Acetone and Isopropyl alcohol and placed on a granite table (with a flatness better than 30 µm) with a vacuum system underneath. They have to be fixed on the edges with metal jigs which have marks for the internal wire support or chamber division.

The places which are not sprayed with graphite, like the wire support and the edges, are covered with a 3.5 mm black tape on the designated wire support locations across the board. To prevent spraying graphite on the places where they will be glued, a blue tape must be placed on the edges.

Graphite spraying

A key point for this process is to prepare the "painting", a mixture of Graphite-33 with Plastik-70 bonding agent.

The graphite must be agitated for at least 2 hours before mixing with Plastik-70. A proper ratio of 1500 g Graphite and 540 g Plastik is mixed during 2 hours before spraying.

A spraying machine is in charge of this process, and meanwhile temperature and humidity must be controlled. After the cathode is painted, the superficial resistivity is measured on the edges. Values must exceed 100kΩ/□ otherwise the cathode needs to be sprayed again.

Polishing

In order to ensure an homogeneous resistivity across the chamber, the cathode is visually divided in to 5x6 sections. Inside each section, the resistivity is measured on 5 to 7 points with a probe. Simultaneously the cathode is brushed in the same orientation as the wires. The brush must be done carefully, without over-polishing areas, because once the resistance drops down, nothing will bring it back up.

Gluing internal parts

After removing all the blue and black tapes, all the internal parts (buttons, wire support, etc.) are glued to provide mechanical support to the anode wires.

The wire support and the buttons help the chamber not to bend due to gravity and not to create a catenary effect. The external frames provide the 1.4mm height for the gas gap. All these parts are cleaned with isopropyl alcohol, While the glue, a type of epoxy (2011-Araldite) is prepared, all these parts are cleaned with isopropyl alcohol. This glue will not only fix the parts, it will also fill the surfaces where these parts are less thick than requested.

Winding wires

A flat table which can spin around one axis is used to wind the cathodes board. On each side of the table, one cathode with all the internal parts is tight with metal clamps on the edges. At the same time, vacuum is applied underneath to ensure the flatness of the cathode. A winding machine places each wire at 1.8 mm distance from each other with 50 µm precision.
After the process is completed, all the wires are soldered in batches of 10 over the wire-rulers. The remaining wire can be cut and the HV resistors (10 MΩ) soldered. The metal clamps around the edges are then removed, and the relative wire tension is checked by comparing the deflection of adjacent wires.

Detector Assembly

Once the cathodes are winded and all wires are soldered, the Pad cathode board is cleaned with clean water and dried with clean air. The board is placed on the granite table

(with vacuum underneath) to be tested with high voltage. It is necessary to monitor the current from the cathode while the voltage is increased. It starts with 100 V and reaches 3000 V, with steps of 100 V. The current should never reach a value higher than 1 µA. If it does, the cathode needs to be checked carefully, to remove dust or glue which create sparkles.

Reaching the nominal current, the strip cathode board is placed against the pad cathode board carefully. An aluminum frame with a silicon rubber is placed on top to isolate the chamber from the environment. Afterwards, vacuum is applied to this chamber and CO_2 is flushed inside the chamber.

The power supply is turned on and no sparkles (monitoring the current) must be found.

In order to prevent dust from entering the chamber, the glue is prepared to close it immediately. Upon completion of the process, a single chamber is built.

A doublet is assembled with two single chambers glued with a honeycomb paper. Repeating the process with two doublets, the quadruplet is built.

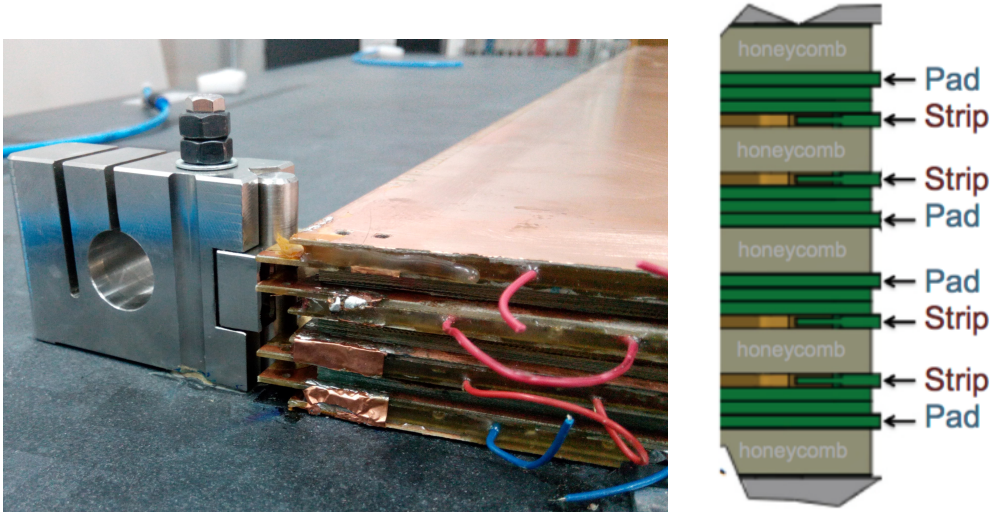

(a) Module #0 against alignment pin **(b)** Layer description

Figure 2.7

2.5. Gain uniformity measurements

After the chambers are built, it is important to look for any malfunctioning. A primitive test to check the behavior of the detector is to move a radiation source across the sensitive area, while the current draw is measured from the power supply.

In this test, it is important to understand what can produce variation on the gain. There are two main factors that can produce gain variations on wire detectors. The first one is the "nature gain fluctuations" from the charge production in proportional counters which follows Polya distribution, however it is less pronounced in limited proportional mode such as sTGC working region.

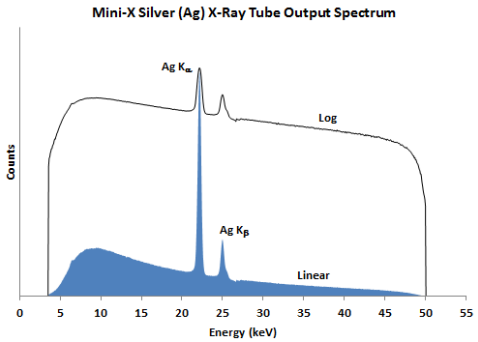

(a) Output spectrum, from 0 to 50keV

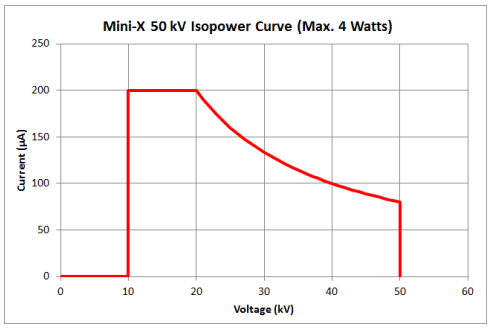

(b) Isopower curve for the Mini-x gun

Figure 2.8

The second one is related to the mechanical tolerances. This part has been very well known for 40 years as it is presented in Sauli's book [15] about drift chambers from which we can conclude the following:

- Variations on the wire diameter of about 1% (fabrication precision) results in a 3% change in the gain.
- A 100 µm difference in the gas gap thickness (2.7 mm) results in about 15% change in the gain.
- The effect of a wire displacement of about 100 µm of a wire plane results in 1% in the charge of the two adjacent wires which with a gain of $\sim 10^6$ will give a $\sim$ 10% change on the gain.

Taking all of this in consideration, it is expected to get a gain variation of less than 20% in agreement with the Construction manual[16].

The amount of current measured from the power supply is considered as gain reference, while the detector is irradiated with x-rays. The test is performed under two different working points (bias voltage), 2500V (low gain) and 2900V, the operational voltage.

For such test the x-ray source is used due to the following advantages:

- Mostly mono-energetic photons.
- Variable photon intensity: Limiting the current from the tube from 1 µA to 200 µA can provide different rates.
- Variable photon energy: Varying the breaking voltage of electrons inside the x-ray gun from 10 kV to 50 kV.
- Different spot size: with a set of collimator it is possible to irradiate area of interest (group of wires).

2.5.1. Setup

To perform such test, a x-ray gun called Mini-X[17] from Amptek is used, with silver (Ag) as transmission target and with a beryllium (Be) end-window.

(a) Mini-X gun mounted on KUKA robo-arm

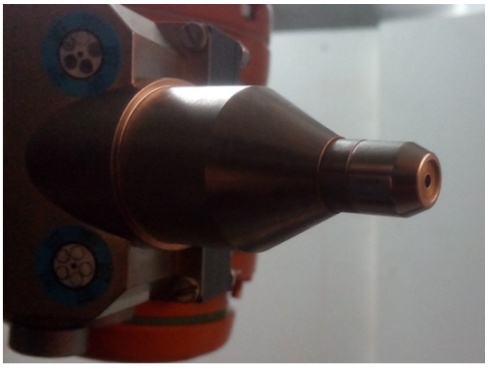

(b) Collimator 2mm

Figure 2.9

The gun is mounted on a KUKA robo-arm (see Fig.2.9a), with a 5 degrees collimator providing a 4 mm^2 spot size at a proper distance. The robo-arm provides the x-y movement to scan the whole sensitive detector area, moving from the small base to the large base along the wires at steps of 1.2 cm/s (y-axis).

The robo-arm moves along the x-axis in 5 cm/s steps. This is not the most suitable step to irradiate the whole detector, but it allows the x-ray gun to work properly at 45 µA, 50keV energy (see figure 2.8b) without overheating.

A NIM HV Power Supply Module CAEN 1470 was used to power the chambers. The power supply (PS) was controlled by USB with the CAEN HV Wrapper Library. The current registered from the PS was written in a ASCII file for further analysis. The sampling rate used from the PS was 1 per second, giving the current average during this period. The test is taken in approximately one hour, irradiating one chamber at the time.

Since the detector is already built as a quadruplet, it has to turn over to irradiate its other face. Hence, only the external layers (chambers) are irradiated directly without having an chamber to provide a screening effect.

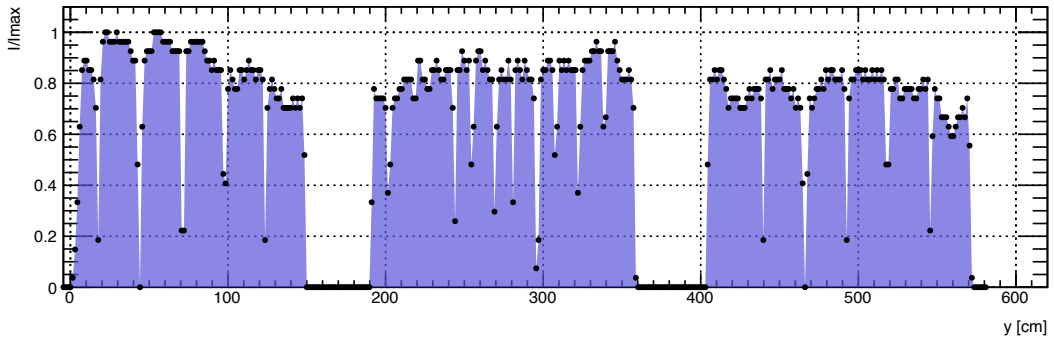

Figure 2.10: Relative current to the maximum, while the robo-arm is moved along the wires. The three set current corresponds to the whole detector irradiated in three different positions from x-axis.

	Chamber 1	Chamber 2	Chamber 3	Chamber4
σ/mean%	15.08%	17.18%	17.25%	16.64%

Table 2.2: Uniformity gain

2.5.2. Results

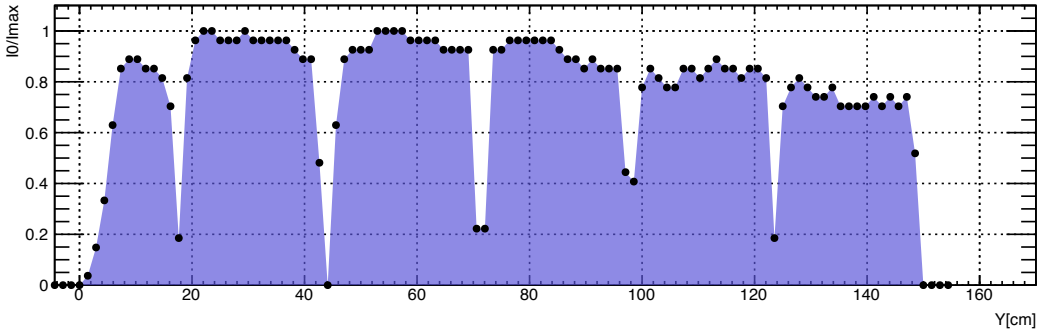

Figure 2.11: Moving across strips, wire-supports are present with minimum gain.

At first glance, it is possible to observ the internal structure of the chamber with this test. Looking at the Figure 2.11 the current decreases when the gun is irradiating the places where the wire-supports are found. In theses places a small gas volume is present, therefore less electrons can drift to the wires, resulting in less current draw from the power supply.

If a better meshing of the irradiation places could be performed, identification of the wire-supports and the chamber separation (small and large sector) could be obtained with good resolution. For internal parts of 20mm, a width from 17 mm to 23 mm has been obtained with this test.

Interpolating the points (x, y, I), an overall picture can be obtained (Figure 2.12a). The figure shows a line with high current resulting from a missing wire in the chamber. More charge is collected by the neighbors when a wire is missing, resulting from a longer drift path.

The graph on Figure 2.12b shows the average current from each Chamber at two different working potentials. The average is calculated only for the sensitive area, hence, only values where the wire-support are not present form part of the average. The average current values at 2.5kV and 2.9kV are 200 nA and 1.2 µA respectively.

The Table 2.4 summarizes the uniformity obtained, calculated as the RMS over the mean from the current draw distribution for each chamber. The four chambers have less than 20% of gain variation, which was expected from the construction manual.

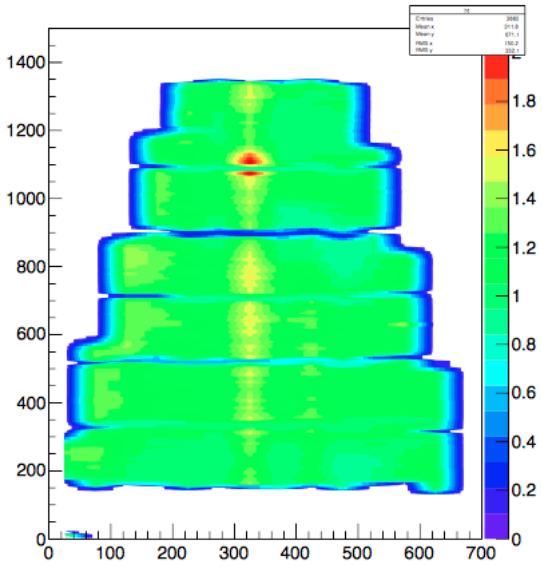

(a) xy-scan Chamber3 sTGC Module #0: missing wire

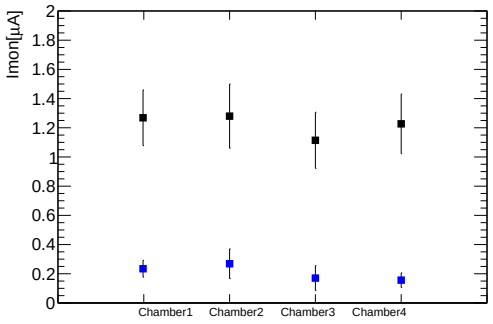

(b) Current draw at 2.5kV (blue) and 2.9kV(black)

Figure 2.12

2.6. Stability under high rate

One of the key feature of this detector is that it must be able to work under high particles flow rates (15kHz/cm^2), and the first step is to check whether the device or its electronic components can handle this high rate.

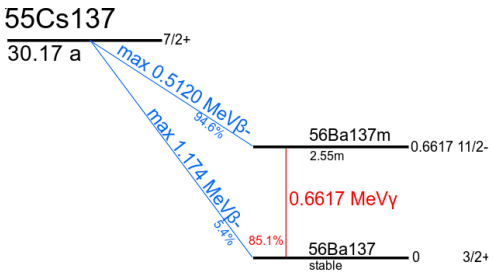

Figure 2.13: Cesium-137 Decay scheme.

For this purpose, the Module#0 was placed inside a new High Radiation Facility at CERN called GIF++[18]. The installation has a Cesium-137 (Figure 2.13) as a gamma source with an activity of approximately 14.9TBq (13.3TBq during the test, August 2016). A system of movable lead attenuators (Figure 3.3b) for large irradiation zone allows attenuation factors between 1 and 5×10^5 in several steps.

In order to get a reference of the particle rate, a direct measurement setup was implemented with a small size (16.2 cm × 12.4 cm as sensitive area) sTGC as a **Monitor**. A LVDS (Low voltage differential signaling) logical signal from wires was obtained from an Amplifier Shaper Discriminator (ASD) board[19] connected to this Monitor.

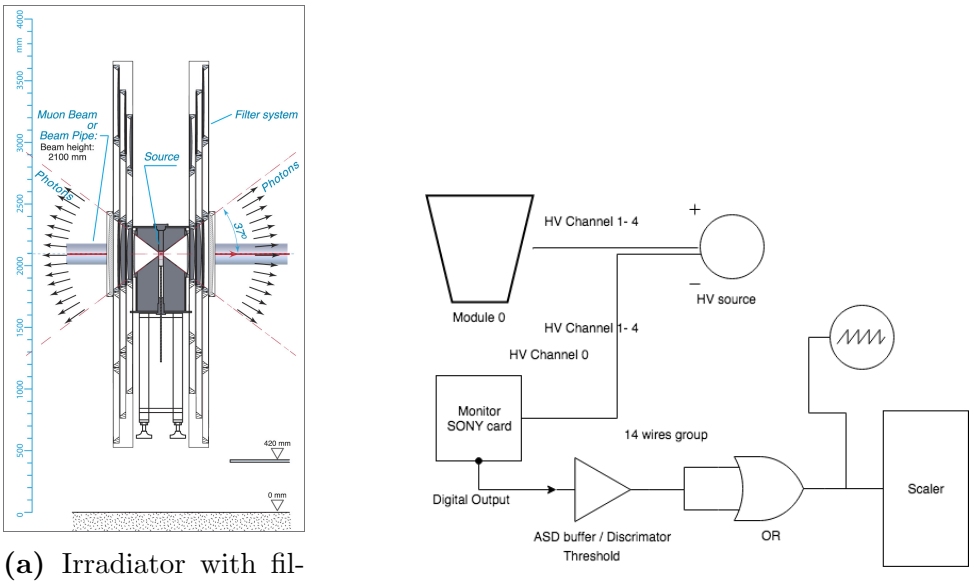

(a) Irradiator with filter system.

(b) GIF++ setup.

Figure 2.14: Three different rows with three lead (Pb) layers, each one with different thickness to provide multiples rates for the facility.

The ASD board provided the signal from 16 wires groups, all of them connected to a VME module (KEK ASD buffer), which controls the threshold from the discriminator on the ASD and converts the LVDS to NIM signal. The 16 LVDS signals are converted into two NIM logical signals. The two outputs from the module are connected to a Scaler NIM n145 which provides the number of positive NIM signals from the 16 channels in 10 seconds.

The Module#0 and the Monitor were placed at 1.3 m distance from the radioactive source. Both were connected in series to the same gas line ($55CO_2$: 45 n-pentane), and the temperature and pressure were recorded to keep track of the working voltage. Most of the time, the environmental conditions were measured at 25 Celsius degree and 971 mbar.

The working potential for the chamber is 2850 V at 1 bar. Since the gain is proportional to E/P, where E is the electrical field and P the pressure inside the chamber, the voltages must be decreased by 2.9% to compensate the lower pressure, resulting in a 2765 V as the new working point in this environment.

To achieve the background rate for ATLAS (15 kHz/cm^2), the Monitor must register more than 2680 kHz if the sensitive area is considered. The sensitive area is calculated as the total area 200 cm^2 times the amount of wires group connected to the ASD.

Four different attenuation factors were registered (10, 4.5, 2.2 and 1). On Figure 2.15a it is possible to observe two sets of data with rates over than the expected one (red and blue). The other two sets of data emphasize the *plateau* reached over 2.7 kV. At the same time, the highest rate shows an inefficiency on voltages over 2.8 kV and the *plateau* is lost. Therefore, the data set with attenuation 2.2 (in red) is our reference.

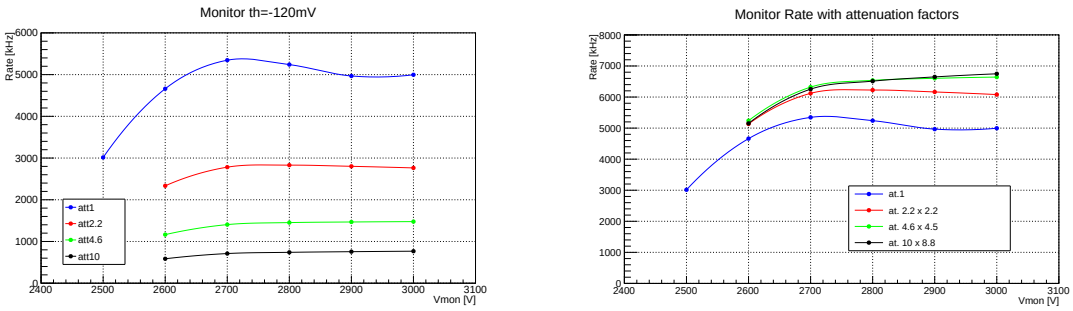

(a) Different attenuation filters **(b)** Multiplying by att. Factors

Figure 2.15: Rate on **Monitor**

Multiplying the attenuation factors with each data set (Figure 2.15b) should give us the expected rate with no filters. However, the data set with factor 1 has 5 MHz at working potential (2.9 kV), while the expected rate from data sets attenuation 10 and attenuation 4.6 is 6.6 MHz. When comparing the rates from data set 1 with these, we observe an efficiency of about 75% of the expected rate. Then, comparing the data set 2.2 with the lowest rates results in approximately 93% of efficiency.

These findings may suggest a change in the gamma spectrum emitted after the attenuation filters. For a comprehensive analysis, a detailed study of the spectrum can be found in Chapter 3.

The flow rate recorded in data set 2.2 is 28 kHz/cm^2. If we compensate the inefficiency, the total flow rate is 30 kHz/cm^2, which is the double than expected as a background level for ATLAS. Therefore the sTGC detectors must be tested against attenuation factor lower than 4.4.

Once the Monitor is set, the quadruplet is connected to the high voltage power supply. Each layer is internally divided in two sections, a small sector (S0) and large sector (S1). Each sector is powered independently on each channel by a CAEN High Voltage power supply A1833P (4 kV/2 mA max). The current from each layer (two sectors each one) was recorded with a resolution of 0.1 µA. Four different attenuation filters were applied, and the results are shown in Figure 2.16.

$$\Delta\% = \left| 1 - \frac{I_1/I_0}{A_1/A_0} \right| * 100 \tag{2.1}$$

These results show a linear dependency of voltage, with lower resistance as the rate of particles is increased. It is also important to notice that each wire group is connected to a 10 MΩ resistor, however not all the wires have the same length (the chamber has a trapezoidal shape), resulting in a lower voltage drop from the external groups where the wires are shorter (collecting less charge).

The Table 2.3 compares the area ratio between the internal sections of each chamber with the current registered for each set of measurements. The effect of dropping voltage appears to be the explanation of the incremental disagreement of the area ratio as the rate increases.

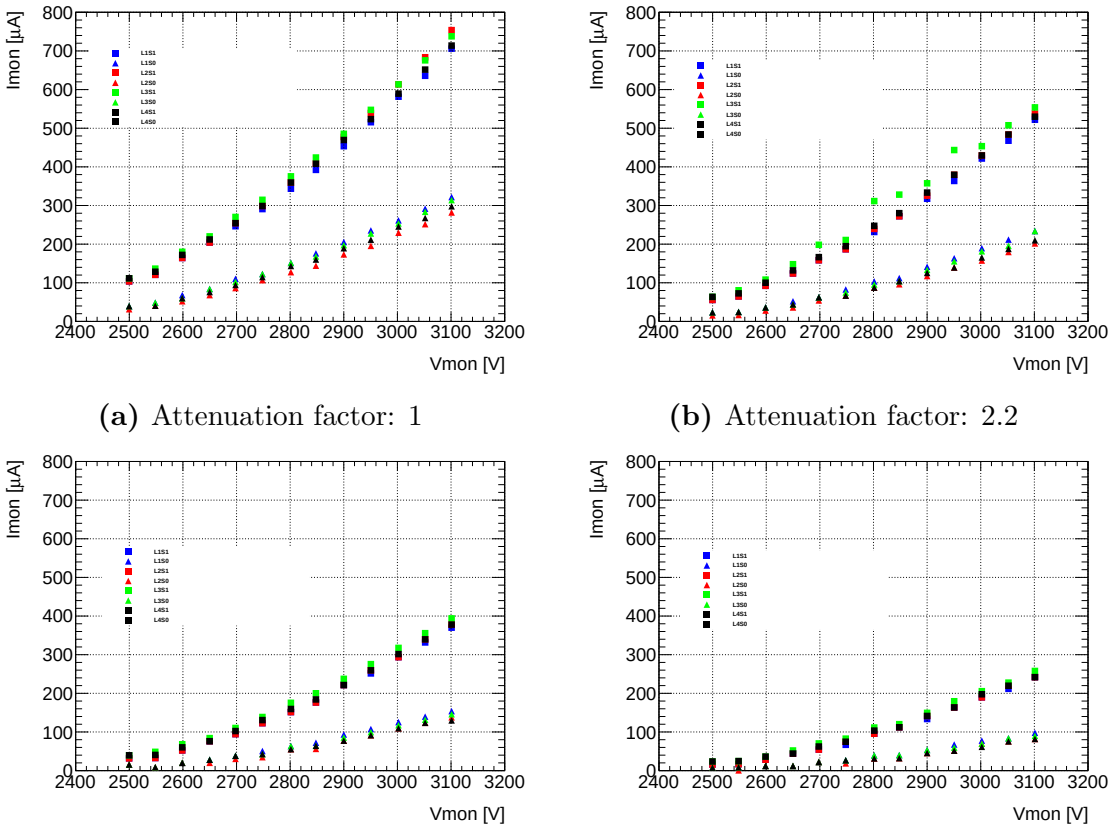

(a) Attenuation factor: 1

(b) Attenuation factor: 2.2

(c) Attenuation factor: 4.6

(d) Attenuation factor: 10

Figure 2.16: Current registered on the power supply for each chamber, large (S1) and small sector (S0) against applied voltage on anode.

The set of graphs shown in Figure 2.17 highlights the disagreement between different working voltages for two different rates.

These two sets of data are the expected rates for the large and small sector on the sTGC QS1. Hence, it is important to compare these ratios with the amount of current registered by both sectors. As the area ratio increases, the current ratio decreases, which suggests the use of different HV resistors for the external wires groups to produce an homogeneous voltage drop.

	Layer 1		Layer 2		Layer 3		Layer 4	
A_1/A_0	2.53		2.78		3.07		3.40	
Filter	I_1/I_0	$\Delta\%$	I_1/I_0	$\Delta\%$	I_1/I_0	$\Delta\%$	I_1/I_0	$\Delta\%$
10	2.49	1.58	3.02	8.63	3.01	1.95	3.08	9.41
4.6	2.34	7.51	2.87	3.24	2.73	11.07	2.87	15.59
2.2	2.29	9.49	2.79	0.35	2.68	12.70	2.67	21.47
1	2.22	12.25	3.02	8.63	2.45	20.19	2.49	26.76

Table 2.3: Comparison between sensitive area ratio (A_1/A_0) from large and small sectors with the ratio of current (I_1/I_0) at 2.9kV. A percentage difference column ($\Delta\%$ defined in equation 2.1) is calculated to highlight the incremental disagreement as the gamma rate and the area ratio increases.

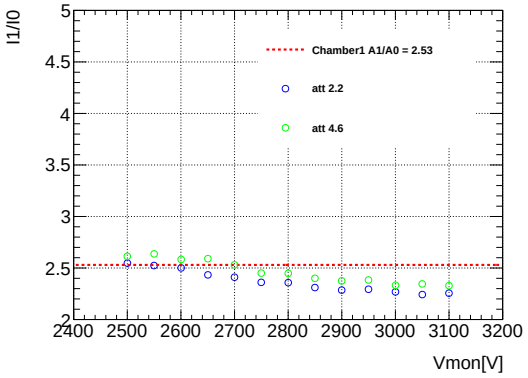

(a) Chamber 1, A_1/A_0 =2.53

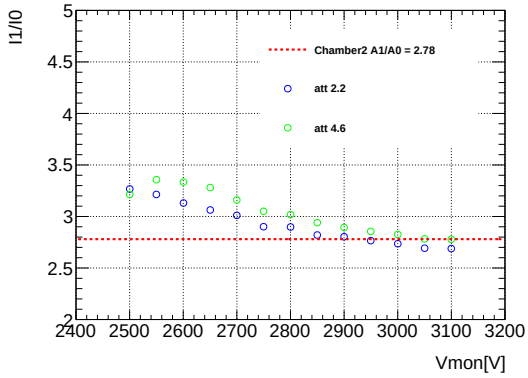

(b) Chamber 2, A_1/A_0 =2.78

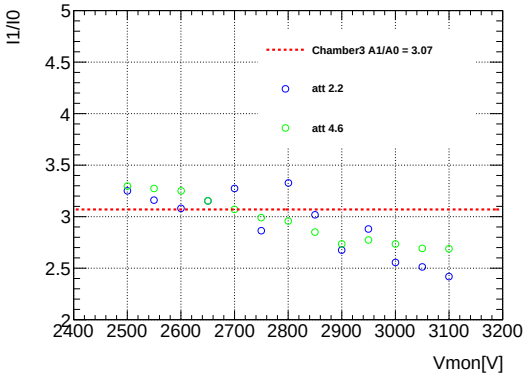

(c) Chamber 3, A_1/A_0 =3.07

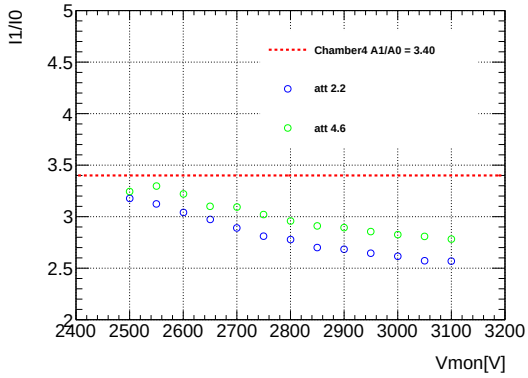

(d) Chamber 4, A_1/A_0 =3.40

Figure 2.17: Current ratio I_1/I_0 for two different rates compared with the area ratio A_1/A_0 at different anode voltage. The Chamber 3 in (c) has a missing wire in the large section (A_1), therefore the area ratio must be slightly lower and an increase of the current can be expected for the same reason.

2.7. Spatial Resolution

In order to achieve the precision reconstruction of tracks (offline) with a spatial resolution of about 100 µm per sTGC layer, and fast trigger on the region of interest (ROI) with Pads, two test beams were done.

In the spring of 2014, the Weizmann Institute of Science in Israel built the first full-size sTGC quadruplet detector of dimensions 1.2 m × 1.0 m. This prototype consists of four sTGC strips and pad layers and was constructed using the full specification of one of the quadruplets to be used in the NSW upgrade (the middle quadruplet of the small sector). The first test beam experiment took place at Fermilab with one goal in mind, to determine the position resolution of a full-size sTGC.

EUDET pixel telescope was used as a reference to measure the beam position, using the technology of 6 Minimum Ionizing MOS Active Pixel Sensor (Mimosa26) detectors with ≈ 5 µm position resolution. Three telescopes are placed in front of the beam, and three after the sTGC as is shown in Figure 2.18 with 15 cm between them and 64 cm between each arm. Each Mimosa26 detector has an active area of 2.24 m^2 made of CMOS pixel matrix of 576 rows and 1152 columns with 18.4 µm pitch.

A 32 GeV pion beam was used at the rate of 1 kHz over a spot of 1 m^2 giving to the sTGC a very precise pion trajectory thanks to the EUDET telescope. Event triggering was controlled by a custom Trigger Logic Unit (TLU). The TLU received signals from two 1 cm × 2 cm scintillators placed in front and behind the telescope. The TLU generated the trigger signal that was distributed to the telescope and the sTGC readout electronics, which consists of a first application-specific integrated circuit (ASIC) called VMM1 which has the ability to read out both positive (strips, pads) and negative (wires) polarity signals, on 64 individual readout channels.

The VMM1 analog circuit features a charge amplifier stage followed by a shaper circuit and outputs the analog peak value (P) of the signal.

The readout of the ASIC is zero suppressed and thus only peak values of channels with signals above a predefined threshold are read. At the same time, the VMM1 may be programmed to provide the input signal amplitude of channels adjacent to a channel above threshold (neighbor-enable logic).

The precise position of a charged particle traversing an sTGC gas volume can be estimated from a Gaussian fit to the measured charge on adjacent readout strips (referred to as strip-clusters from here on). Given the strip pitch of 3.2 mm and sTGC geometry, charges are typically induced on up to five adjacent strips.

The spatial sampling of the total ionization signal over a small number of readout channels means that a precise knowledge of each individual readout channel baseline is necessary in order to achieve the best possible measured spatial resolution.

The baseline of each individual readout channel was measured by making use of the neighbor-enabled logic of the VMM1 and its internal calibration system.

Test pulses were sent on one readout channel with the neighbor-enabled logic on, and baseline values were obtained by reading out the analog peak values of the two channels adjacent to the one receiving a test pulse.

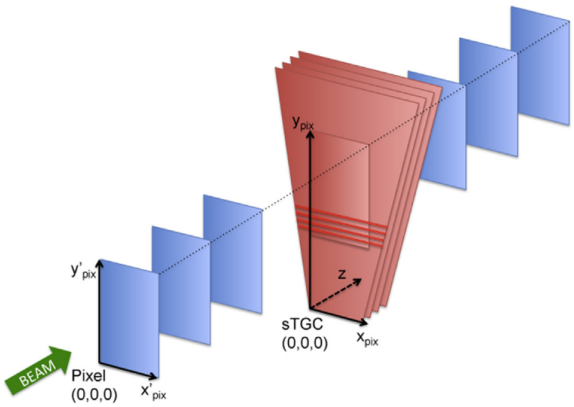

Figure 2.18: Schematic diagram of the experimental setup at Fermilab and coordinate systems used. Three layers of silicon pixel sensors are positioned before and after the sTGC detector.The dimensions are not to scale.

The silicon pixel hit positions were then used for reconstructing three straight dimensional charged-particle tracks. A track quality parameter was obtained for each fitted pion track based on the χ^2 of the track-fit. A small value of the track quality parameter corresponds to a straight track and a cut on this parameter can therefore be used to mitigate multiple scattering which are not considered in this analysis.

2.7.1. Analysis Model

Pixel telescope analysis

In this model the intrinsic position resolution is obtained comparing the extrapolated beam trajectory from the pixel detectors with the measurements in each of the sTGC quad planes. Each layer is analyzed separately to reduce the effect of the multiple scattering and only tracks with $\chi^2 < 10$ are considered for the same reason. From Figure 2.18 one can see that the *y-axis* is defined perpendicular to the strips, therefore sTGC strip-clusters provide measurements of the particle position in the y-direction(y_{sTGC}).

The position resolution is directly related to the profile of induced charge on the strips. The particle position is estimated from a Gaussian fit to the induced charge distribution on the strips. The neighbor-enabled logic of the VMM1 was used. Strip-clusters with induced charge in either 3, 4 or 5 adjacent strips are selected.

The pixel telescope tracks provide both coordinates, x_{pix} and y_{pix} at the position of the sTGC layer studied. The spatial resolution measurement is obtained by fitting the residual distribution y_{sTGC} and y_{pix} with a Gaussian model.

The charge measured on the strips of the sTGC detector results from a spatial sampling and discretization of the induced charge. The process of reconstructing the sTGC strip-cluster position from this sampling introduces a non-linearity differential effect on the reconstructed strip-cluster position.

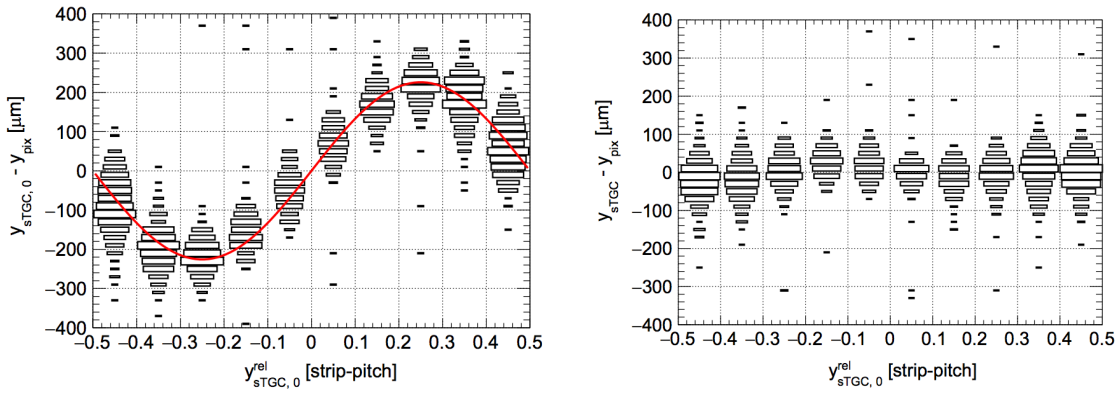

(a) The non-linearity differential for sTGC strip-clusters

(b) The differential after sinusoidal correction is applied

Figure 2.19: Charge distribution over strip-pitch

Table 2.4: Fit parameters per cluster size

Strip-cluster multiplicity i	Amplitude parameter a_i
3	205 ± 9
4	206 ± 4
5	211 ± 5

The deviation of the measured strip-cluster position from the expected position (estimated by the pixel telescope track) depends on the strip-cluster position relative to the strips. This dependence is clearly seen in the two dimensional distributions in Figure 2.19a. It shows the y-residual versus strip-cluster position relative to the closest inter-strip gap center $y^{\text{rel}}_{\text{sTGC},0}$. This effect is corrected using a sinusoidal function:

$$y_{\text{sTGC}} = y_{\text{sTGC},0} - a_i \sin\left(2\pi y^{\text{rel}}_{\text{sTGC},0}\right) \tag{2.2}$$

where $y_{\text{sTGC},0}$ is the strip-cluster mean resulting from the Gaussian fit and y_{sTGC} is the corrected particle position estimator. The amplitude parameters are denoted a_i for the 3,4 and 5 strip-multiplicity (cluster size). These amplitude parameters are free parameters in the fit. The values of the amplitude parameters obtained from the fit to data are compatible with being equal for the three strip-cluster multiplicity as shown in Table 2.4.

The correction function is therefore universal and is shown in Figure 2.19a. The two dimensional distribution after the correction is applied was found to be reasonably flat as shown in Figure 2.19b.

The alignment of the coordinate system of the pixel telescope with respect to the above-defined coordinate system of the sTGC layer also affects the measured residual distribution. A simple two-parameter model is used to account for translations and rotations of the two coordinate systems with respect to each other. Both the alignment correction and the differential non-linearity correction are included *in situ* in the analysis.

The alignment correction is introduced in the model by expressing the pixel track position in the sTGC-layer coordinate system y_{pix}, as a function of the track position in

the pixel telescope coordinate system x'_{pix} and y'_{pix}, and two misalignment parameters δy and ϕ_{xy}, as follows:

$$y_{\text{pix}} = -x'_{\text{pix}} \sin\phi_{xy} + y'_{\text{pix}} \cos\phi_{xy} + \delta y \tag{2.3}$$

The variable δy corresponds to a misalignment along the y-axis of the sTGC coordinate system, and ϕ_{xy} corresponds to a rotation of the telescope coordinate system in the x-y plane around the z-axis of the sTGC coordinate system. Translation and rotation misalignment along and around the other axis are not taken into account in this model, since they are expected to have a small impact on the determination of the intrinsic position resolution.

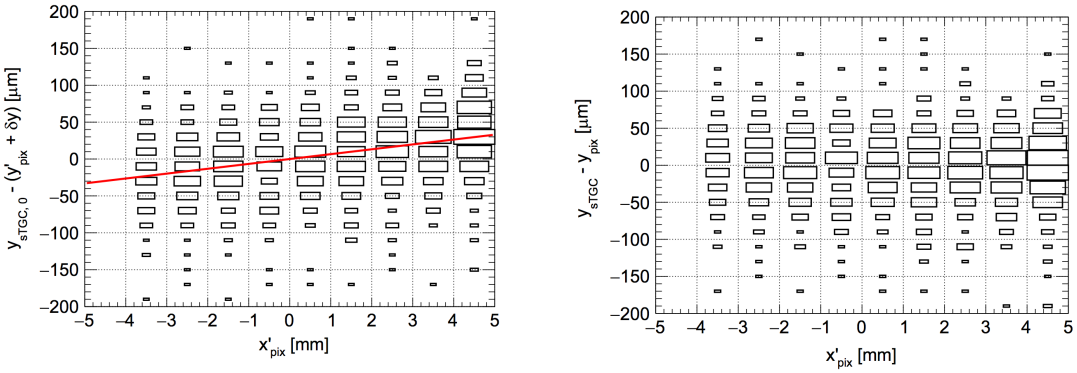

(a) Residual y against x position on pixel telescope.

(b) After rotation and translation applied

Figure 2.20: Coordinate system correction

On the Figure 2.20a it is possible to observe the y-residual mean increase linearly as a function of the x position on the telescope called x'_{pix}, which is evidence for a small rotation between the two coordinate systems. The red line represents the correction applied to this dataset. Accounting for this correction results in a distribution that is independent of x'_{pix} on Figure 2.20b.

After all the corrections are applied, the calculations for the intrinsic resolutions are taken for each layer and compared with the residual distribution. A double Gaussian function (equation 2.5) is fitted, where the first Gaussian represents the core of the residual distribution and the second one is a wider Gaussian which represents some reconstructed strip-cluster from background sources.

$$\begin{aligned} F_i &= F_i(y_{\text{sTGC},0}, y^{\text{rel}}_{\text{sTGC},0}, x'_{\text{pix}}, y'_{\text{pix}}; \delta y, \phi_{xy}, a_i, \sigma, f, \sigma_w) && (2.4)\\ &= fG(y_{\text{sTGC}} - y_{\text{pix}}; 0, \sigma) + (1-f)G(y_{\text{sTGC}} - y_{\text{pix}}; 0, \sigma_w) && (2.5) \end{aligned}$$

On Figure 2.21 a set of events shows the distribution presented before with an intrinsic resolution parameter σ of about 44 µm for a representative data taking run and sTGC strip-layer, where the red line is the narrow Gaussian fit and the dashed line is the wider Gaussian fit.

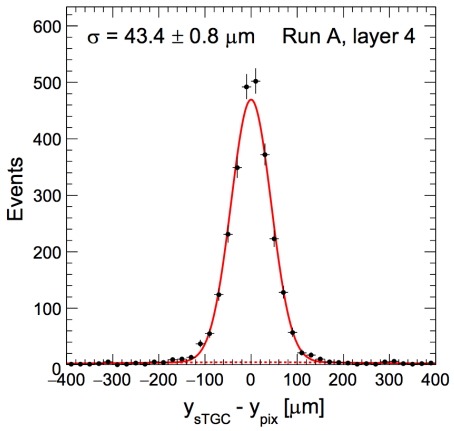

Figure 2.21: Intrinsic resolution of layer 4, respect to pixel telescope. The solid line correspond to the narrow gaussian and the dashed line to the wide gaussian fit.

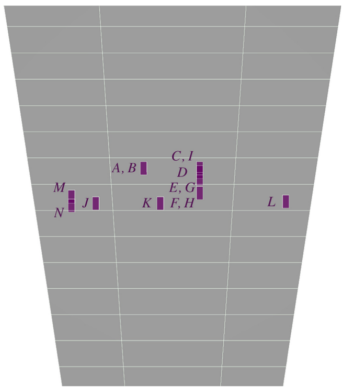

(a) Beam position for different data sets on sTGC

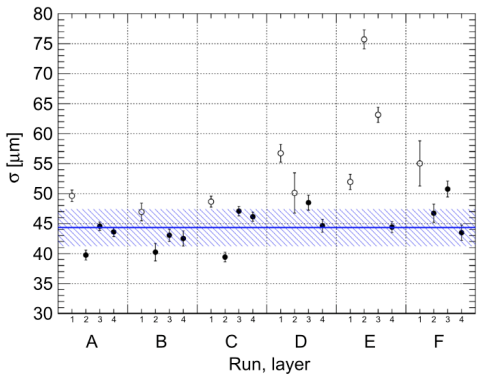

(b) Summary of intrinsic resolution for each data set and layers of sTGC

Figure 2.22: Summary of pixel telescope analysis

The fraction of the data parameterized by the narrow Gaussian is around 95% with a RMS of about 2%. The rest of data taking runs and its beam position can be observed on Figure 2.22b, where the black circles represent the valid data and the open circles the runs with expected degradation due to detector structure supports or individual channel pedestal.

sTGC standalone analysis

In this analysis the correction for the differential non-linearity in respect to strip-pitch obtained before is kept, however the residual distribution of the y-position is calculated from two pairwise layers of the sTGC. Therefore half of the variance of this distribution corresponds to our parameter to estimate the intrinsic resolution for one layer, hence $\sigma = \sigma_{\text{residual}}/\sqrt{2}$.

A strip-layer position residual distribution for a representative sTGC standalone data

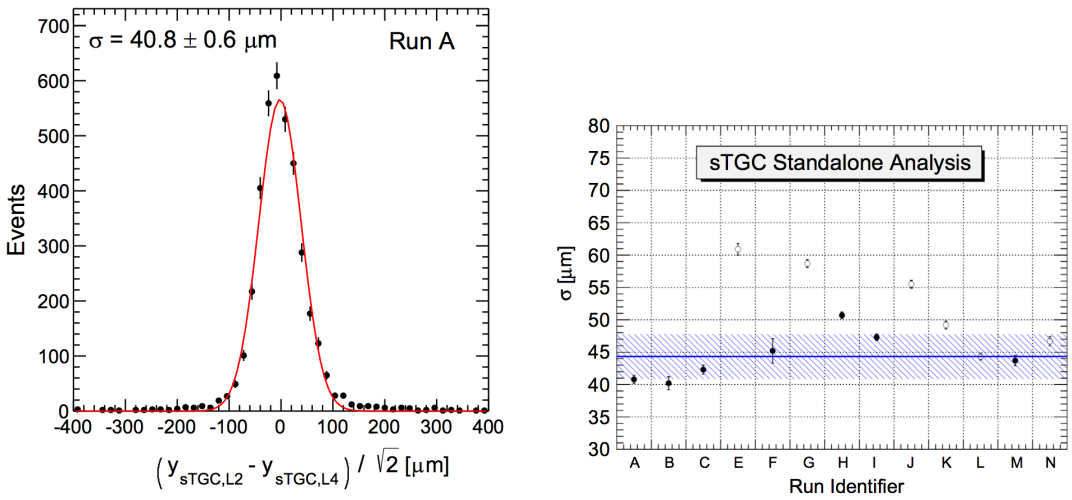

(a) (b)

Figure 2.23: (a) Resolution estimate based on adjacent sTGC strip-layer position residual distributions for a representative sTGC standalone data taking run.
(b) Summary of the measured intrinsic sTGC resolution using the pixel telescope analysis for different data taking runs. The beam position on the sTGC detector for each run is shown in 2.22a. Results for runs with no expected degradation due to sTGC detector support structure or calibration are shown as black filled circles. The horizontal line represents the average resolution for these runs whereas the hashed band represents the RMS spread. Results for the remaining runs are shown as open circles.

taking run is shown in Figure 2.23a.
In this graph, a intrinsic resolution of $\sigma = 40.8 \pm 0.8 \mu m$ is obtained.

In summary of fourteen data sets, the intrinsic resolution with this analysis is about 45 µm. The white open circles on the graph 2.23b correspond to non-validate data due to wire-support position or mis-calibrations. The hash band represents the RMS spread and the blue line is the average.

2.8. Pad efficiency

One of the new features of the small-strip Thin Gap Chamber compare to its previous version is the possibility to provide a fast trigger for the Region of Interest from the $8\,\mathrm{cm}^2 \times 50\,\mathrm{cm}^2$ pad area, where 3 out of 4 pads from a sTGC quadruplet can confirm a particle candidate, therefore a track position can be obtained from the strips within this area.

A test beam experiment was conducted at the CERN H6 beam line, using a 130 GeV muon beam of about 4 cm radius, a wider beam spot to test the characteristics of the pads. The setup is shown in Figure 2.24 where the system was triggered by a set of

scintillators (in blue) with a $12\,\mathrm{cm}^2 \times 12\,\mathrm{cm}^2$ coincidence area.

As explained before, for the beam tests a preliminary front-end electronics based on the VMM1 was used. This ASIC provides a Time-over-Threshold (ToT) signal as digital output, however it is also possible to get analog pulses. During the test beam, using the present configuration, an inefficiency was observed related to small late charges from the sTGC detector which may be not well adapted to the VMM1. An efficiency of 80-90% was observed running at $100\,\mathrm{kHz\,cm}^{-2}$.

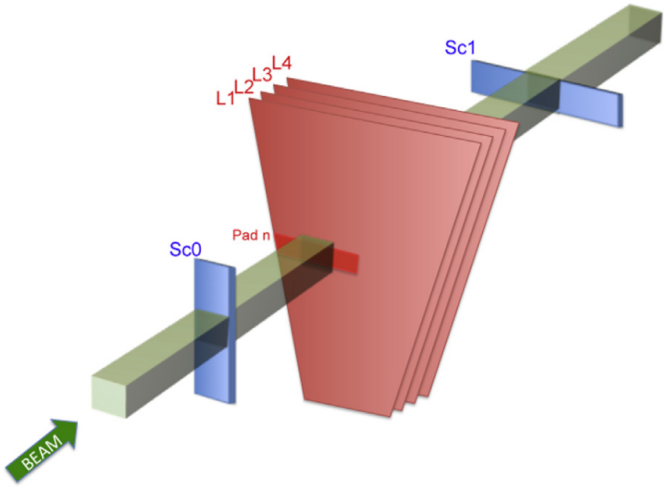

Figure 2.24: Setup for pad measurements. Coincidence block in light green. Pad n in red. Scintillators in blue.

To ensure that no inefficiency was due to the detector itself, the large cathode pads were used to estimate the detector efficiency, which was measured by looking at the analog output of the front-end amplifier. The efficiency of the pad n in the first layer was defined with respect to the coincidence of the trigger with a signal in the fully overlapping pad of the second layer.

Two examples from this configuration are shown on Figure 2.25; on the left two analog signals from pads are present with a ToT signal from layer 1 with about 2 µs length, meanwhile on the right picture a long ToT pulse with more than 40 µs length when the two analog signal (in coincidence) are present. By recording hundreds of triggered events using an oscilloscope, the presence of a detector signal within the live-part of the front-end electronics (independent of the signal threshold) was checked. This test confirmed that the detector was 100% efficient.

Charge sharing between pads

To study the transition region between pads, the scintillator coincidence triggering area and the particle beam were centered between pad n and pad $n+1$ of the first layer, as illustrated in Figure 2.26a.

After applying timing quality requirements on the strip and pad hits, the channel baseline values are subtracted from the analog peak values. Strip-clusters with induced

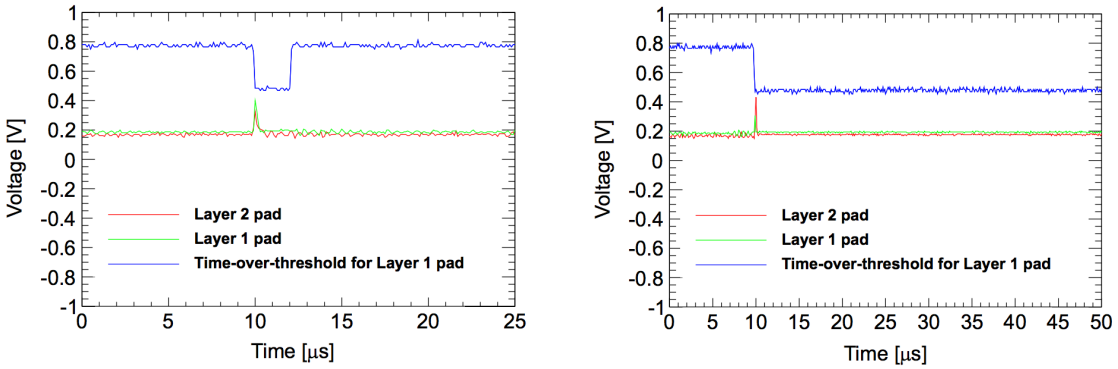

(a) ToT signal from pad L1, pad L2 as a trigger

(b) Large dead time on ToT signal from pad L1

Figure 2.25: Digital and analog signal from VMM1

charge in either 3,4 or 5 adjacent strips are selected and calibrated in the same way as for the Fermilab beam test.

Events with a single strip-cluster in the first layer and the second layer are selected. The strip-cluster position (mean of the fitted Gaussian) in the first layer is used to define the position of the particle going through the detector. The events are further required to contain a hit above threshold on either pad n or pad $n+1$. The charge fraction (F) is defined using the analog peak values (P) of the two adjacent pads:

$$F = \frac{P_n - P_{n+1}}{P_n + P_{n+1}} \tag{2.6}$$

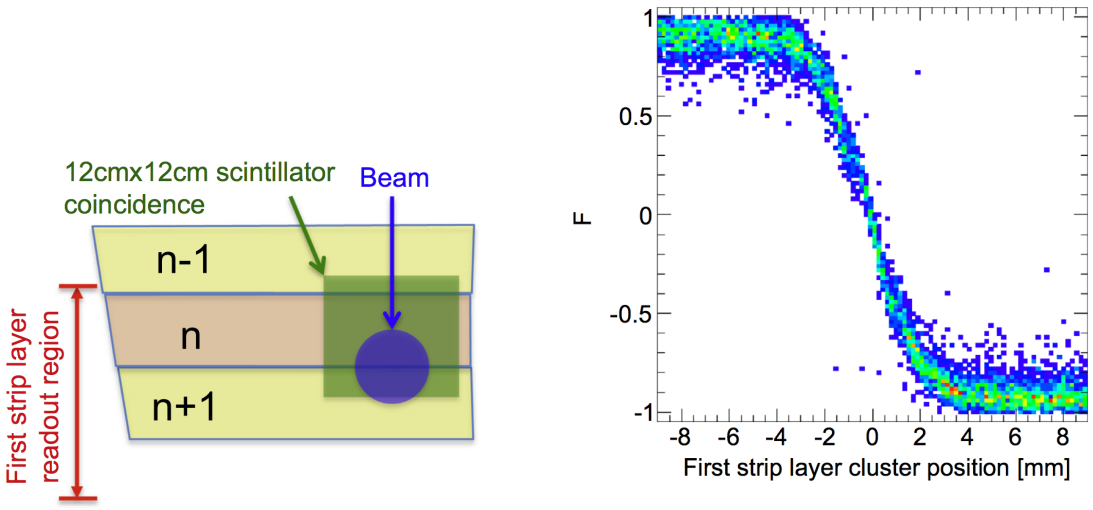

(a) Pad region transition scheme

(b) Charge Sharing distribution

Figure 2.26

Figure 2.26b shows the charge fraction as a function of the position with respect to the

center of the transition region, where the two pads share more than 70% of the induced charge, spans about 4 mm.

2.9. Summary

In the chapter we introduce the construction process and discuss the phenomenology of the sTGC. The main features of this Thin Gap Chamber are presented. The smaller strips of 3.2 mm pitch give the spatial resolution needed for the improvement of the New Small Wheel of ATLAS. The main problem to achieve this precise 3.2 mm±50 µm pitch in long boards (1 m to 2 m long) is discussed.

To improve the time response and fulfill the timing of bunching crossing, the resistivity of the graphite layer is decreased and the distance between the readout and graphite layer is reduced to a 100 µm, hence the $\tau = RC$ is decreased by a factor 0.4.

The sTGC detector is tested with four different objectives. The first test under x-rays occurs right after the Quadruplet is constructed. The use of this source helps to understand the construction issues as well as the qualifying process, where the uniformity of the gain is measured. Certainly, multiple factors can be improved in this test, such as increasing the vertical and horizontal steps to benefit from the 2 mm spot size of the x-ray gun. Although the entire process for this test can be improved, the Module 0 shows an overall 17% gain uniformity for the four chambers.

In the Section 2.6 a direct measurement of the rate in a high irradiation environment is provided by a small size sTGC. The references values obtained help to set a working point to test the new Quadruplets against high irradiation rate. The non-linear change in the resistivity of the chamber for different particles rates suggests a better election for the resistor component connected to the anode wires. All the group wires are connected in series to a 10 MΩ, however, not all the groups covers the same area, hence the amount of current (charge) is different for an homogeneous particle rate.

The last two sections summarize the two test beams for the first sTGC prototype, where crucial results are obtained for the electronics in charge of the readout. The test beam in CERN helps to understand the inefficiency of the Pads. The electronics designed for this detector (VMM1) has some issues which provides a 80-90% efficiency running at 100 kHz cm^{-2}. The detector is discarded, therefore, the VMM1 needs to be improved.

On the sTGC technology, all the efforts go to the improvement of the position resolution and the Section 2.7 shows a intrinsic resolution of about 40 µm for the standalone analysis.

The spatial resolutions and pad efficiency results have been published in "Performance of a full-size small-strip thin gap chamber prototype for the ATLAS new small wheel muon upgrade" [20].

The estimation of the position and efficiency resolution as a function of background rates inside the high rate environmental with a muon beam is remaining and it will be done after a new version of the VMM1 electronics is produced.

3. High count rate γ-ray spectroscopy in GIF++

In the previous chapter we discuss the behavior of the small-strip Thin Gap chamber under high gamma rates. The tests were performed at the new Gamma Irradiation Facility (GIF++) at CERN. This facility is designed to simulate background events of ATLAS or CMS detectors for the High Luminosity era of the Large Hadron Collider (HL-LHC).

The GIF++ provides a Cesium-137 irradiation source with a high intensity of 13.3 TBq. The intensity can be attenuated by a set of lead filters, resulting in 27 different intensities. Even with the highest attenuation filters the count rate can reach hundreds of MBq and therefore the spectra is difficult to measure. Our goal was to estimate the attenuation factors and the spectra at the same position as the sTGC detector (1.3 m) inside GIF++.

If there were only one γ-energy present, the problem would be reduced to the evaluation of the geometric counting efficiency and the absorption probability of the detector. However, the intensity determination becomes difficult in all cases where the emitted spectra are rather complex and where considerable background intensities are present. Since the energy region, where Compton interactions dominates, all γ-lines are connected with a continuous Compton distribution, the overlap of these Compton spectra makes detailed intensity determinations impossible.

As a first attempt, we measured spectra with few filters configurations at intensities up to 1/6 of the maximal count rate given by the crystal scintillator decay constant $1/\tau_{sc}$. With such intensities, effects of pile-up are observables and hence, the pulse reconstruction gets more difficult, leading sometimes to reject events. In our analysis we consider only the case where no pile-up is present or at least the second pulse is rejected.

To determine the amount of pile-up events and their peak position we use a Discrete Wavelet Transform (DWT), which decomposes the waveform in two components, smoother waveform (amplitude component) and a pulse sensitive to the high frequency (detailed component). The detailed component is sensitive to the rise time of the waveform, hence the starting position of an event. Having solved the problem of peak determination, we identify the single pulse and reject pile-up events.

In this chapter we present a set of spectra comparison between different attenuation filters to estimate the real attenuation value for > 600 keV events and how the spectra changes.

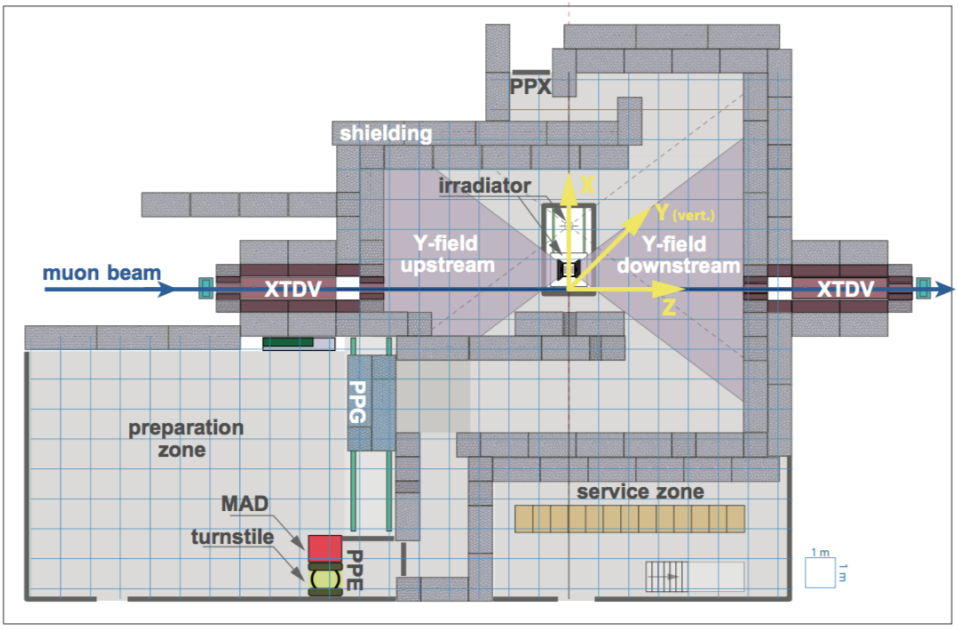

Figure 3.1: GIF++ layout.

3.1. Gamma Irradiation Facility, GIF++

During the next years, the High Luminosity LHC (HL-LHC) will enter in operation with 10 times more collisions than the current configuration, which will lead to a higher background and therefore, higher irradiation on each detector.

For the LHC era, several gas-based detectors were under study on the Gamma Irradiation Facility (GIF) and during the Long Shutdown 1 (LS1), a new facility has been built to cope with irradiation background from the HL-LHC named Gamma Irradiation Facility++ (GIF++)[21]. The facility is located on the North Area at CERN and is equipped with a ^{137}Cs gamma source with an activity of 13 TBq (on March 2015). With such intensity, all the gas-based detectors from ATLAS or CMS upgrades will be tested. Since all the detectors must remain working with good performance over 10 years, studies of aging process over the detector material or gas are performed. With few weeks under high intensity radiation one can simulate the detector aging over the expected working years.

The gamma source has been selected to emulate the background radiation by neutrons, produced on every collision. The energy spectrum of this background matches approximately the energy spectrum of the ^{137}Cs source, composed of the primary 662 keV photons and lower energetic scattered photons. The facility also provides a muon beam coming from secondary beam line (H4) from SPS. This beam line produces pions and kaons which can decay into muons. The muons produced by these decays represent 57-100% of the nominal energy range.

The GIF++ facility consists of a room surrounded by concrete walls (providing shielding) with the irradiator (radiation source) at the center of the two zones. Each zone is divided in three sections respect to the distance from the source, named {D1,D2,D3} and

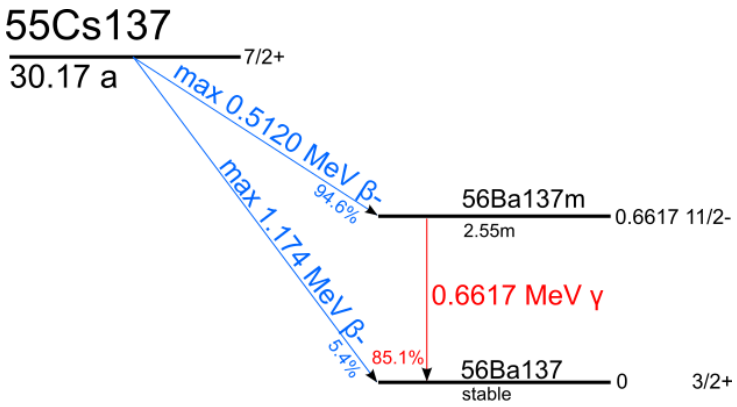

Figure 3.2: Cesium decay.

{U1,U2,U3} where D and U stand for Downstream and Upstream respect to the beam direction. The beam line is located right next to the irradiator. On Figure 3.1 it is possible to observe the two irradiation zones, together with the preparation and service area. The service area/zone is where all the electronic is placed, power supplies, acquisition systems, gas service, etc.

3.1.1. Irradiator and filter system

The gamma source used as irradiator is a Cesium isotope Cs-137 which disintegrates by beta minus emission to the ground state of Ba-137 (5.6%) or via isomeric level of Ba-137 (94.4%) which decays into ground state by a 661.7 keV gamma emission with a half-life of 2.55 min. Therefore, the excited state of Barium is responsible for all the gamma emission from the Cesium. The ^{137}Cs isotope was chosen instead of ^{60}Co due to its long half-life of 30.08 years, leading to a smaller decrease of the photon rate over the expected life-time of this facility. The irradiator has an activity of 13 TBq (in March 2015) resulting as the highest activity for a facility test. These two features will provide the high rate environment needed to study all the new gas-based detectors for the next few years.

The facility does not just provide the intensity for aging studies, but also fraction of the intensity. This feature could help to simulate the background conditions for $p + p$ collisions at high luminosity for different positions inside ATLAS/CMS. The irradiator (in Figure **??**) has its source inside a receptacle with two collimators, one for each zone with an open windows of 37° from center. The source is at 1.65 m from the base and when needed it can be hidden inside the lead shielding shown in Figure 3.3a.

On the Figure 3.3b it is possible to observe one shaped angular lens at the edge of the irradiator. The lens provides a uniform photon distribution over a plane with a proper correction on the attenuation. A uniform irradiation is needed for flat large area detectors. Afterwards, embedded inside a common enclosure, two complete and independent attenuation systems are available, each consisting of an array of 3x3 convex lead attenuation filters, to fine tune the photon flux for each irradiation field individually. The filters are in different thickness and with the same angular correction to provide a

	A	B	C
1	1	1	1
2	10	1.5	2.2
3	100	100	4.6

Table 3.1: Attenuation filters, nominal values

uniform field. The nominal attenuation factors are resumed on the next table:

The attenuation factors were chosen to provide a 24 different values to be nearly equidistant on a logarithmic scale.

The thickness of the angular correction filter varies for each angle of incidence in such a way that the desired attenuation is reached for all 662 keV photons. The attenuation can either mean that the photon has lost energy, or that it has been fully absorbed. For photons with lower energies, created due to scattering in the source capsule and the collimator irradiator, the angular correction filter leads to a less uniform current.

For the attenuation filters, on the other hand, the attenuation factor does not depend on the angle of incidence of the photons. The convex face of the attenuation filters is shaped in such way that at every point of the filter, photons from the source traverse the same thickness of material and hence undergo the same attenuation. The nominal attenuation factor is again defined as attenuation of 662 keV photons; photons with lower energy are attenuated to a larger degree. Due to the presence of lower energy photons, the effective total attenuation over the whole spectral range is lower than the nominal attenuation. The exact value will depend on the spectral sensitivity of the detector used.

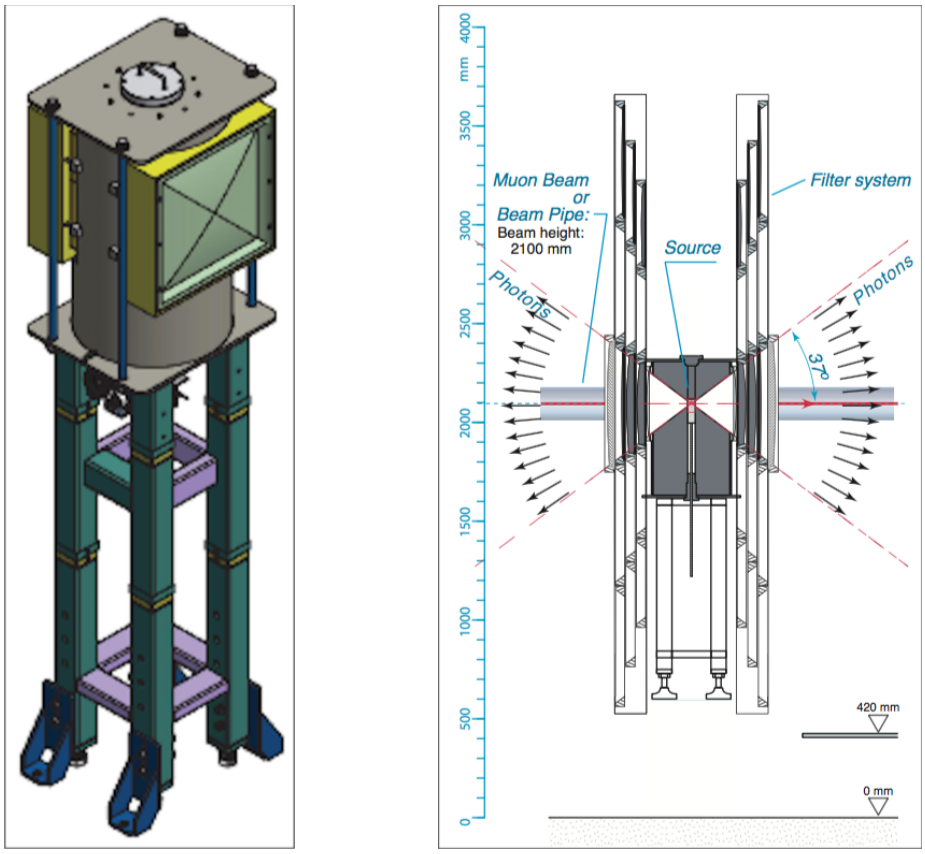

(a) Irradiator scheme **(b)** Irradiator filter system

Figure 3.3: Irradiator scheme and filter system

3.2. Setup and Apparatus

In order to measure the spectra of the irradiator a setup with a fast scintillator was prepared. The apparatus consists of a scintillator crystal $LaBr_3(Ce)$ coupled to a photo-multiplier (HAMAMATSU R7525). The crystal $LaBr_3(Ce)$ named BriLanCe^{TM}380 has the fastest decay among the organic scintillator with a decay time of 16 ns, resulting in a counting rate of 62 MHz. It also features a high light output (63 photons/keVγ) compared to the common $NaI(Tl)$.

The crystal has a cylindrical shape of 1″ diameter by 1″ (25.4 mm) long. This size matches perfectly to the PMT R7525 with an open window of 25 mm diameter of the effective area. This PMT has also a fast time response of about 1 ns, leaving the limitation of the counting rate to the scintillator. The PMT R7525 is a linear-focused type with 8 stages and a maximum Voltage between Anode and Cathode of 1750 V.

The two components, crystal and PMT, are installed inside a black aluminum tube. On one edge the signal output and voltage input connectors are installed, while on the detection side, a 4 mm thickness collimator is attached with a 25 mm hole. The window entrance is covered with black tape to prevent the light coming in. Black tubes and the rest of the apparatus are shown in Figure 3.4.

Figure 3.4: Detector housing, photomultiplier and BrilLance crystal.

3.2.1. Calibration

To calibrate our spectrometer we use the internal radiation from BrilLance crystal as radiation source. The active component on $LaBr_3(Ce)$ is the radioisotope Lanthanum-138 with a scheme decay shown in Figure 3.5. In 66.4% of its decays, ^{138}La undergoes electron capture (EC) to produce excited ^{138}Ba, which in turn decays by emission of a 1436 keV gamma. The remaining decays (33.6%), proceed by beta emission to ^{138}Ce, which decays by emitting a 789 keV gamma in coincidence with the beta having an end point energy of 255 keV.

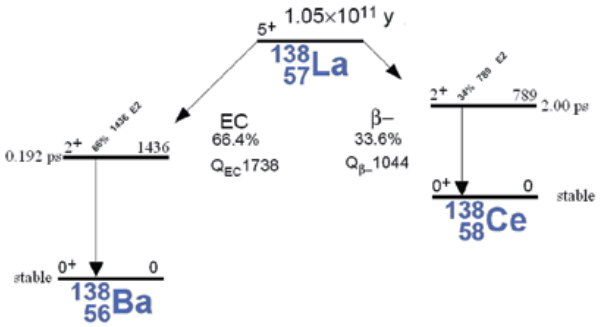

Figure 3.5: Lanthanum decay scheme from 8th edition Table of Isotopes.

The Figure 3.6 shows the spectra from the ^{138}La decay. It is possible to observe the two decays of the isotope, the main peak at 1436 keV corresponds to gamma emission from the excited Barium nucleus and x-ray emitted in coincidence when one electron fills the K level (37 keV), the second corresponds to the gamma emission from the Cerium nucleus. This gamma emission is in coincidence with the beta decay and the beta continuum

Voltage	$\Delta E/E\%$
1.3 kV	7.41
1.4 kV	5.45
1.5 kV	4.67

Table 3.2: Energy resolution

distribution overlaps the Compton decay from the gamma-ray.

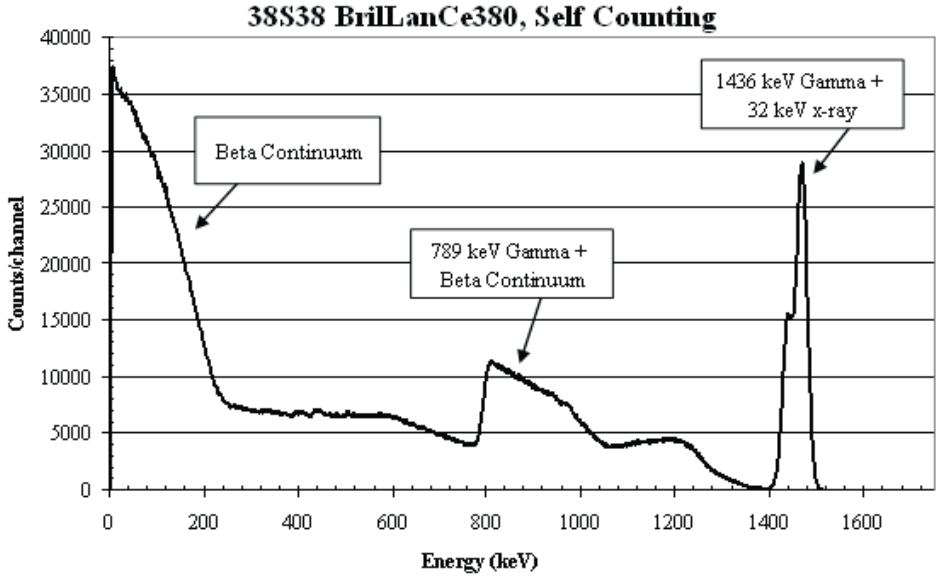

Figure 3.6: Spectrum of internal radiation from BrilLance, Lanthanum decay.

The gamma peak from EC is used to set an energy scale for each integrated pulse.

The spectra was obtained at three different voltages; 1.3 kV, 1.4 kV and 1.5 kV to calculate the energy resolution at the 1.4 MeV peak. The Anode voltage was supplied by a High Voltage Power Supply Module N472 and an Oscilloscope Lecroy WX-440 was used as acquisition system. The table 3.2 summarizes the values for energy resolution calculated at Full Width at Half maximum (FWHM) for this peak.

Once the polarization voltage is set, the scale of energy can be obtained with the self-counting spectrum. The maximum of the pulse for events with energies at 1447 keV is 482 mV, therefore the maximum for a photon with 662 keV will be 220 mV. Having that numbers we set the acquisition windows on the Oscilloscope, with a voltage range of 0 to 800 mV and a threshold level of 80 mV for La decays. Due to the minimum threshold at this voltage range, photons with energy below < 240 keV are not registered.

The Figure 3.7 shows the spectrum from the internal radiation measured at 1.5 kV. For the self-count measurement the detector was placed outside the bunker, hence no irradiation from Cs-137 is present on the spectra.

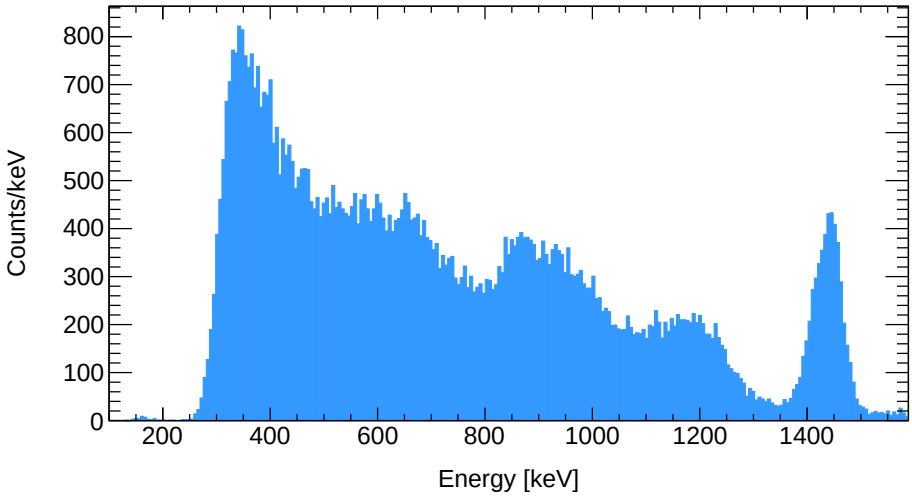

Figure 3.7: Spectra of internal radiation from BrilLance380, obtained from integrated pulse (charge distribution) and calibrated with a gaussian fit from the 1.4 MeV photopeak.

3.3. Measurements

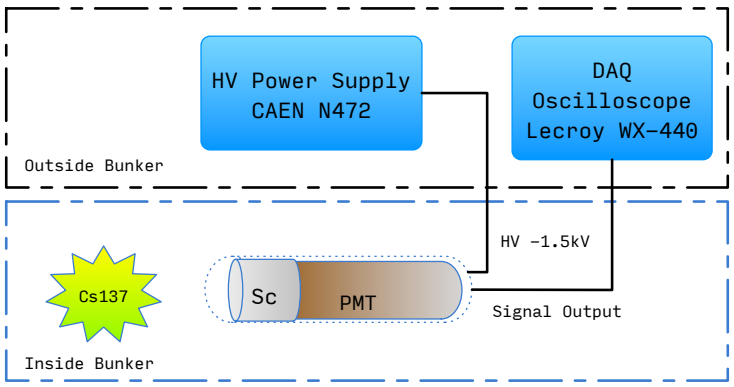

Figure 3.8: Spectrometer inside bunker, at 1.3 m from source.

The irradiation source is available 6 days a week with one day off for entering the bunker. The radiation source is kept with attenuation filter 1 the longest possible, due to many users with their detector testing for radiation aging. However one day per week or just the afternoon it is possible to make a filter scan, in agreement with the rest of the users. Hence, the choice of a specific filter was a difficult task. The measurements were done from the highest attenuation filter until a level of pile-up events no more than 5 per acquisition window (500 ns).

The rate was measured for every single filter configuration. The pulses coming from the PMT goes to a discriminator module with 70 ns gate. The events with energy of 662 keV have an amplitude of -220 mV, however the minimum threshold allow for this discriminator module it was -150 mV, hence the counting rate stand for photons with energy higher than 450 keV. The table 3.3 summarize all the attenuation filters con-

A	B	C	Attenuation	Rate (scaler)[kHz]	Rate Estimated [kHz]
100	100	4.6	46000	.555	6.58
100	100	2.2	22000	1.190	13.76
10	100	1	1000	25.62	302.79
1	100	4.6	460	59.1	658.24
1	100	2.2	220	127.2	1376.33
1	100	1	100	288.4	3027.92

Table 3.3: Filter configurations

figurations performed, rate expected and measured. The expected rate is estimated by considering the activity of the source, the geometrical acceptance of the detector and the detector efficiency for gammas of 662 keV.

The voltage range was set from 0 to 400 mV (220 mV Cs peak) and the trigger was set with minimum threshold possible for this range (30 mV). Due to this threshold all events below 90 keV were not registered.

Around 100k events were registered for each filter configuration. With this amount of events it possible to find at least 80% of single pulse events for the highest intensities.

The next section shows the analysis for single pulse events and the treatment to determine the number of peaks is explained on the Pile-up reconstruction section.

3.4. Single pulse analysis

3.4.1. Pulse Shape

As explained in previous sections, all the events were registered with an oscilloscope within a time window of 500 ns. A pulse shape was obtained with the lowest intensity (46.000 att. factor), to understand rise time and fall time and hence, provide a appropriate integral time window. While the rise time $\tau_r = 4$ ns the decay time is $\tau_d = 28 \pm 3.5$ ns, therefore a gate of 150 ns is enough to provide an integral from the pulse and then obtain its charge. The Figure3.9 shows the average waveform shape for the lowest intensity.

The time to register each configuration was limited and depending on the rest of the working users. However, the amount of samples registered was around 100k (with one or more pulses).

3.4.2. Discrete Wavelet Transform as pulse recognition filter

One of the main problems faced by any detector is when the particle rate to detect overpass the intrinsic maximal count rate (time decay). Usually the maximal count rate (n) for any detector is defined as a tenth of its decay constant ($n\tau_D > 1/10$). When a detector is placed in such rate conditions pile-up events are observed. To faced this problem one could either reject the pile-up events[22, 23] an hence decrease the detector efficiency or find a way to include such events. For both cases the starting point is recognize every single pulse with pile-up.

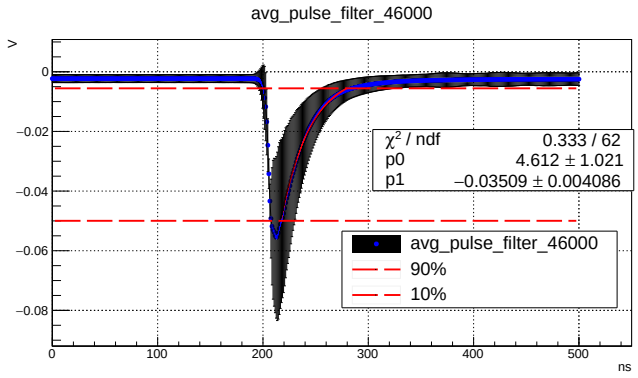

Figure 3.9: Average of 100k single pulse events from attenuation 46.000. Each sample represent the average and its deviation of the same point over the 100k events.

In our case we use a wavelet transform which has been employed in data processing algorithms for several branches of the physical sciences, including x-ray crystallography. Wavelet-base data compressing filtering algorithms are analogous to their counterparts built upon Fourier transformations. As in Fourier-based filtering, the denoised data are typically transformed back into their original (1D) coordinate space for further analysis.

For each data set a Discrete Wavelet Transform (DWT) was applied to each pulse. The DWT of a signal x is calculated by passing it through a series of filters. These filters corresponds to decompose of the signal x into two signals with detail coefficients (high filter) and approximation coefficients (low filter). Both filter are the convolution of the signal x with a family of wavelets. The simplest case is the Haar wavelets.

$$y_A[n] = \sum x[k]g[2n-1]$$

$$y_D[n] = \sum x[k]h[2n-1]$$

The values y_A and y_D are the approximations and detail coefficients from the signal and both signals y_A and y_D are downgrade in samples by a factor of two. For a further noise reduction, a DWT can be applied through the detailed function y_D. The Figure 3.10 shows two pulse samples from a high rate data set from GIF++. The method to recognize the pulses it was using the

3.4.3. Spectra Measurements and estimation of attenuation factors

As explained before, our goal was to determine how the attenuation change for 662 keV photons and how these filters can affect the lower energy components. The table 3.3 shows all filters used to measure the spectra and to estimate the attenuation factor between them.

The method to estimate the attenuation factor is by comparing the ratio of events above 600 keV from two different spectras with one combination of filters mentioned before and with only one layer of difference.

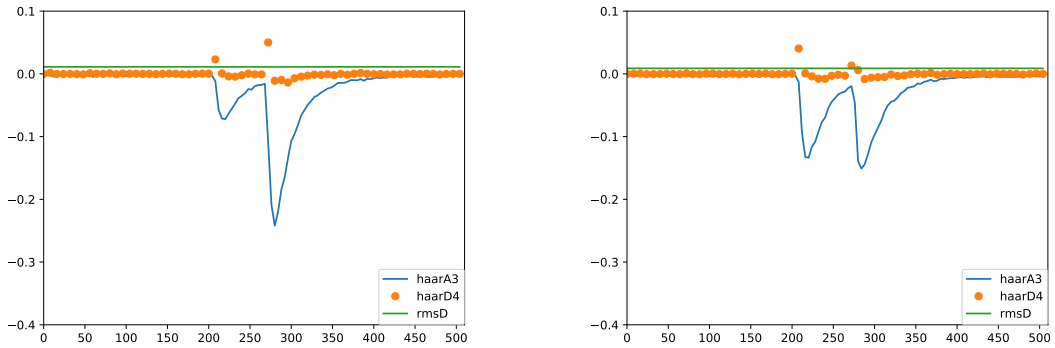

(a) Irradiator scheme **(b)** Irradiator filter system

Figure 3.10: Examples of pile-up events. The blue line represents the approximations function of the 3rd level (noised removed). The orange circles represents the detail coefficients from a four level Haar WDT, the green line is the RMS of the detail function.

Since the attenuation factors are calculated for the Cs-137 peak, it is important to remark that lead layers do not only attenuate these photons but the less energetic too and with not with the same factors. The Figure 3.11 shows the different attenuation values for a range of energy in keV. This tells us that in case of lower energy gamma the attenuation is bigger than the one for 600 keV and therefore they are highly suppressed.

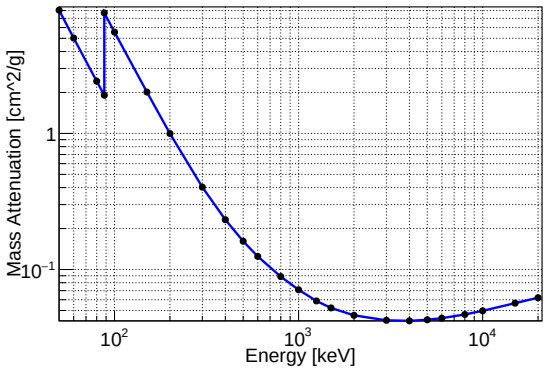

Figure 3.11: Attenuation factors for Lead. Data from NIST.

The following sections present only the spectras and afterward a summary section shows results.

3.4.4. Filter 100

The first comparison is made with two pairs of measurements with one filter of attenuation 100 between them. The first obvious observation is the no presence of the Cesium peak with the filter 46000 (Figure 3.12a) and the big amount of low energy gamma. This could be related to the presence of the lead collimator around the crystal. Secondly, with this high attenuation the number of gamma with 600 keV and above which enter straight

to crystal are highly attenuated. On the spectra from the 460 filter, the peaks appears with a 6.2% energy resolution, measured with FWHM.

Another comparison possible with a filter 100 of difference is between the filters 22000 and 220. These two spectra are shown in 3.13a and in a logarithmic scale is shown in 3.13b to better understanding . Now it is possible to observe a difference of two orders of magnitude on the photopeak and the backscatter peak at 200 keV is distinguishable for the attenuation 220.

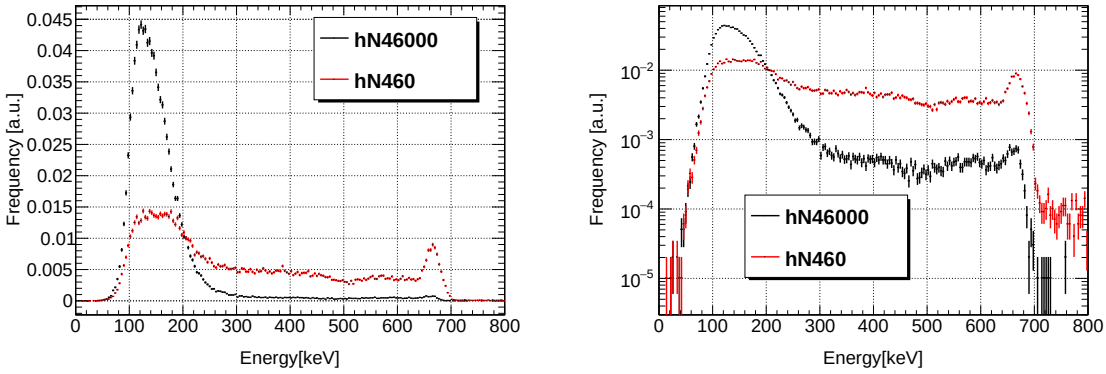

(a) linear **(b)** Log plot of the same comparison.

Figure 3.12

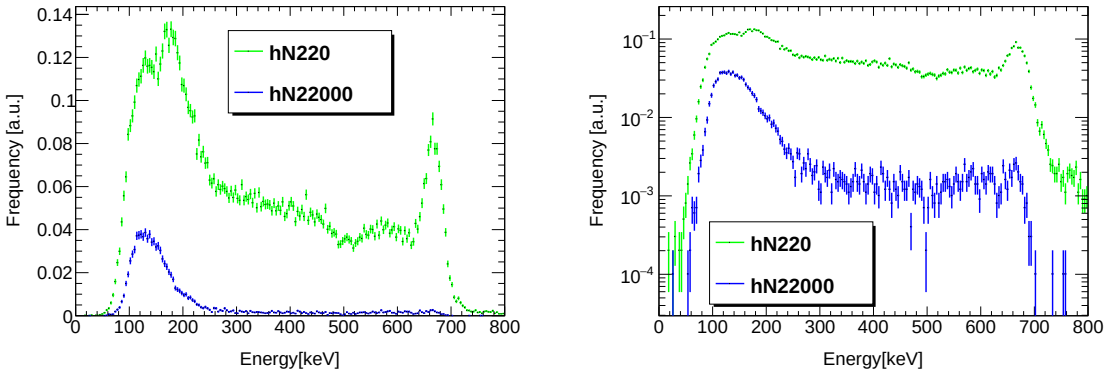

(a) linear **(b)** Log plot of the same comparison.

Figure 3.13

3.4.5. Filter 10

On the next filter comparison, all the attenuation factors are related to the highest intensity measured with filter 100. At this intensity the pile-up effect is appreciable and therefore the resolution is lost by a 4% compared to the attenuation 22000.

As we increase the intensity, the Compton continuous(200 keV to 600 keV) increases too, however the photo peak begins to decrease and loss resolution.

A similar situation is observed on the filter comparison 4.6 and 2.2.

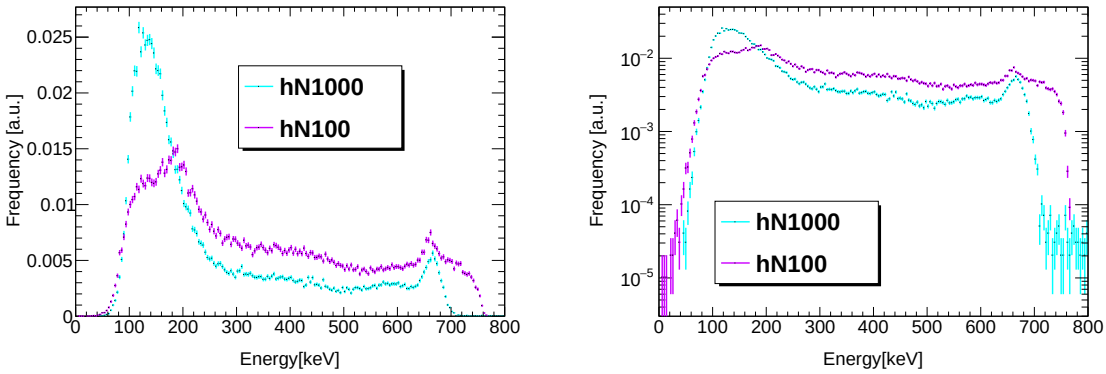

(a) linear **(b)** Log plot of the same comparison.

Figure 3.14

3.4.6. Filter 4.6

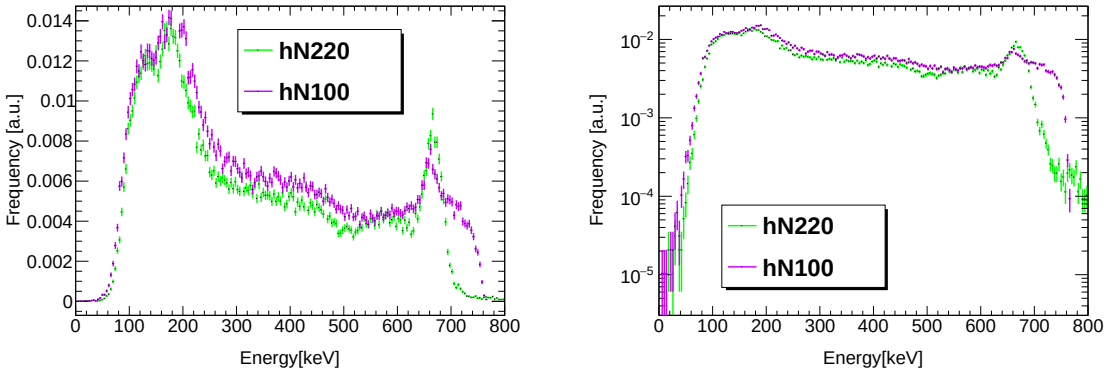

(a) linear **(b)** Log plot same comparison.

Figure 3.15

3.4.7. Filter 2.2

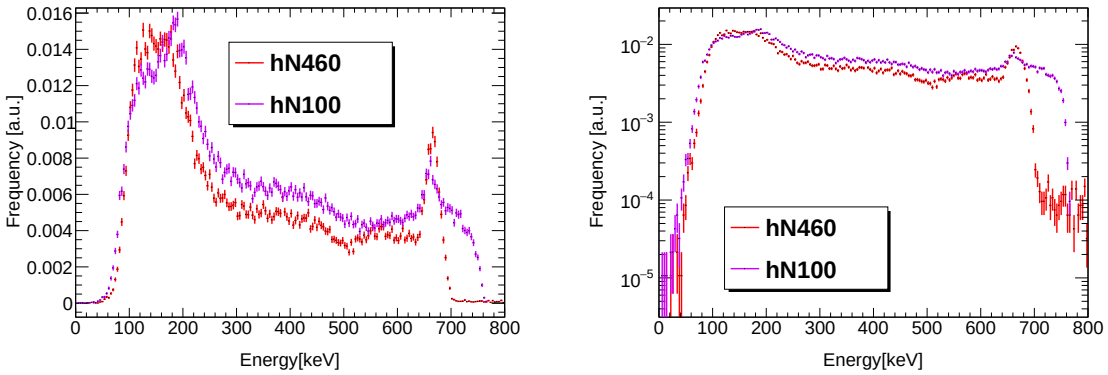

(a) linear **(b)** Log plot same comparison.

Figure 3.16

3.5. Summary

In order to estimate the attenuation factors we integrate the spectra for energy values from 600 keV until 700 keV for both spectra. The ratio of these two numbers represent the attenuation factor for the photopeak. For the attenuation filter 10, there are two pairs of spectra, however only the second one is used due to the no presence of the photopeak on the filter 46000.

The following graph shows the relation between the measured values compared to the nominal ones given by GIF++ facility. Clearly the relation is not linear and the measured values are lower for all the cases. The quadratic relation is not only affected by the presence of the collimator on the crystal but also by the surrounding materials, e.g. Housing tube, aluminum frames from the sTGC, aluminum windows from the source, air, etc.

It is also possible to compare the dose attenuation from the spectra, however the situation looks similar. The filter 10 shows an attenuated dose of 37.33 while the value provided by the simulation is 72.3. These factors are calculated for dose attenuation from the photopeak region.

The possible reasons for this disagreement could be many as the background sources present inside the bunker, but one big factor was the thickness of the lead collimator inside the tube. This piece affects highly the free entrance of gammas and hence the shape of the spectra change considerably.

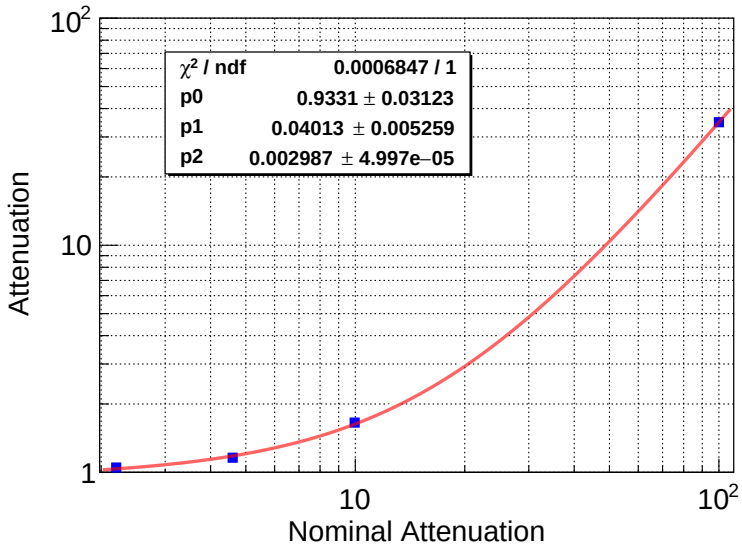

Figure 3.17

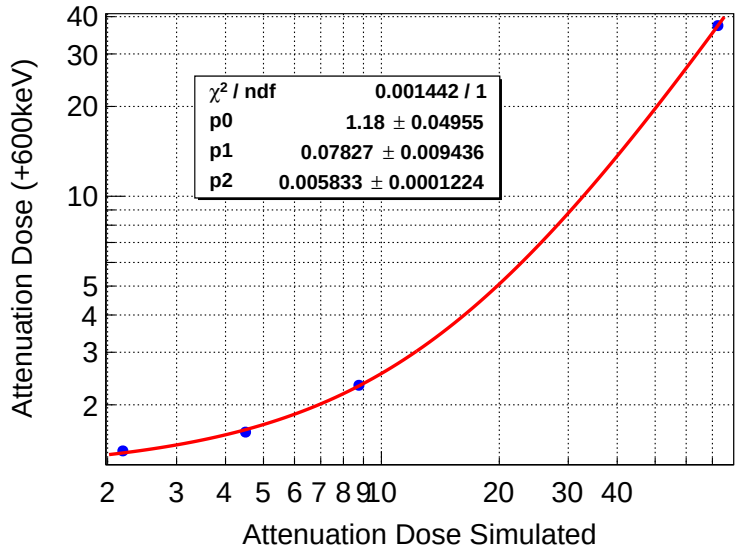

Figure 3.18

4. Synchrotron Radiation Detector for electron tagging

Many high energy experiments require pure electron beams. Despite the steady improvement of the beam lines, it is still very difficult to obtain a small percentage of contamination. The NA64 experiment[24] at CERN provides such an example, in which it is mandatory to suppress hadron and muon contamination in the electron beam, since such particles can generate irreducible background processes mimicking the experimental signature of a dark photon [25, 26].

NA64 uses 100 GeV electrons from beam lines provided by the Super Proton Synchrotron (SPS) at CERN, which is one of the best existing beam lines at this energy in terms of beam purity[27]. Since the electrons are secondary particles from the proton beam at the SPS, the experiment uses magnets to remove the remaining hadrons (pions and kaons) and some low-energy electrons from the interaction with passive material along the beam line. However, a presence of hadrons still remains at the level of 10^{-2}, hence the experiment uses the synchrotron radiation to tag the incoming electrons and to reject the other events.

In this chapter we start by briefly describing the NA64 experiment goals, the physics motivation for searching dark photons in this region and the advantage of this configuration.

The experiment has two different configurations for two possible dark photon decays; *visible* and *invisible* mode. These two configurations are discussed, however the focus goes on the *invisible decays*, where first results are shown.

To detect a dark photon signal, the level of hadron contamination must be reduced to the level of 10^{-5} without compromising the electron efficiency below 95%. For this purpose, the experiment must apply a particle identification technique, e.g. Cherenkov radiation counters.

A brief discussion about the difficulties of using Cherenkov radiation as particle identification technique is presented and how the synchrotron radiation (SR) is the key for this energy range.

For detecting SR, three alternatives were tested in the experiment during the first run in 2015. Performance and results are shown for detectors named BGO and LYSO. These two synchrotron radiation detectors (SRD) are made of scintillator crystals, assembled in different configurations and geometries. The main alternative used by the NA64 collaboration is an array of eight BGO (Bismuth germanium oxide) crystals, where results from

the first run are shown. The second alternative is a device designed and assembled at the Universidad Tecnica Federico Santa Maria, a detector with a crystal matrix of 25x25 LYSO (Lutetium-yttrium oxyorthosilicate) crystals. This high granularity configuration can provide energy profile in 2 dimensions and due to its shorter time decay constant compared to BGO, the LYSO detector could work under higher beam intensity.

A method to suppress the hadron contamination by using the SR is presented, comparing results from the two devices mentioned before.

Finally the results from dark missing energy events of dark photons in the invisible mode configuration are presented.

4.1. NA64 experiment

The NA64 experiment is a fixed-target experiment at the CERN SPS combining the active beam dump and missing energy techniques to search for rare events.

The experiment uses the H4 line from SPS, where H stands for hadrons which are produced by the interactions of protons on a Beryllium target T2 upstream. Afterwards, the hadrons which are mainly pions are evacuated into the beam line, tuned to a freely adjustable beam momentum from 10 GeV/c to 300 GeV/c. The pion beam can be converted into electrons after hitting a removable thin lead plate. The maximal beam intensity of electrons at 100 GeV/c is $\simeq 10^6$ e/s for typical SPS spill with 10^{12} protons on target, see Figure 4.1. Typically there are two spills per minute and the spill duration is 4.8 s.

A fully hermetic detector is placed on the H4 beam line with the primary goal to search for light dark bosons from dark sector that are coupled to photons, e.g. dark photons (A'), or sub-GeV boson (Z') coupled only to quarks. In some cases the Z' is coupled only to μ or τ, so we call the Z' the dark leptonic gauge boson. The experiment is also capable to search for $K_L \rightarrow$*invisible* decay, which is complementary to $K^+ \rightarrow \pi^+ + \nu\nu$, and invisible decays of π_0, η, η', K_S mesons[28, 29].

The use of a fixed target experiment to detect rare events does not only have the advantage of the high luminosity compare to colliders experiments, it also offers the possibility to search for missing energy events due to the full hermeticity. The missing energy events could be dark photon decays into a non-SM particles, such as dark matter. The advantage of this approach is that the sensitivity (or number of signal events) of the experiment is roughly proportional to the A' coupling squared ϵ^2, associated with the A' production in the primary interaction in the target, while in a classical beam dump experiment searching for SM particles decays, it is proportional to ϵ^4; one ϵ^2 comes from the A' production, and the other ϵ^2 comes either from the probability of A' decays or their interactions in a detector located at a large distance from the beam dump.

The sensitivity of these two methods depends on the region under study in the (ϵ^2, $m_{A'}$) parameter space, background level for a particular process and available beam intensity (Figure 4.1).

One of the main background sources in the experiment is related to the possible presence of the low-energy tail in the energy distribution of beam electrons. This tail was observed during irradiation of the setup by the 100 GeV electron beam without switching

on the deflecting magnet. This tail is caused by the electron interactions with passive material, e.g. as entrance windows of the beam lines, residual gas, etc. Another source of low energy electrons is due to the presences of pions or muons on the beam line and their decays in-flight.

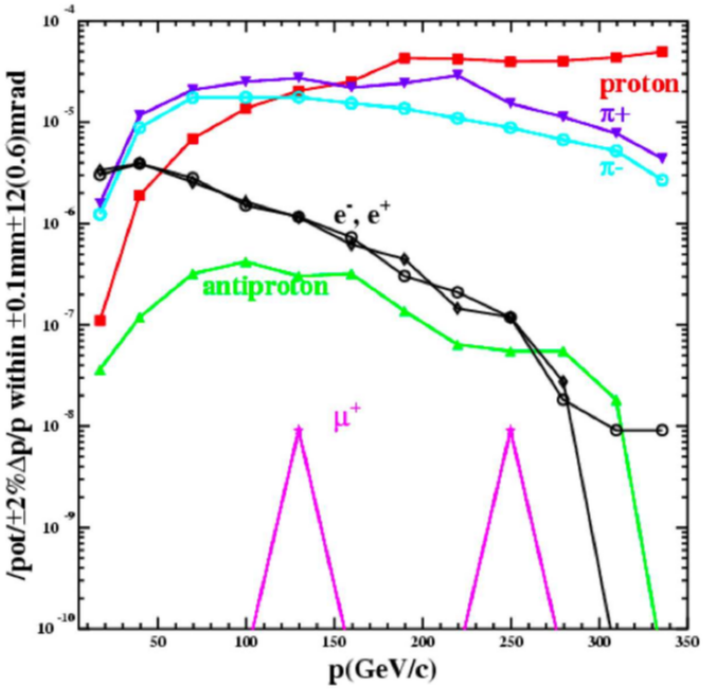

Figure 4.1: Beam intensity of different particles coming from target T2 at SPS (H4 beam line). The intensities are relative to the proton beam on T2 (10^{12}). Hence for 100 GeV/c electrons the intensity is a couple of millions per second. Picture from SPS webpage.

The uncertainties arising from the lack of knowledge of the dead material composition in the beam line are potentially the largest source of systematic uncertainty in accurate calculations of the fraction and energy distribution of these events. Hence, the sensitivity of the experiment could be determined by the presence of such electrons in the beam, unless one takes special measures to suppress this background. To reject these background sources at high energies by using standard techniques such as threshold Cherenkov counters is impossible, see Section 4.6.1.

To improve the high energy electrons selections and to suppress background from the possible admixture of low energy electrons, we use a tagging system utilizing the synchrotron radiation (SR) from high energy electrons deviated by a dipole magnet, installed upstream of the detector. This technique will allow us to suppress the hadron contamination by 5 orders of magnitude.

4.2. Physics Motivation

The most general low energy extension of the Standard Model is the so-called dark sector due to its extremely weak interaction with the known sector. The connection between the standard sector and the dark sector is usually done through a *mediator* - a particle which possesses both Standard Model and dark sector quantum numbers.

Depending on the type of the mediator, a few "portals" to the hidden sector could be identified:

- Scalar portal:
  The most general scenario employing an additional scalar particle is through its interactions with the Standard Model Higgs boson. This includes both operators of third and fourth orders resembling the Higgs potential in the Lagrangian:

$$\mathcal{L} \sim \mu S H^+ H + \lambda S^2 H^+ H \tag{4.1}$$

  The best way to look for such type of new particles is through the study of Higgs decay final states and Higgs properties, the most appropriate machines to address this scenario are the high energy colliders, such as the LHC.

- Pseudoscalar portal:
  A possible solution to the strong Charge Parity (CP) problem is the introduction of a new Peccei-Quinn $U(1)$ symmetry which is broken spontaneously. The pseudo Nambu-Goldstein boson of this breaking is the axion. The interaction between the axion and the Standard model fermions is given by:

$$\mathcal{L} \sim \frac{\partial_\mu a}{f_a} \bar{\psi}_f \gamma^\mu \gamma_5 \psi_f \tag{4.2}$$

- Neutrino portal:
  The existing puzzle in the neutrino mass sector provides input for a few interesting models explaining this phenomena. The possible existence of a sterile neutrino (a type of neutrino that does not interact with fundamental forces from SM, except for the gravity) may lead to the addition of Yukawa term:

$$\mathcal{L} \sim Y_N L H N \tag{4.3}$$

  This sterile neutrino is the SM singlet and could have been produced in the early Universe. If the relic abundance and interactions strength with the dark matter are sufficient, they will delay the DM kinetic decoupling and will allow the solution for the problem of missing-small structures like satellite galaxies[30].

- Vector portal:
  The most general interaction of an electrically neutral vector particle A' with the SM fermions can be written in the form:

$$\mathcal{L} \sim g' q_f \bar{\psi}_f \gamma^\mu \psi_f A'_\mu \tag{4.4}$$

where g' is the universal coupling constant of the new interactions and q_f is the corresponding charge of the interacting fermions.

4.3. Dark photon

The origin of the coupling of A' (dark photon) to the fermion fields could arise in various models. Since almost any extension of the Standard Model introduces new symmetries and gauge groups, the wide range of possibilities goes from maximally models to including only single type of fermions or even a single generation.

One of the best motivated dark photon models is the so-called kinetic mixing model, in which a new $U(1)_D$ group is introduced, responsible for the interactions between the particles in the dark sector. It mirrors the hypercharge interactions of the SM particles and its carrier, the dark photon could mix with the ordinary photon as follow:

$$\mathcal{L}_{\text{int}} = -\frac{\epsilon}{2} F_{\mu\nu} F'^{\mu\nu}, \tag{4.5}$$

where $F_{\mu\nu}$, $F'^{\mu\nu}$ are the ordinary and the dark photon fields respectively, and parameter ϵ is their mixing strength. The kinetic mixing of Eq. (4.5) can be diagonalized resulting for a massive A' in a non diagonal mass term and $\gamma - A'$ mixing[31].

The mixing term $\frac{\epsilon}{2} F_{\mu\nu} F'^{\mu\nu}$ after breaking the symmetry results in the interaction $\mathcal{L} = \epsilon e A'_\mu J^\mu_{em}$, of dark photons with the electromagnetic current J^μ_{em} with a strength ϵe, where e is the electromagnetic coupling and $\epsilon \ll 1$. Therefore, any source of photons could produce a kinematically permitted massive A' state according to the mixings.

The mixing strength may be as large as $\epsilon \simeq 10^{-5} - 10^{-3}$, which makes experimental searches for A's interesting [6, 7]. Then, depending on the A' mass, photons may oscillate into dark photons -similarly to neutrino oscillations- or, the A's could decay, e.g., into e^+e^- pairs.

The complete Lagrangian for this type of mixing would be:

$$\mathcal{L} = \mathcal{L}_{SM} - \frac{1}{4} F'_{\mu\nu} F'^{\mu\nu} + \frac{\epsilon}{2} F'_{\mu\nu} F^{\mu\nu} + \frac{m^2_{A'}}{2} A'_\mu A'^\mu + i\bar{\chi}\gamma^\mu \partial_\mu \chi - m_\chi \bar{\chi}\chi - e_D \bar{\chi}\gamma^\mu A'_\mu \chi, \tag{4.6}$$

where the massive vector field A'_μ is associated to the spontaneously broken $U_D(1)$ gauge group, $F'_{\mu\nu} = \partial_\mu A'_\nu - \partial_\nu A'_\mu$, e_D is the coupling constant of the $U(1)_D$ gauge interactions, $m_{A'}$, m_χ are the masses of the dark photons and dark matter particles, respectively.

Here, we consider as an example the Dirac spinor fields χ which are treated as Dark Matter fermions coupled A'_μ by the dark portal coupling constant e_D. If A' is the lightest boson in the dark sector, then its decay will be mainly visible, typically into leptons (or hadrons), if not it will decay into dark matter particles, hence invisible decay. These two decay modes (*visible* and *invisible*) lead to two different dark photon signals.

4.4. Dark Photon signal

The detection of this dark boson will depend from whether it is the lightest particle from its family or not. As is mentioned before, if A' is the lightest boson in the dark sector, then its decay will be mainly in SM particles (visible decay), however in the presence of lightest dark states of χ, where $m_\chi < m_{A'}/2$, the dark boson would predominantly decay in these **invisible** states, with a coupling $e_D > \epsilon e$.

The decay rates of $A' \to \bar{\chi}\chi$ and $A' \to l^- l^+$ are given by:

$$\Gamma_{A'\to l^+l^-} = \frac{1}{3}\alpha\epsilon^2 m_{A'}\left(1+\frac{2m_l^2}{m_{A'}^2}\right)\sqrt{1-\frac{4m_l^2}{m_{A'}^2}} \tag{4.7}$$

$$\Gamma_{A'\to\bar{\chi}\chi} = \frac{1}{3}\alpha_D m_{A'}\left(1+\frac{2m_\chi^2}{m_{A'}^2}\right)\sqrt{1-\frac{4m_\chi^2}{m_{A'}^2}} \tag{4.8}$$

The oscillations of photons into dark photon $\gamma - A'$ could produce a kinematically permitted massive A' state according to the mixing. Therefore, any source of photon could produce A', except for the low interaction strength ϵ.

The experiment NA64 uses A' bremsstrahlung as physics process to detect the dark photon. The interaction of electrons through an active target (nucleus) provides a photon interaction which can eventually decay in A'. The process will follow:

$$e^- + Z \to e^- + Z + A' \tag{4.9}$$

Eventually, A' will decay in visible or invisible states. The total number of A's produced by n_e electrons in a target with thickness $t \gg X_0$ is[6]:

$$n_{A'} \sim C n_e \frac{\epsilon^2 m_e^2}{M_{A'}^2}, \tag{4.10}$$

Compared to the electron bremsstrahlung, A' is suppressed by $\epsilon^2 m_e^2/M_{A'}^2$.

The region of interest for the experiment is within $\epsilon \simeq 10^{-5} - 10^{-3}$ and for massive photon with $M_{A'} \leq 1\,\mathrm{GeV}$. Therefore, for a parameter space region of our interest it is expected to occur with the rate $\leq 10^{-13} - 10^{-9}$ in respect to the ordinary photon production rate.

The energy spectrum will depend on the fraction of A' energy ($E_{A'}$) compared to the initial electron energy E_0[32] :

$$\frac{dn_{A'}}{dE_{A'}} \sim kx\left(1+\frac{x^2}{3(1-x)}\right) \tag{4.11}$$

where k is constant, $x = E_{A'}/E_0$.

The emission of A' is expected to be collinear with respect to the beam[6]. The decay length will depend on the electron energy E_0 and is shown in Figure 4.2.

It is possible that one of these two channels, visible and invisible, can be suppressed, therefore the detector could be configured according to the dominant channel $\Gamma_{\text{visible}}/\Gamma_{\text{tot}} \simeq$

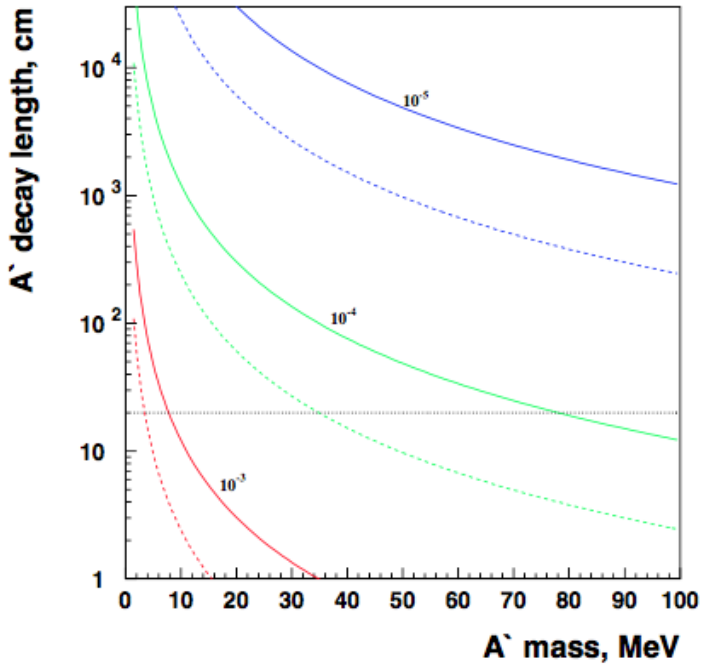

Figure 4.2: The A' decay length as a function of its mass calculated for different $\gamma - A'$ mixing values indicated near the curves. The solid line is for 150 GeV and the dashed line is 30 GeV of E_0. The horizontal line indicates the approximate length of the designed calorimeter ECAL1 ≃200 mm

1 or $\Gamma_{\text{invisible}}/\Gamma_{\text{tot}} \simeq 1$. The next two sections explain the two possible detector configurations.

4.4.1. Visible decay

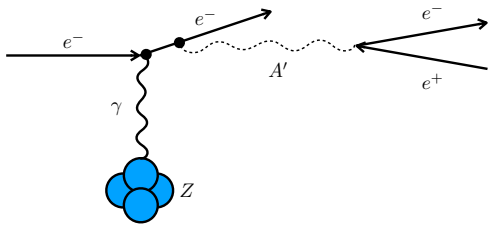

Figure 4.3: Diagram illustrating the massive A' production in the reaction $e^-Z \to e^-ZA'$ of electrons scattering off a nuclei (A, Z) with the subsequent A' into an e^+e^- pair.

If it is assumed that the decay $A' \to e^-e^+$ is dominant, then $\frac{\Gamma(A' \to e^-e^+)}{\Gamma_{\text{tot}}} \simeq 1$ and the decay is totally visible. The process of dark photon production will be by A'-strahlung and after a few centimeters, the dark photon will decay into electron-positron pair (see Figure 4.3).

The detector configuration for such process requires a coincidence system with scin-

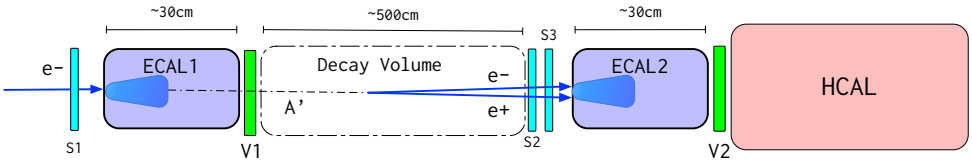

Figure 4.4: Illustration of detector configuration for visible decay of dark photon.

tillators named **S2** and **S3** (in light blue in Figure 4.4), **S1** provides the trigger.

The interaction happens in the first X_0's of the active target named **ECAL1** (Tungsten electromagnetic calorimeter) where the dark photon is produced, hence no events are expected in the veto **V1**, afterwards $\sim 420\,\text{cm}$ of a decay volume allows the dark photon decay into an electron-positron pair.

A fraction (f) of the primary beam energy $E_1 = fE_0$ is deposited in the ECAL1. The remaining part of the primary electron energy $E_2 = (1-f)E_0$ is transmitted by A' which decays in-flight in the Decay Volume. The two leptons cross the coincidence system (S2 and S3) and afterwards they deposit their energy as an electromagnetic shower in the **ECAL2** of around $40X_0$.

At high A' energies $E_{A'} \leq 30\,\text{GeV}$, the opening angle $\Theta_{e^-e^+} \simeq M_{A'}/E_{A'}$ of the decay e^-e^+ pair is too small to be resolved in two e-m showers in the **ECAL2**, so the pairs are mostly detected as a single electromagnetic shower. At distances larger than 5 m from the **ECAL1**, the distance between the hits is $\leq 5\,\text{mm}$, so the e^-e^+ pair can be resolved in two separated tracks in the **S3** and **S2**.

The signal candidate events have the signature:

$$\text{S}_{\text{A}'} = \text{ECAL1} \cdot \overline{\text{V1}} \cdot \overline{\text{V2}} \cdot \overline{\text{HCAL}} \tag{4.12}$$

and should satisfy the following criteria:

- The starting point of the e-m shower in the ECAL1 and ECAL2 should be localized within a few first X_0. Therefore, both electromagnetic calorimeters must consist of a pre-shower with $\sim 4X_0$ and $\sim 36X_0$ for energy deposition.
- The shape of both showers in ECAL1 and ECAL2 must be consistent with an electromagnetic, longitudinal and lateral shape (the fraction of the total energy deposition in the ECAL1 is $f \leq 0.8$ while in the ECAL2 $(1-f) \geq 0.2$).
- No energy deposition in **V1** and **V2**.
- The signal on the scintillator counter is consistent with the one expected from two minimum ionizing particle (MIP) tracks. At low beam energies, E_0 ≤30 GeV, two isolated hits in each counter are requested.
- The sum of energies deposited in the **ECAL1** and **ECAL2** is equal to the primary energy, $E_1 + E_2 = E_0$.

4.4.2. Invisible decay

If the boson A' is not the lightest particle from its family, it will decay eventually in other lightest states, such as dark matter particles. In that case, such particles can pass the detector being undetected. Therefore, if we assume that the visible decay is suppressed, then the invisible decay is dominant ($\Gamma_{\chi\bar{\chi}}/\Gamma_{\text{tot}} \simeq 1$).

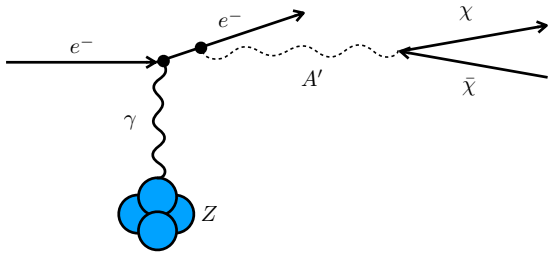

Figure 4.5: Diagram illustrating the massive A' production in the reaction $e + Z \rightarrow eZA'$ of electrons scattering off a nuclei with the subsequent A' into dark matter particles.

The production for invisible decay is a rare event with a rate of $10^{-13} - 10^{-9}$ compared to the photon production (bremsstrahlung), with a mixing strength from $\epsilon \leq 10^{-5} - 10^{-3}$ respectively. Therefore, a high number of electrons on target is needed to find such events.

The searching method for the invisible decay is the following:

The incident electron energy absorption in the ECAL is accompanied by the emission of bremsstrahlung A's in the reaction $eZ \rightarrow eZA'$ of electrons scattering on nuclei, due to the $\gamma - A'$ mixing. The diagram for the A' production in the reaction is shown in Figure 4.5.

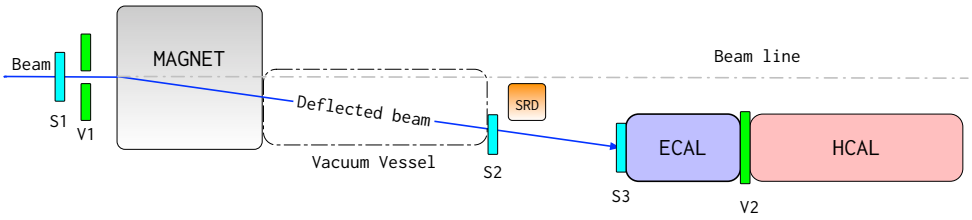

Figure 4.6: Illustration of detector configuration for invisible decays of Dark photon. The calorimeter ECAL is divided in two sections ECAL0 (preshower) and ECAL1 (calorimeter).

The reaction typically occurs in the first few radiation length (X_0) of the calorimeter **ECAL**. Hence, the **ECAL** is divided in two modules **ECAL0** with $4X_0$ and **ECAL1** with around $36X_0$ for total energy deposition.

The part of the primary beam energy is deposited in the **ECAL0**, while the remaining fraction of the total energy is transmitted by light dark matter decay particles χ through the rest of the detector. The χ penetrates the **ECAL1**, veto **V** and the hadronic calorimeter **HCAL** without interactions resulting in the missing-energy signature in the detector.

The occurrence of $A' \rightarrow \textit{invisible}$ decays produced in e^-Z interactions would appear as an excess of events with a single electromagnetic shower in the **ECAL1**, Fig. 4.6.

$$S_{A'} = \mathrm{ECAL0}(E_{\mathrm{ECAL}} > 0.5E_0) \cdot \mathrm{ECAL1}(E_{\mathrm{ECAL}} < 0.8E_0)\overline{V \cdot \mathrm{HCAL}} \quad (4.13)$$

and should satisfy the following selection criteria:

- The momentum of the incoming particle track should correspond to the beam momentum.
- The starting point of (e-m) showers in the ECAL should be localized within a few first X_0s.
- The lateral and longitudinal shapes of the shower in the ECAL are consistent with an electromagnetic one. The fraction of the total energy deposition in the ECAL is $f < 0.5$.
- No energy deposition in the V and HCAL.

An electron tagging system based on synchrotron radiation is used to improve the primary high energy electrons selection and to suppress any background. First, by bending the electron beam with a dipole magnet, as schematically shown in Figure 4.6 electrons with low momentum ($p_e < 50\,\mathrm{GeV/c}$) could be sent away from the target. Second, by detecting the energy of the SR photons one could determine the presence of hadrons due to their low power emission compared to the electrons. The **S2** and **S3** scintillators confirm the pass of an electron, while the synchrotron radiation detector **SRD** (in orange) tag the incoming photons from the beam.

4.5. Detector

The experimental setup specifically designed to search for the A' production in the reaction $eZ \to eZA'$ of high-energy electron scattering off nuclei in a high density target T is schematically shown in Fig. 4.5.

The experiment employs the upgraded H4 electron beam line at the CERN SPS described in details in Ref.[27]. The beam is designed to transport the electrons with the maximal intensity $\simeq 4 \times 10^6$ e/s per SPS spill in the momentum range between 50 GeV/c to 150 GeV/c that could be produced by the primary proton beam of 400 GeV/c with the intensity up to a few 10^{12} protons on target. The electrons are produced by protons impinging on a primary beryllium target and transported to the detector inside the evacuated beam-line tuned to an adjustable beam momentum.

The hadron contamination in the electron beam is $\pi/e < 1\%$ and since there are no special requirements for the small beam size at the entrance of the detector, which could be within a few cm^2, the beam intensity can be increased by a factor 2 by tuning the beam line optics and collimators.

The detector shown in Figure 4.8 utilizes upstream magnetic spectrometers (MS) consisting of two successive dipole magnets with the integral magnetic field of $\simeq 7\,\mathrm{T\,m}$ and a low-material-budget tracker, which is a set of Micromegas chambers, MM1-MM4

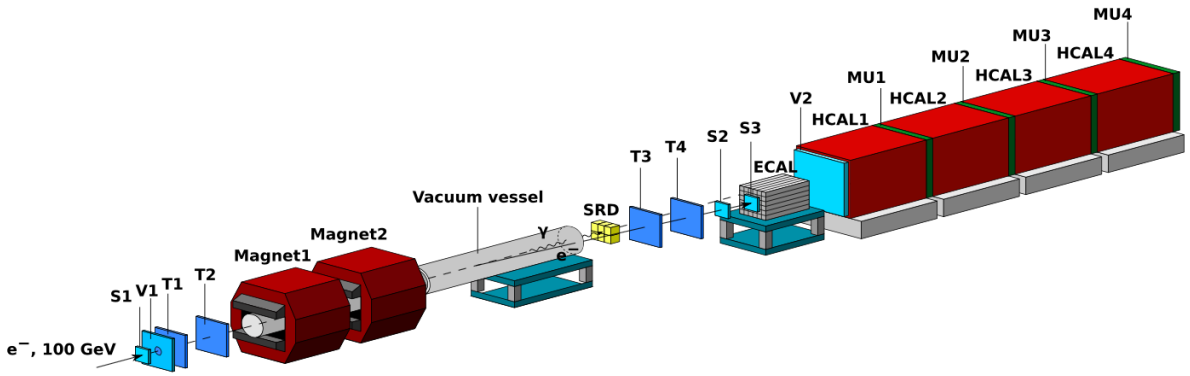

Figure 4.7: Schematic illustration of the NA64's detector, to search for $A' \rightarrow$*invisible* decays with 100GeV e^- at H4 beam line.

(**T1-T4** in the figure), allowing the reconstruction and momentum resolution at 100 GeV $\Delta P/P \sim 2\%$ for incident electrons [33].

To avoid absorption of the synchrotron radiation after the electron beam is bent, a vacuum vessel is placed between the magnets and **SRD**. The vacuum pipe with $\simeq 50$ cm diameter and 5 m length is filled with He or vacuum $\leq 10^{-3}$ mbar to minimize interactions in air. The in and output flanges are made of a thin Mylar layers, with about 20 mg/cm^2.

A beam trigger counter telescope is installed and consists of three organic scintillators **S1**, **S2** and **S3** with 42, 32 and 35 mm respectively. After the main counter **S1** a veto **V1** is placed; a scintillator squared shaped (16x16 cm^2) with a 40 mm hole. The veto prevents to fire the trigger with particles coming from the upstream interaction with the target T2, e.g muons.

Three hodoscopes are installed along the beam to prevent pile-up events. Each hodoscope consist of an X-Y array of scintillator strips with 1 mm thickness in a squared shape with 32×32 mm^2. The hodoscopes are installed after the beam counters **S1**, **S2** and **S3**.

Downstream the vacuum pipe, the SR detector is placed to tag the incoming electrons and reject low energy electrons or hadrons present in the beam. The NA64 experiment has three alternatives as a synchrotron radiation detector; the first one is an array of 6 hexagonal crystal tubes of 55 mm diameter and 200 mm length made of Bismuth Germanate named **BGO**, later explained in detail. A second option is an array of 25x25 small sized crystals (0.4x0.4x4.5 cm^3) of a Cerium doped Lutetium **LYSO** that offers high density and short decay time. The third option will not be discuss in this thesis.

The main component for the NA64 detector is the active target; a shashlik-type electromagnetic calorimeter with 6x6 cells of 38.2x38.2x490 mm^3, where each cell is made of 150 layers (1.5 mm Pb+1.5 mm Sc) resulting in a $\simeq 40X_0$. Each cell is subdivided in $4X_0$, a pre-shower (PS) part and $36X_0$ for calorimetry part (ECAL). The energy resolution obtained in the first test at 100 GeV is $\sigma_E/E \simeq 1.5\%$ which is in good agreement with $\sigma_E/E \simeq 9\%/\sqrt{E} + 0.7\%$ [34]. The electron-hadron rejection (e/π) is $\simeq 10^{-3}$ at 100 GeV.

The important characteristic feature of the ECAL is that the wavelength-shifter fibers are inserted in a spiral in order to avoid energy leak through them. Timing and energy

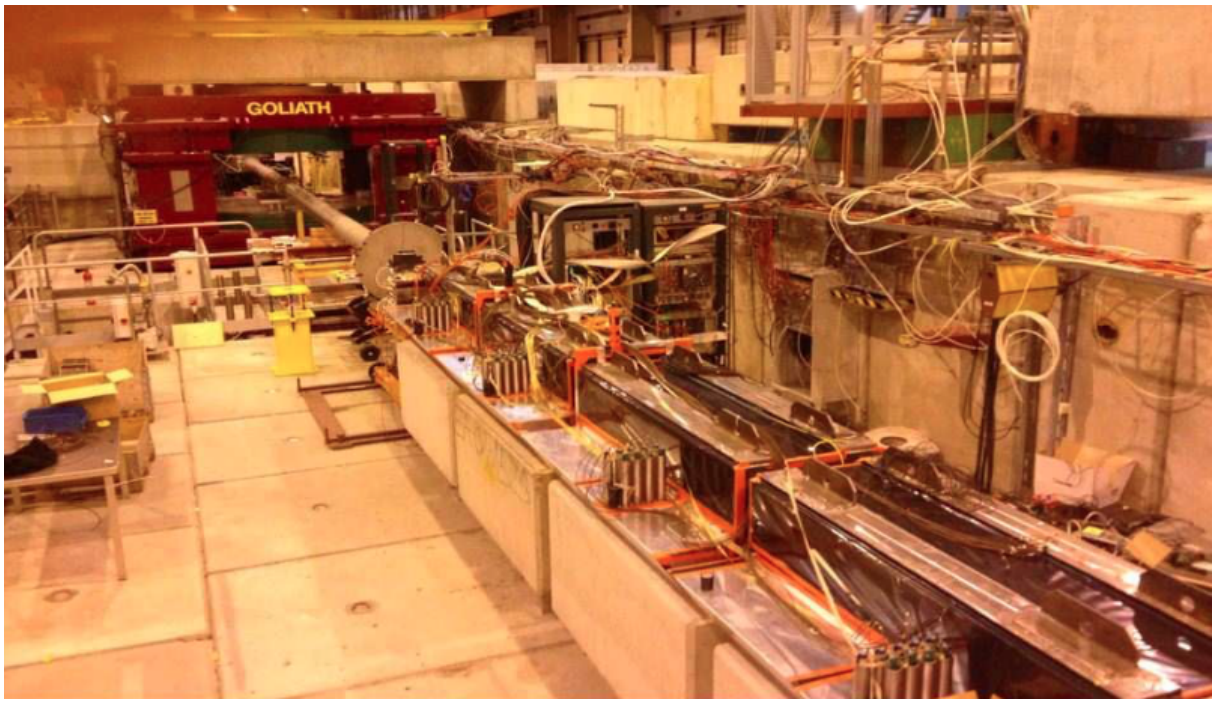

Figure 4.8: Photograph from the H4 beam line, showing the setup for the NA64 experiment. The photograph is taken looking towards upstream, with the HCAL Modules on the right side.

deposition information from each PS/ECAL module is digitized for each event.

The second main component from the NA64 detector is a high-efficiency veto counter **V2**, and a massive, hermetic hadronic calorimeter **HCAL** of $\simeq 30$ nuclear interaction lengths (λ_{int}) is positioned just after the **ECAL**. The **V2** is a plane of scintillation counters of 60x60 cm^2 with 5 cm thickness used to veto charged secondaries particles incident on the **HCAL** detector from the upstream e^- interactions. The expected MIP inefficiency is $\simeq 10^{-4}$.

The **HCAL** detector consists of four modules **HCAL1-HCAL4**, which serve as an efficient veto to detect muons or hadronic secondaries produced in the e^-Z interactions in the **ECAL** target. Each HCAL module is a sandwich of 48 alternating layers of iron and plastic scintillators with a thickness of 25 mmand 4 mm respectively, with a total length of $\simeq 7\lambda_{int}$, and with a lateral size of 60x60 cm^2. Each scintillator layer consists of 3x3 plates with WLS as optic readout allowing to assemble the whole HCAL module as a matrix of 3x3 cells, each of 20x20 cm^2. The $\simeq 30\lambda_{\text{int}}$ enhances the hermeticity of the detector, and suppresses background caused by the detection inefficiency.

4.6. The synchrotron radiation tagging system

In previous sections we have discussed the hadron contamination in the electron beam line and the presence of a tail of low momenta electrons (below 100 GeV). For the detection of the dark photon signal, it is essential to tag the incoming electrons with a precise

momentum and to reject events which can deposit low energy on the ECAL and provide a signal on the HCAL, e.g. hadrons.

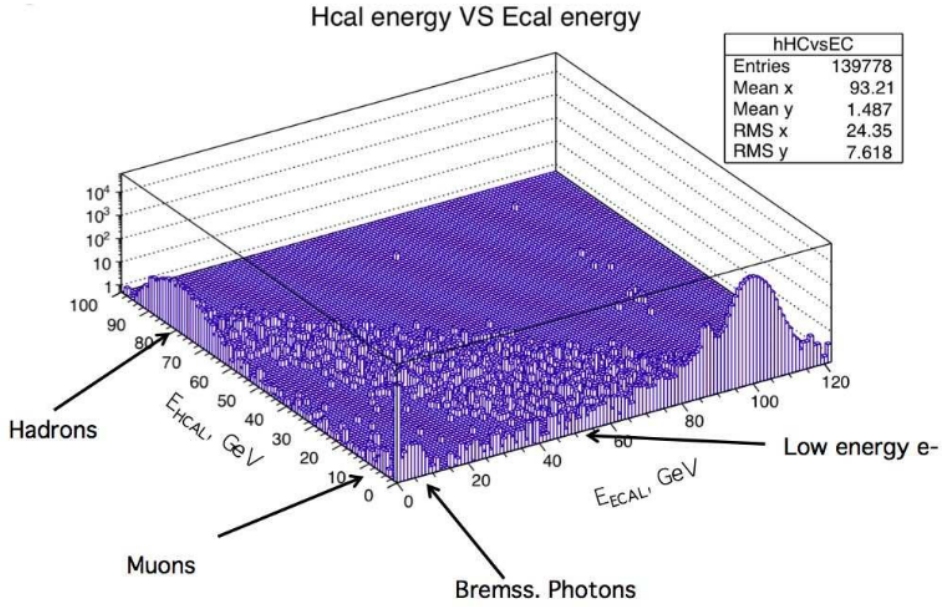

Figure 4.9: Distribution of 100GeV e^- events in the (E_{HCAL}; E_{ECAL}) plane.

The Figure 4.9 shows the distribution of events coming from the beam line with bending magnet switched off. A presence of low energy electron is seen with $E \leq 50\,\text{GeV}$ and some hadrons events with $E \sim 100\,\text{GeV}$.

This observation emphasizes the need to use a particle identification system for the experimental setup. Different standard techniques exist, and we will review two relevant ones for this energy scale.

4.6.1. Cherenkov Radiation

A common technique to identify particles is the use of Cherenkov counters which identify the particles by the emission of Cherenkov light. This type of electromagnetic radiation is emitted when a charged particle passes through a dielectric medium at speed v greater than the phase velocity of light c/n, where n is the refraction index of the medium. Since the propagation of an electromagnetic field distortion is at speed of light, it is decreased by a factor n (index refraction) in a dielectric medium, reaching values of about 75% less in a medium like water.

When a charged particle moves faster than c/n, it leaves behind an electrically polarized medium. The energy kept on the disturption is released as a photon emission with a specific wavelength.

Since the emission of this particular radiation depends only from $\beta = v_p/c$, where v_p is the particle velocity and the refraction index n, one could trigger the emission for certain particles by choosing a proper n.

For a relativistic particle the velocity β can be written in terms of its momentum p

and mass m:

$$\beta = 1/\sqrt{1 + (m/p)^2} \tag{4.14}$$

For particles with the same momentum, e.g. in a beam line, the identification could be provided by the Cherenkov condition (4.15) to distinguish two particles with different masses.

$$\frac{v}{c} = \beta > \frac{1}{n} \tag{4.15}$$

For two particles with mass $m_1 > m_2$ and same momentum the respective velocity is $\beta_1(m_1)$ and $\beta_2(m_2)$, therefore to trigger Cherenkov radiation only for the particle with mass m_1, one must choose a medium with index refraction such as:

$$n_{min} = \frac{1}{\beta_1} < n < \frac{1}{\beta_2} = n_{max} \tag{4.16}$$

This criteria becomes inefficient when the momentum of the particles goes higher, since $\beta \approx 1$ for ultra relativistic cases. In our particular case, we want to identify electrons ($m_e \approx$0.5 MeV) over hadrons (mostly charged pions, $m_{\pi^-} \approx$140 MeV) both with momenta $\approx$100 GeV. To satisfy the criteria of (4.16) we must choose an index refraction such as $n_{\pi^-} < n < n_e$, where $n_e \simeq 1.000000979$ and $n_{\pi^-} \simeq 1.00000000001$. That means we should find a dielectric medium with an index refraction close to the vacuum index but higher in an order of 10^{-6}.

4.6.2. Synchrotron Radiation

Another technique to reject heavy charged particles is the use of synchrotron radiation which exploits the high suppression of the radiated power emitted by heavier particles. The use of this technique is not new and detection of electrons or positrons in electrons beams with momenta ranging from 30 to 50 GeV was reported earlier[35, 36, 37].

Generally, radiation is emitted by any accelerated charge. For highly relativistic particles in accelerators this is referred to as synchrotron radiation. This radiation compromises electromagnetic waves emitted when a high-energy charged particles is accelerated in a direction orthogonal to its velocity, such as in a magnetic field.

The electromagnetic fields are given by:

$$\vec{E} = -\frac{\partial}{\partial t}\vec{A} - \nabla\phi, \qquad \vec{B} = \nabla \times \vec{A} \tag{4.17}$$

Here, ϕ and $\vec{A}$ are the Lienard-Wiechart scalar and vector potentials, which are given by:

$$\vec{A}(t) = \frac{e}{4\pi\epsilon_0 c}\left[\frac{\vec{\beta}}{R(1-\vec{n}\cdot\vec{\beta})}\right]_{ret}, \qquad \phi(t) = \frac{e}{4\pi\epsilon_0}\left[\frac{1}{R(1-\vec{n}\cdot\vec{\beta})}\right]_{ret}, \tag{4.18}$$

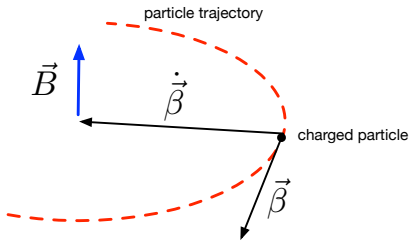

(a) Charted particle trajectory in a Magnetic field

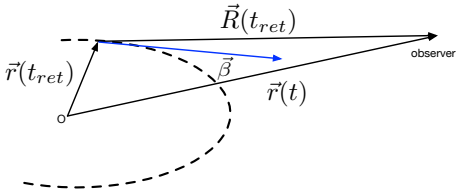

(b) Vector position in retarded potentials.

Figure 4.10

where $\vec{R}(t_{ret})$ is the distance vector from the source to the observer, and t_{ret} is the retarded time, $ct_{ret} = ct - R(t_{ret})$, and $\vec{\beta}$ is the ratio of the velocity $\vec{v}$ to the speed of light c.

Using the relation between electric and magnetic field given by the propagation of electromagnetic waves:

$$\vec{B} = \frac{1}{c}\left[\vec{n} \times \vec{E}\right]_{ret}$$

$$\vec{E} = \frac{e}{4\pi\epsilon_0}\left[\frac{(1-\beta^2)(\vec{n}-\vec{\beta})}{R^2(1-\vec{n}\cdot\vec{\beta})^3}\right]_{ret} + \frac{e}{4\pi\epsilon_0 c}\left[\frac{\vec{n}\times(\vec{n}-\vec{\beta})\times\dot{\vec{\beta}}}{R(1-\vec{n}\cdot\vec{\beta})^3}\right]_{ret} \tag{4.19}$$

This shows that for observing points far from the emitting point, the radiation field of the latter term of $\vec{E} \propto 1/R$ is more important, and the former term can be neglected. Then the power irradiated per solid angle on the observer direction ($\vec{n} = \vec{R}_{ret}/R_{ret}$) is given by:

$$\frac{dP}{d\Omega} = \left(\vec{n}\cdot\vec{S}\right)R_{ret}^2 \tag{4.20}$$

where $\vec{S}$ is the Pointing vector, $\vec{S} = \frac{1}{\mu_0}\vec{E}\times\vec{B} = \epsilon_0 c E^2\left(1-\vec{\beta}\cdot\vec{n}\right)\vec{n}$, and E is the magnitude of the electric field at a distance far from the source given in equation 4.6.2. Using this approximation the irradiated power per solid angle is given by:

$$\frac{dP}{d\Omega} = \frac{e^2}{16\pi^2\epsilon_0 c}\frac{\left(\vec{n}\times(\vec{n}-\vec{\beta})\times\dot{\vec{\beta}}\right)^2}{\left(1-\vec{\beta}\cdot\vec{n}\right)^5} \tag{4.21}$$

Depending on the angle between $\vec{\beta}$ and $\dot{\vec{\beta}}$, the irradiation power will change, however the trajectory from a charged particle inside an homogeneous magnetic field is perpendicular to the acceleration ($\vec{\beta} \perp \dot{\vec{\beta}}$). For this case the dependency on the angle θ for the irradiated power is:

$$\frac{dP}{d\Omega} = \frac{e^2\dot{\beta}^2}{16\pi^2\epsilon_0 c}\frac{(1-\beta\cos\theta)^2 - (1-\beta^2)\sin^2\theta}{(1-\beta\cos\theta)^5} \tag{4.22}$$

For the relativistic limit ($\gamma \gg 1$ or $\beta \simeq 1$), the term $(1 - \beta\cos\theta)$ becomes important for $\theta \simeq 0$

$$\frac{dP}{d\Omega} \simeq \frac{2e^2}{\pi c}\frac{\gamma^6\dot{\beta}^2}{(1+\gamma^2\theta^2)^3}\left[1 - \frac{4\gamma^2\theta^2\cos^2\phi}{(1+\gamma^2\theta^2)^2}\right] \tag{4.23}$$

Which shows that most of the radiation power is emitted when $-1 < \gamma\theta < 1$, hence the emission of the synchrotron radiation is located in very narrow angles ($\theta = 1/\gamma$).

Integrating the equation 4.23 over the solid angle, the total irradiation emission by an electron is given by:

$$P_\gamma = \frac{e^2 c}{6\pi\epsilon_0}\frac{\beta^4\gamma^4}{\rho^2}, \tag{4.24}$$

where ρ is the radius of the curvature track, $\rho = \beta E_e/eBc$, with E_e the electron energy and B the magnetic field. This expression helps us to understand the use of synchrotron radiation to identify particles with different masses. Since $P \propto m^{-4}$, there is a high suppression of the radiation power for heavier particles than electrons, e.g. pions.

Thus for relativistic π^-'s and e^-'s of the same energy, the energy loss is $(m_e/m_{\pi^\pm})^4 \sim 10^{-10}$ times less for a $\pi^\pm$.

4.6.3. Energy Spectrum of synchrotron radiation

So far we have seen the spectrum in a time domain only. To obtain the irradiation power in a frequency domain, hence the energy spectrum we apply the Fourier transform.

$$\frac{dW}{d\Omega} = \int \frac{dP(t)}{d\Omega}dt = \frac{1}{\mu_0 c}\int_{-\infty}^{\infty} |R\tilde{E}(\omega)|^2 d\omega \tag{4.25}$$

Where $\tilde{E}(\omega)$ is the Fourier transform of the electric field. Thus the energy irradiated per solid angle per frequency is given by:

$$\frac{d^2W}{d\Omega d\omega} = \frac{1}{2\pi\mu_0 c}\left|\int_{-\infty}^{\infty}(RE)e^{i\omega t}dt\right| \tag{4.26}$$

Integrating will result in a expression in terms of the Modified Bessel functions $K_i(\xi)$:

$$\frac{d^2W}{d\Omega d\omega} = \frac{e^2}{16\pi^3\epsilon_0 c}\frac{\omega^2}{\omega_c^2}\gamma^2 K_{2/3}^2(\xi)F(\xi,\theta) \tag{4.27}$$

$$\begin{aligned}
\xi &\equiv \frac{\omega}{2\omega_c}(1+\gamma^2\theta^2)^{3/2} \\
F(\xi,\theta) &\equiv (1+\gamma^2\theta^2)^2\left[1 + \frac{\gamma^2\theta^2 K_{1/3}^2(\xi)}{1+\gamma^2\theta^2 K_{2/3}^2(xi)}\right] \\
\omega_c &\equiv \frac{3c\gamma^3}{2\rho}
\end{aligned} \tag{4.28}$$

The energy spectrum per solid angle in equation 4.27 has two important features, the first one is the critical frequency (energy) defined in equation 4.28 which divides the spectrum in two halves. The second one is the maximum of the spectrum at approximately $\omega_{max} \simeq 0.3\omega_c$. Using $P_\gamma = W/T_{re}$ as the energy per revolution time T_{rev}, we can redefine W and integrating over the angles, we obtain the energy spectrum of synchrotron radiation:

$$\frac{dP_\gamma}{d\omega} = \frac{P_\gamma}{\omega_c} S\left(\frac{\omega}{\omega_c}\right) \tag{4.29}$$

$$S\left(\frac{\omega}{\omega_c}\right) \equiv \frac{9\sqrt{3}}{8\pi}\left(\frac{\omega}{\omega_c}\right)\int_{\omega/\omega_c}^{\infty} K_{5/3}(x)dx \tag{4.30}$$

The function S is shown in Figure4.11, in units of critical frequency ω_c.

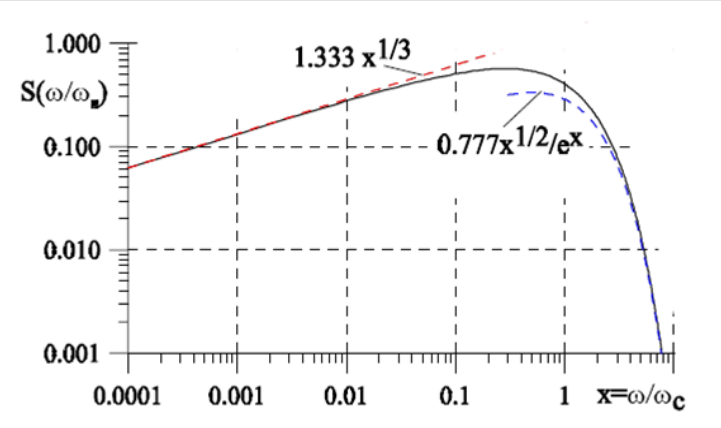

Figure 4.11: Spectrum synchrotron radiation from two different particles, where $\gamma_1 = 10\gamma_2$

Knowing the spectrum, it is possible to make a statistical treatment of our photon emission. We consider $\Pi(\varepsilon)$ the probability to emit a photon with energy $\varepsilon = \hbar\omega$. This probability depends on the ratio of the photon flux at energy ε given by $\dot{n}(\varepsilon)$ and the total photon flux $\dot{N}$. Therefore, the photon flux at energy ε is related to the spectral photon power as:

$$\varepsilon\dot{n}(\varepsilon)d\varepsilon = P_\gamma(\varepsilon)d\varepsilon = \frac{P_\gamma}{\varepsilon_c} S\left(\frac{\varepsilon}{\varepsilon_c}\right) d\varepsilon \tag{4.31}$$

where P_γ is the total power emitted (normalization constant of the power distribution) and ε_c is the critical energy $\hbar\omega_c$. Thus the photon flux at energy ε is given by:

$$\dot{n}(\varepsilon) = \frac{P_\gamma}{\varepsilon_c^2}\frac{S(\xi)}{\xi}, \quad \xi \equiv \varepsilon/\varepsilon_c \tag{4.32}$$

The total photon flux is given by:

$$\dot{N}(\varepsilon) = \int_0^\infty \dot{n}(\varepsilon) d\varepsilon = \frac{15\sqrt{3}}{8} \frac{P_\gamma}{\varepsilon_c} \tag{4.33}$$

The probability to emit a photon with energy ε is then given by:

$$\Pi(\varepsilon) = \frac{8}{15\sqrt{3}} \frac{1}{\varepsilon_c} \frac{S(\xi)}{\xi} \tag{4.34}$$

Then the mean photon energy can be written as:

$$\varepsilon_{mean} = <\varepsilon> = \int_0^\infty \varepsilon \Pi(\varepsilon) d\varepsilon = \frac{8\varepsilon_c}{15\sqrt{3}} \underbrace{\int_0^\infty S(x) dx}_{=1} \tag{4.35}$$

Therefore, by only knowing the critical energy, which depends on the γ factor, we can get the mean energy per photon. It is also possible to obtain by calculating the total power emitted divided by the total number of photons.

$$\varepsilon_{mean} = \frac{P_\gamma}{\dot{N}} = \frac{8}{15\sqrt{3}} \varepsilon_c \tag{4.36}$$

It is also interesting to calculate the number of photon emitted in a arc section from the total emitted in one turn. By using the relation 4.33 and multiplied by the time of a revolution. Then the number of photon per angle $\Delta\phi$ is:

$$\begin{aligned} N_\gamma &= \frac{15\sqrt{3}}{8} \frac{P_\gamma}{\varepsilon_c} 2\pi\rho \\ N_\gamma &= \frac{5\pi}{\sqrt{3}} \alpha\gamma \end{aligned} \tag{4.37}$$

where α is the fine structure constant.

4.6.4. NA64's tagging system

The tagging system of NA64 experiment was briefly discussed before. It consists of two dipole magnets installed in series with a total magnetic field of $B = 1.7\,\mathrm{T}$ in a $7\,\mathrm{T\,m}$ integrated field. The electron beam of $100\,\mathrm{GeV}$ is deviated $31\,\mathrm{cm}$ in over $15\,\mathrm{m}$.

The Figure 4.12 shows a scheme of the tagging system. Three sets of scintillators S_i are used to confirm the pass of the particles on the main target (ECAL). The SRD device (in orange) detects the incoming $\gamma' s$ from the $31\,\mathrm{cm}$ deviated beam. The geometrical acceptance of the different options for SR detector are the size of $\sim 10\,\mathrm{cm}$, hence over 1/3 of the radiation is within the detector acceptance.

The critical energy for this configuration is $\varepsilon_c = 11.35\,\mathrm{MeV}$ while the mean energy is about $\varepsilon_{mean} = 3.5\,\mathrm{MeV}$. The number of photon within this $31\,\mathrm{cm}$ is about 24, hence the mean energy deposited on the SRD is $\approx 29.35\,\mathrm{MeV}$.

To detect this SR, the experiment has been working to find the best suitable detector. For this task three options have been tested, three types of scintillator material; BGO,

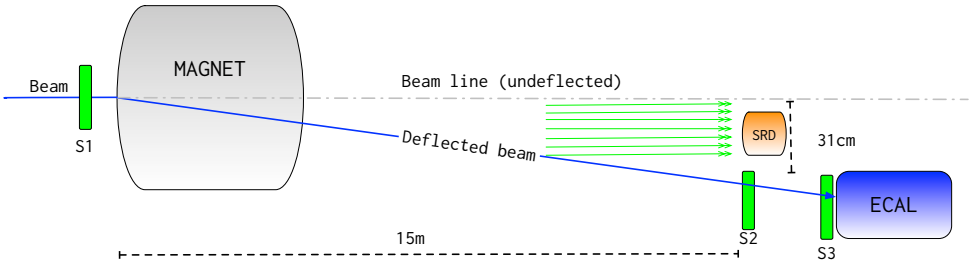

Figure 4.12: Scheme of the additional tagging of high energy electrons in the beam by using the electron synchrotron radiation in the bending magnetic dipole. The synchrotron radiation photons are detected by a γ-detector by using scintillator as BGO crystals, LYSO crystals or a different configuration with Pb+Sc. All theses options are viewed by a high quantum efficiency PMT or SiPM.

LYSO and Pb+Sc. Each one features different geometry and crystal's configuration. In this thesis we focus on two out of the three options, BGO and LYSO due to their similarities and good performance. In the next sections, we describe these detectors and we present a comparison of their use to suppress the hadron contamination on the beam line.

4.7. BGO

The NA64 experiment uses an array of eight $Bi_4Ge_3O_{12}$ (BGO) crystals as a first option of SRD due to the high photoelectric gamma rays absorption and its configuration that can detect the incoming SR and reject the back scattering events coming from the main target (ECAL). The BGO crystal has been used on tagging electron system with SR photon for electron beam[37].

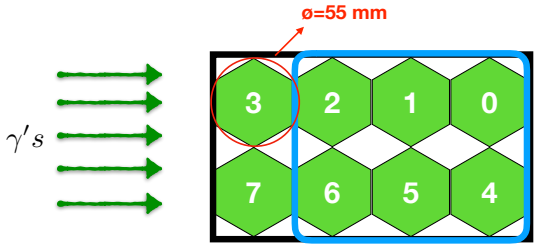

Figure 4.13: BGO detector.

The BGO crystal has a density of 7.1 g/cm^3 and because of the high atomic number of the bismuth component ($Z = 83$) it has one of the largest probability per unit volume for photoelectric absorption of gamma rays[38]. The light yield of about 8500 γs/MeV coupled to the transportation losses and quantum efficiency of the PMT gives an energy resolution of about 17% (FWHM) at 1.27 MeV (measured with a ^{22}Na radioactive source).

The detector consists of 8 hexagonal crystals with an external diameter of 55 mm and a length of 200 mm (see Figure 4.13). Each crystal is wrapped in Teflon tape for efficient

light collection and is glued to an ETL 9954 photo-multiplier (PMT), hence each crystal is read independently.

The first two crystals collect most of the synchrotron radiation spectrum. The remaining six crystals (square light blue) are affected only in case of high energy events, therefore they could serve as a shield from back-scattering particles coming from the main target (ECAL).

4.7.1. Geant4 simulations

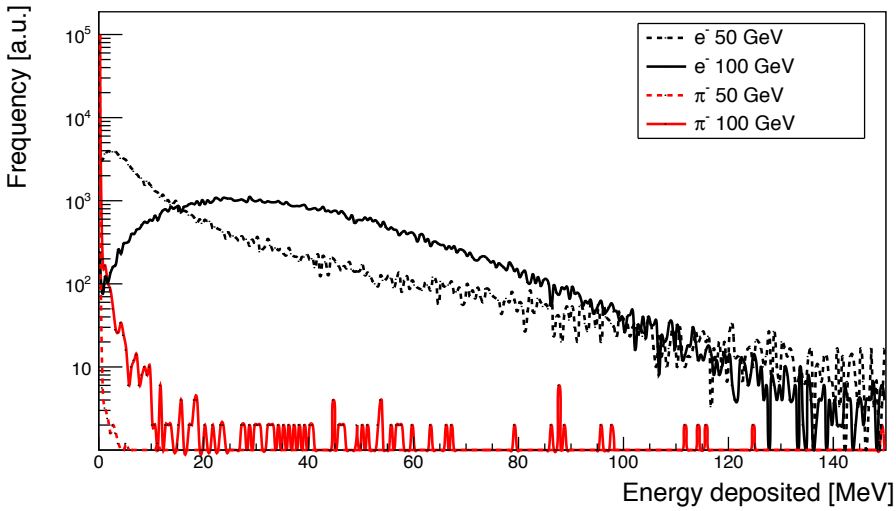

Figure 4.14: Results of the GEANT4 simulation for the energy detected by BGO for 50/100 GeV e^- (black dashed/solid line) and 50/100 GeV π^- (red dashed/solid line).

Simulations on Geant4 were performed to get the expected SR signal. The geometry of the NA64 experiment was coded in Geant4, including the 200 µm mylar vacuum windows, detailed composition of the trackers, scintillators. The residual gas was set at a level of 10^{-3} mbar as in the measurements.

The expected SR spectra for pions and electrons with energies of 50 GeV and 100 GeV are shown in Figure 4.14. The plot shows the expected dependence on the incoming electron energy in the emission spectra for realistic experimental conditions. Moreover, the comparison between the SR spectra of pions and electrons illustrates clearly the principle of this technique that allows to discriminate between them by requiring an energy threshold in the synchrotron detector. For pions, one can see that the probability of detecting an event with energy above 1 MeV (the threshold in our detector) is about $\sim 10^{-3}$ to 10^{-4}

4.7.2. Results

The gain of the PMTs was set using a 100 GeV π^- beam impinging directly on the SRD. The pions crossing the BGO have a mean energy deposition of about 60 MeV as

expected for a MIP particle.

The BGO detector was placed on the SRD position, 9 cm from the un-deflected beam axis and 9 cm from the bending beam axis. This configuration minimizes different events coming from the un-deflected beam such as, bremsstrahlung photons, neutral particles coming from the interaction on the target T2, beam interaction with detector material upstream and lastly the beam halo (about 2 cm).

The trigger was given by the coincidence of the scintillator counters S1, S2 and S3 shown in Figure 4.12. A total of 220 spills of an electron beam were recorded with an intensity of $\sim 3.4 \times 10^5\, e^-$/spill at energy of 100 GeV.

In order to reduce the pion contamination which is at level of few percent and to obtain a pure sample of electrons only, events with a total energy deposition in ECAL + HCAL above 90 GeV but with less than 20 GeV energy in the HCAL were used.

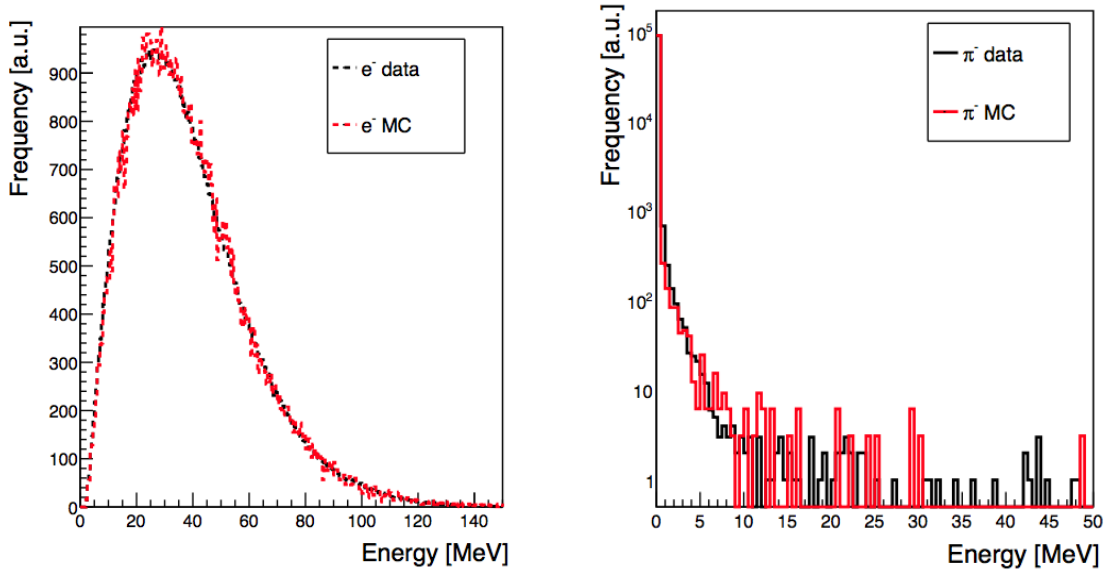

(a) SR spectrum from electron beam **(b)** SR spectrum from pion beam

Figure 4.15: Comparison between data and simulation (MC) of the SR spectrum detected for 100 GeV electrons

The spectrum of events collected with such configuration are shown in Figure4.15a and is compared with these events obtained from MC simulations.

For a pure sample of hadrons a data set with $\sim 10^5$ events were collected from a hadron beam with 100 GeV energy with an intensity of $\sim 5.4 \times 10^3\, e^-$/spill. A selection of events with energy on ECAL below 60 GeV was applied to get a pure π^- sample. The Figure 4.15b shows the spectra for this data set which decreases drastically for a few MeV.

4.7.3. Hadron suppression with BGO

The method to discriminate events from electron or hadron is based on the total energy deposited on the BGO. Although the 8 BGO crystals form part of the detector,

only the first two crystals (3 and 7 from Figure 4.13) collect most of the SR energy. We call them SRD BGO, and the last two (4 and 0) are named VETO BGO since they are affected only in case of a high energy event. Therefore, the total energy deposited is set on the SRD BGO.

The next plots show the data and the MC simulation using two criteria to count the events from electron SR and to reject the events coming from hadron SR; suppression factor.

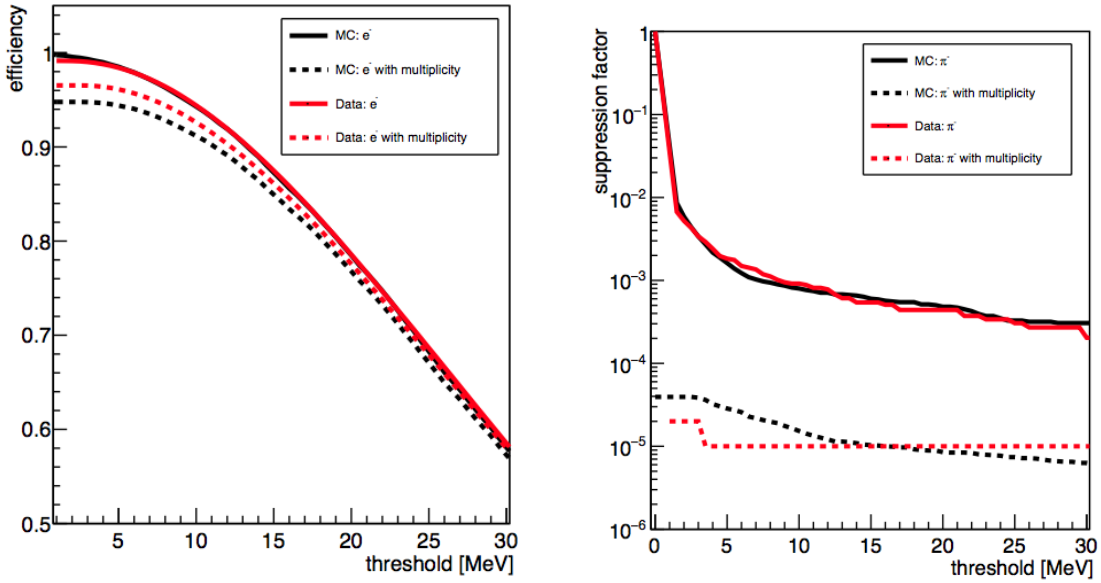

(a) Electron efficiency **(b)** Suppression factor

Figure 4.16: Comparison between data and simulation (MC) for electron efficiency as function of threshold set on the total energy and suppression factor. Both figures show the two criteria as a function of the threshold level.

The electron efficiency and hadron suppression factor are considered in two criteria:

- Threshold set on the total energy deposited in the SRD.
- Both SRD signals have to be in-time and above the threshold (multiplicity requirement).

The Figure 4.16a shows the efficiency using the two criteria, where the use of multiplicity events drops the efficiency by only a few percent for the first 15 MeV.

The contamination level using the total energy criteria can be suppressed down to a level of 10^{-3} (see Figure 4.16b), while the electron efficiency remains above 0.95. However, a much lower contamination level is required and in order to do so, the multiplicity requirement criteria is applied. On the suppression factor plot, the level of contamination is below 3×10^{-5} for a 10 MeV threshold level. This criteria rejects the knock-on electrons which hit one of the two crystals, as well as pions and muons. Results shown in this section are published in name of the NA64 collaboration in [39].

4.8. LYSO

An array of LYSO[40] crystals has been tested as another alternative for detecting SR. This array consists of 25x25 crystals of 4x4x45 mm^3. Each crystal is a Cerium doped Lutetium ($Lu_{1.8}Y_{0.2}SiO_5 : Ce$), with a light output of 32 000 γ/MeV. This type of crystal has a short time decay (see Table 4.1) compared to BGO crystals. Therefore, it is a more suitable candidate for a SR detection at higher rates. With a decay time of $\tau = 40$ ns, it could allow a maximal electron counting rate of $1/\tau \lesssim 10^7$ e/s.

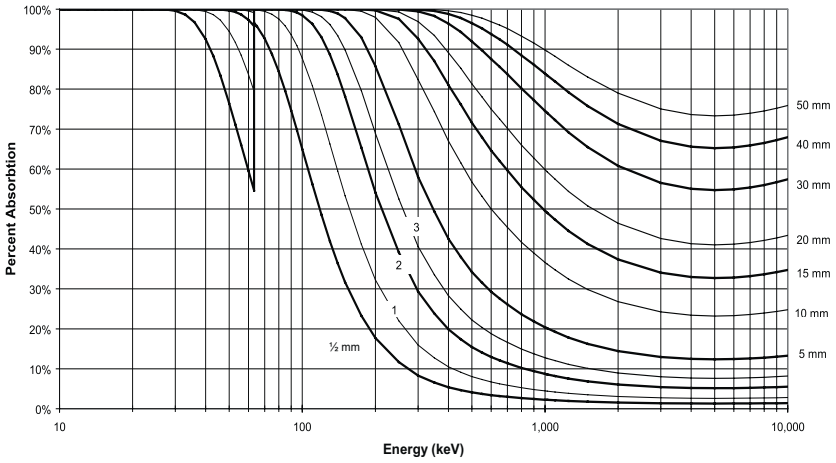

Figure 4.17: Gamma and x-ray absorption efficiency for various thicknesses of LYSO crystals[41].

The gamma absorption for 45 mm thickness ranges from 70 to 90% for the incoming SR photons (See Figure 4.17).

Property	LYSO	BGO
Density [g/cm^3]	7.1	7.1
Attenuation length for 511 keV [cm]	1.2	1.0
Decay time [ns]	41	300
Energy Resolution % at 662 keV	8.0	12.0
Light output, photons per keV	32	9
Radiation Length [cm]	1.16	0.96

Table 4.1: Property comparison LYSO and BGO crystals. Data from Saint-Gobain.

The light spectrum emission from LYSO crystals has its peak at 420 nm and is collected from a net of Kuraray Y-11 wavelength shifter (WLS) fibers. The Kuraray fiber has its maximum light absorption at 439 nm and its peak emission at 490 nm.

Each crystal is wrapped in a ultra high reflective film Vikuiti^{TM} and stacked on top of each other. The net of fibers is faced on one side of the crystals (see Figure 4.18). The WLS fibers are mounted in a ultraviolet transmitting (UVT) acrylic, with a 4 mm of separation.

An electronic board with photo counting devices is mounted for x and y readout. Each photo sensor is connected to one fiber through a lightguide (see Figure 4.19). The photo

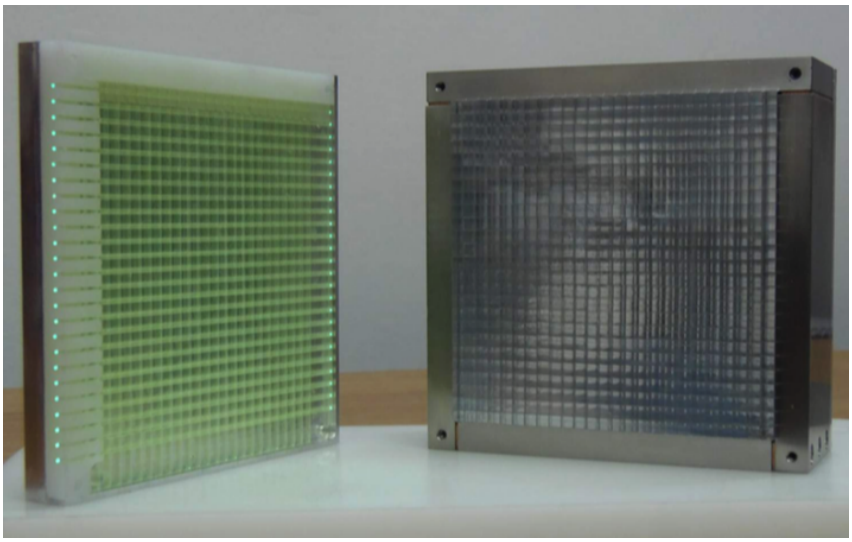

Figure 4.18: On the left, the net of WLS fibers mounted on a UVT acrylic and on the right the crystals array inside the Aluminium housing.

sensor used is a Multi-pixel photon counter (MPPC) Hamamatsu S10931-025P[42]. This device is a new type of photon counter using multiple Avalanche Photo-Diode (APD) pixels. The MPPC operates in a Geiger mode on a low voltage and features a high multiplication ratio (gain).

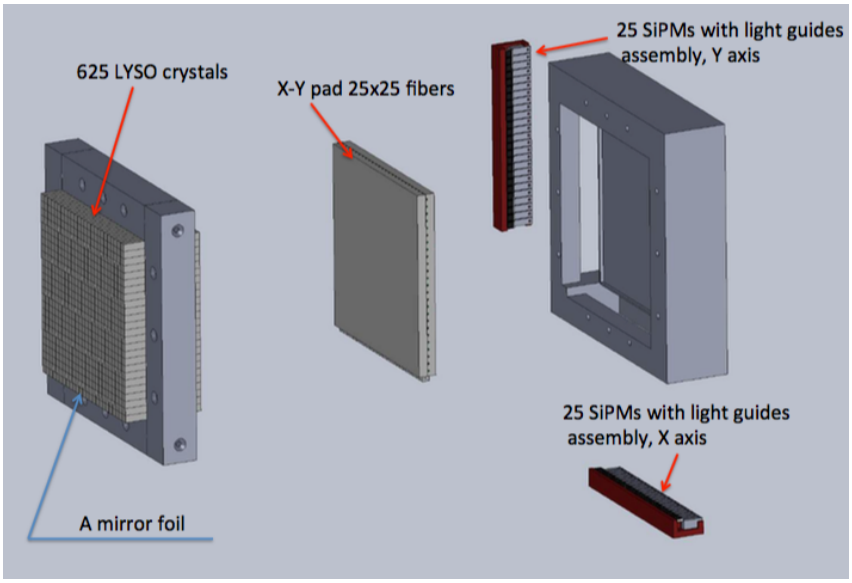

Figure 4.19: Scheme of LYSO detector.

4.8.1. Electronic Readout

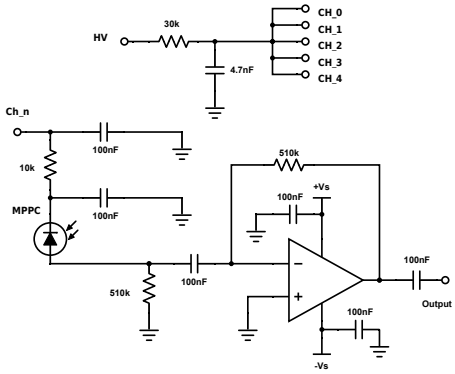

(a) Amplifier and bias voltage circuit for MPPC

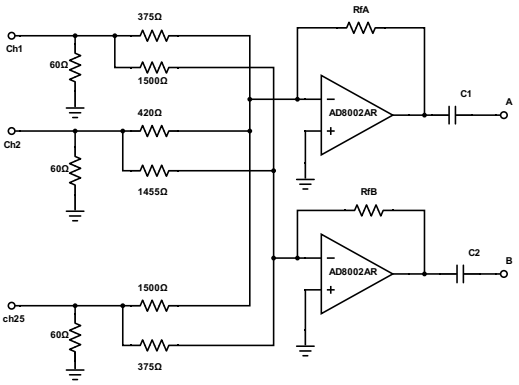

(b) Weighted signal circuit

Figure 4.20: The figure **(a)** shows two circuits, one is the amplifier circuit (bottom) for each Multi-Pixel Photon Counter and on top the polarization circuit for 5 MPPC. The circuit on **(b)** provides the two weighted signals from N channels which are implemented on one side only to reduce the amount of channels.

The readout consists of 50 Multi-pixel Photon Counter (MPPC) [42], 25 per axis (X and Y). MPPC's with similar gain were selected in group of 5 to share the same bias voltage. The top circuit in Figure 4.20a shows the polarization circuit for each group of 5 MPPC. The polarization voltage is supplied by a CAEN module SY2527 and the voltage is controlled through telnet protocol.

```
 -  Main  Utility  Setup  Groups  View                                    User
Group 00
Channel Name  V0Set     I0Set     VMon      IMon      Pw  Status          Ch#

CHANNEL00     71.60 V   100.0 uA  71.90 V   12.5 uA   On                04.0000
CHANNEL01     72.50 V   100.0 uA  73.55 V    8.3 uA   On                04.0001
CHANNEL02     71.40 V   100.0 uA  71.40 V    1.2 uA   On                04.0002
CHANNEL03     71.50 V   100.0 uA  70.95 V    1.4 uA   On                04.0003
CHANNEL04     71.50 V   100.0 uA  72.60 V    1.5 uA   On                04.0004
na             0.00 V     1.0 uA   0.00 V    0.0 uA   Off               04.0005
CHANNEL06     73.80 V   100.0 uA  73.60 V    0.2 uA   On                04.0006
CHANNEL07     72.30 V   100.0 uA  72.40 V    0.9 uA   On                04.0007
CHANNEL08     71.70 V   100.0 uA  72.65 V    3.4 uA   On                04.0008
CHANNEL09     71.80 V   100.0 uA  72.80 V    1.5 uA   On                04.0009
CHANNEL10     73.30 V   100.0 uA  73.50 V    1.1 uA   On                04.0010
na             0.00 V     1.0 uA   0.10 V    0.0 uA   Off               04.0011

Channels Display/Edit Screen                  LocEn V0 I0     N ♦| CAEN SY2527
```

Figure 4.21: Bias voltage control for MPPC through telnet protocol.

The bottom scheme corresponds to the pre-amplification circuit for each single channel (MPPC). Only the polarization voltage is shared and 25 independent signals are provided.

The high transversal segmentation ($4 \times 4\,\mathrm{mm}^2$) from this device could help to identify

the particle position and its energy very precisely. However, the disadvantage is that more channels need to be connected to the DAQ system.

The reduced amount of ADC channels in the NA64's DAQ system leads us to reduce the numbers of channels on our device. Since the electron beam is deviated only horizontally, the SR is homogeneously distributed across the x-axis (horizontally). The vertical spread of SR is just a few mm ($\Delta\phi_{SR} \sim 1/\gamma$). Therefore, the readout from the crystal along the y-axis can be reduced. On the other hand, to identify other events with low SR emission like pions or delta electrons, it is much better to keep the advantage of the 25 channels horizontally. For the vertical side, a charge division readout system is used to reduce the amount of analog output from 25 to 2 signals.

The charge division readout system operates as a multi-channel analog signal converter which converts signals from the multi-channel output to just two per analog outputs with same amplitude correlation as common charge division position readout. The extra circuit added with a charge division style is shown in Figure 4.20b. This provides two weighted signals A and B, each one depending on the Gain G and the resistance R_n where n is the n-th channel. The relations for proper resistance and N channels are provided in equation 4.38.

$$R_n A = \frac{R_f A}{(n-1)\frac{G-1}{N-1} + 1} \qquad R_n B = \frac{R_f B}{(N-n)\frac{G-1}{N-1} + 1} \tag{4.38}$$

The average of A and B provides the total amplitude recorded on the 25 channels while equation 4.39 shows the position of the event ranging from -1 to 1. Afterwards, this position value can be translated into physical units by measuring the distance between two crystals peaks.

$$\bar{Y} = \frac{A-B}{A+B} \tag{4.39}$$

4.8.2. Calibration

The LYSO detector was placed in front of the ECAL for calibration purpose. The main target (ECAL) was located on a movable table, therefore the LYSO detector could be moved respect to the beam.

Since it was the first time when the detector was connected to the DAQ[43], a proper gain equalization was performed. This mean that the polarization voltage from each MPPC group must be adjusted to provide similar signal amplitude. For the calibration process, the beam was changed from electrons to pions, which can leave a signal of a minimum ionizing particle at the interaction with the crystals.

The method for the calibration is the following:

- The particles (pion) should interact with only one crystal per channel.
- The signal should correspond to an energy loss by a minimum ionization particle.
- The bias voltage on each MPPC group is adjusted until the Landau peak for every channel is roughly on the same ADC channel.

The Figure 4.22 shows the position of the LYSO detector refer to the pion beam. On the first two configurations each pion triggers only one row of crystals providing the same signal for each channel. Each analog signal is sent to a shaper card, afterwards to the ADC with 12 bit resolution for input signals from 0-1 V.

A program for monitor events online was used to look at the event's distribution. The monitor program named COOOL[44] provides histograms of the integrated signal and other features. At the beginning of the calibration all the MPPC were set with the typical operation voltage, 70 V. The range of operation voltage for this MPPC type is 70 ± 10 V.

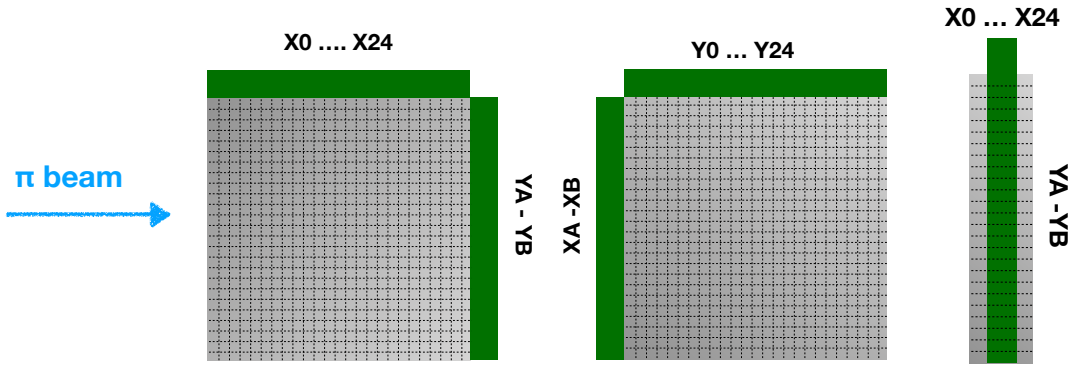

(a) x-side **(b)** y-side **(c)** z-side

Figure 4.22: Detector position for calibration. Pion beam is always from the left to the right on the three configurations

The peak value for the energy loss on each channels was around 20-50 ADCcounts (or arbitrary units au from now on). The aim was to set a higher peak value on each MPPC, since the full range of the ADC was around 4000 au. The polarization voltage was changed on the CAEN module during each spill, refreshing the histograms to the get all the peak values around 65 au. After finishing the process, around 10 spills were recorded for offline calibrations.

The process was repeated for the second group of 25 MPPC from the Y side, but this time the detector was in position **(b)** and the readout electronics were exchanged to get all the 25 signals. The polarization voltage was adjusted until reaching a peak value around channel 50 au, a few au less compared to the X side. The reason for a lower gain was to prevent saturation from the two outputs by using the weighted signal board.

The aim of the third configuration **(c)** was to obtain the position resolution, since only one crystal is triggered by the pass of one pion. Since the pion beam was roughly 5 cm of diameter, two positions respect to beam were registered, the pion beam hitting on the left half and another run with the right half.

Offline calibration

The Figure 4.24 shows a typical waveform from the ADC with 32 samples. The first 8 samples are used for pedestal calculations, but since half of the samples comes from one

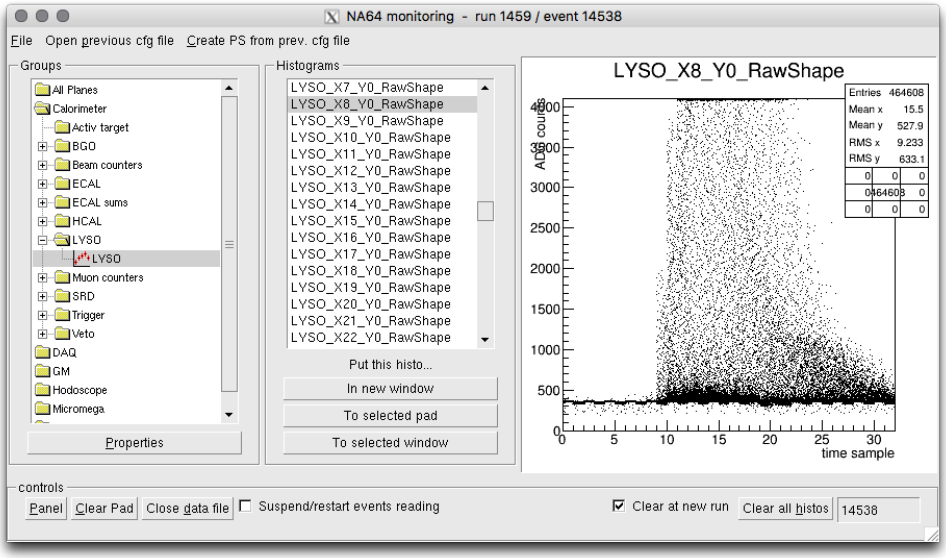

Figure 4.23: Monitoring application COOOL showing a waveform from channel X8. 32 time samples are obtained from the two ADC and 4096 channels for amplitude counts. Pedestal is around 400 ADC counts

ADC and the other half from another one, two pedestals must be obtained.

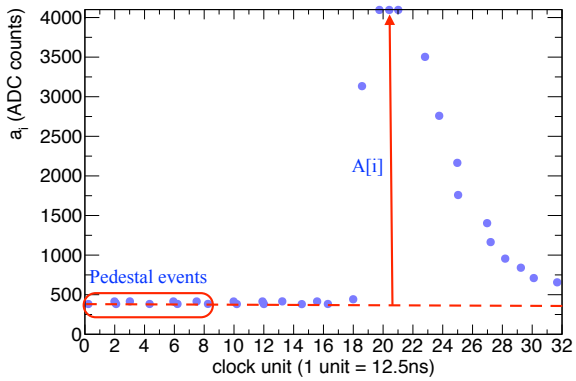

Figure 4.24: 32 time samples of a raw pulse obtained from the ADC.

The waveform is represented as:

$$\mathrm{A}_i = \{a_0, a_1, \ldots, a_{30}, a_{31}\} \tag{4.40}$$

and the two pedestals are calculated from:

$$\mathrm{ped0} = \frac{1}{4} \sum_{i=0,2,4,6} a_i \qquad \mathrm{ped1} = \frac{1}{4} \sum_{i=1,3,5,7} a_i \tag{4.41}$$

Afterwards, the corresponding pedestal was subtracted for each corresponding ADC amplitude:

$$\overline{\mathrm{A}}_i = \{a_0 - \mathrm{ped0}, a_1 - \mathrm{ped1}, \ldots, a_{30} - \mathrm{ped0}, a_{31} - \mathrm{ped1}\} \tag{4.42}$$

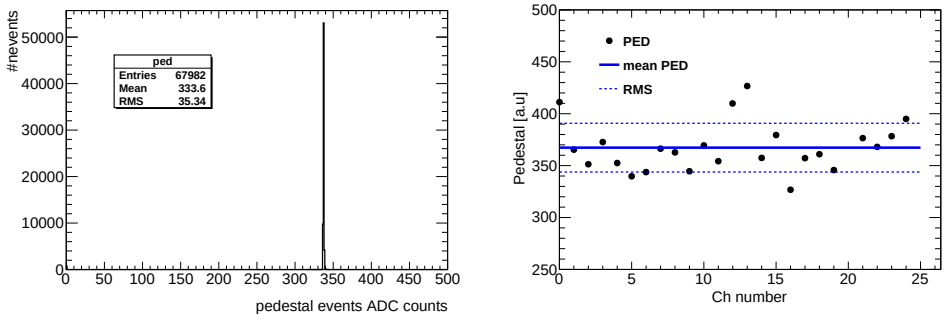

(a) Pedestal example from COOOL. **(b)** Pedestal calculation summary.

Figure 4.25: The figure (a) shows a typical pedestal obtained from the monitoring program. The figure (b) shows an offline calculation of pedestal

A typical pedestal from one channel on the monitoring tool COOOL is shown in Figure 4.25a. A summary of pedestal calculated offline is shown in Figure 4.25b, where the pedestal value is obtained from the histogram of the mean value of **ped0** and **ped1**. A Gaussian fit is applied and the mean and sigma value from the fit are shown on the summary per each channel. The RMS is approximately 1 au for each pedestal, except the channel 20 not shown on the summary. The channel 20 presents a problem of connection during the calibration and histogram of the waveform is shown in Figure 4.26.

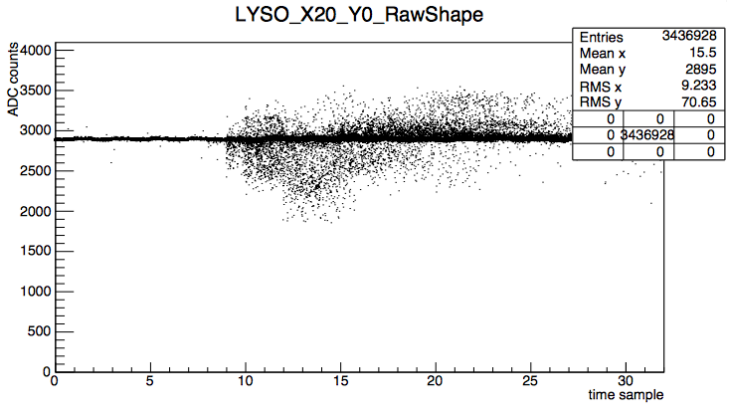

Figure 4.26: Bad channel

The ADC records a pulse when the amplitude of the signal overpasses the threshold level (5 a). Until it reaches the maximum amplitude, the waveform correspond to the integrated signal from the front-end, therefore the maximum represent the charge of the input. Since the energy loss is proportional to ionization on the crystal and the light collected by the MPPC is proportional to the electric charge provided by the avalanche, one can compare the maximum amplitude with the energy loss by one particle.

For the configuration **(a)** and **(b)** the pions cross only 0.4 cm with a density of 7.1 g/cm^2 by losing approximately 2 MeV/g cm^2, therefore a 5.68 MeV is deposited on

each crystal. This value is compared with the most probable value (MPV) obtained from a Landau fit of the amplitude histogram as Figure 4.27 shows. The procedure is apply to each channel and for the two configurations.

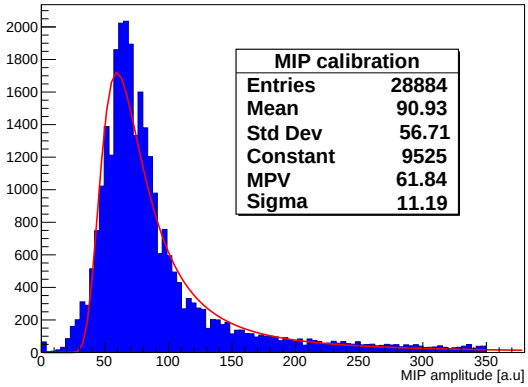

Figure 4.27: Histogram from amplitude when a MIP passes through the crystal across

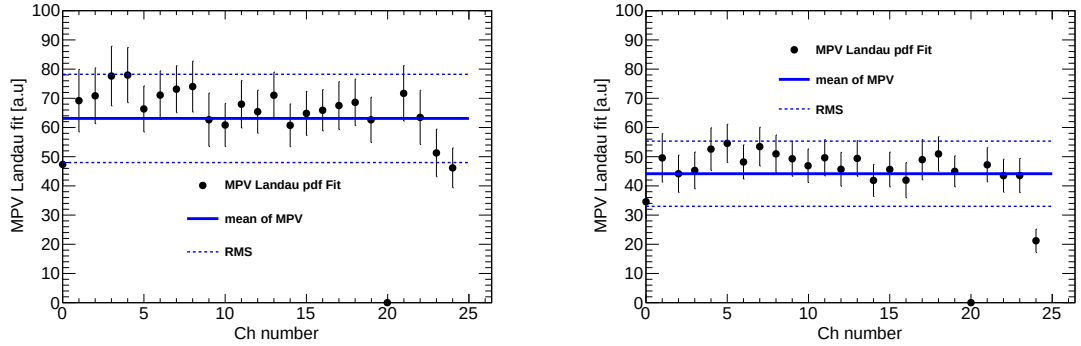

(a) Mip position on x-side

(b) Mip position y-side

Figure 4.28: Gain equalization. Data sets excluding channel 20 for high pedestal and shape problems.

The Figure 4.28 shows a summary for both configuration with all the peak values. The problem on channel 20 mentioned before is present in both summaries, this means that the problem was not caused by the detector; but rather by the DAQ system itself.

By using the peak values, it is possible to provide energy calibration coefficients and estimate the total energy such as:

$$E_{\text{tot}} = \sum_{i=0}^{24} a_i c_0^i \tag{4.43}$$

where c_0 corresponds to the calibration coefficients calculated as $c_0^i = 5.68/\text{MPV}_i$ and a_i corresponds to the maximum amplitude per channel on each event.

For the configuration **(c)**, when the detector is perpendicular to the beam (Figure4.22c), the expected mean energy deposited by a minimum ionizing particle is $E_{\text{mip}} \sim$

64 MeV. It means that for every event, the total light collected should be E_{mip}.

The Figure 4.29 shows energy distribution for a MIP particle crossing the crystals on the configuration perpendicular to the beam. A Landau fit is applied and a 66 MeV is obtained as mean with a $\sigma = 4.5$ MeV. This gives a energy resolution of $\simeq 6.9\%(4.588/66.57)$ for the x-side.

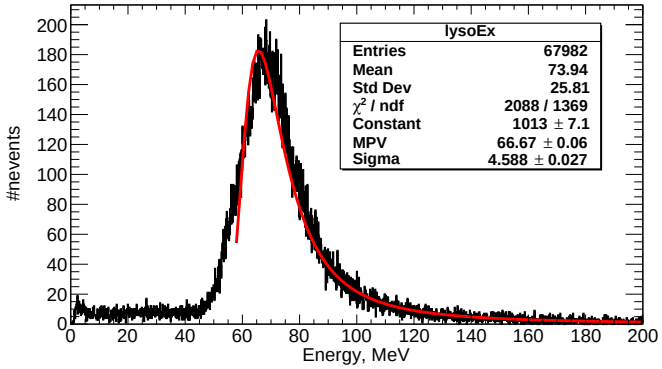

Figure 4.29: Total energy deposited on x side with the **(c)** configuration and calculated as 4.43

On the y-side, every channel was equalized to around the same MPV value (50 ADC counts). Therefore, both weighted signal should show the same distribution with slightly the same MPV values. By applying a Landau fit over the sum of YA plus YB amplitudes, hence the total energy, it is possible to estimate the resolution for the y-side. The Figure 4.30 shows the histogram of both weighted signal with a MPV of 1207 (ADC counts) and a $\sigma = 89.5$ which results in a $\simeq 7.4\%$ energy resolution at 64 MeV.

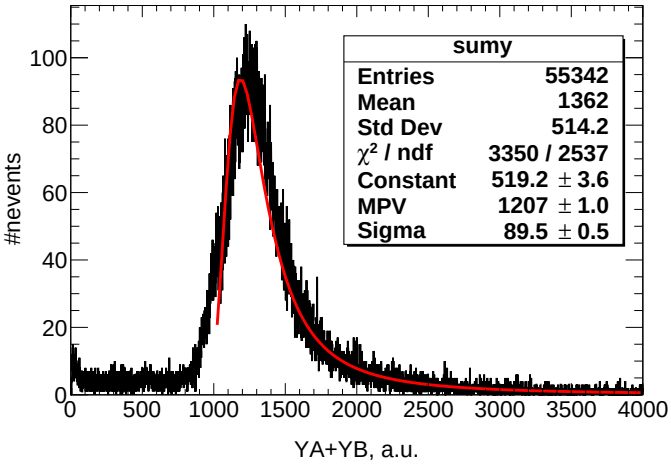

Figure 4.30: Total energy deposition on y-side (arbitrary units)

Particle position

The charge division circuit was designed to obtain the particle's position crossing the detector along y-side. The position is obtained according to equation 4.39. On the other hand, to calculate the position on the x-side, a different treatment must be done. Using a simple center of mass calculation for each x channel the position can be estimated such as:

$$\bar{x} = \frac{\sum_i x_i E_i}{\sum_i E_i} \tag{4.44}$$

where x represents the channel number and E_i the energy deposited on that channel. The values for particle position from x-side will range from 0 to 25 while for the y-

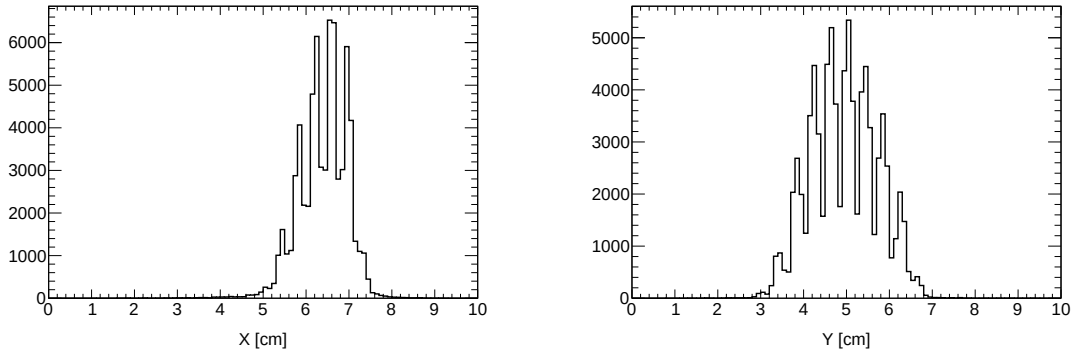

(a) X-axis position **(b)** Y-axis position

Figure 4.31: X position comparison from Run 1467 y 1468.

side it will range from -1 to 1. In order to translate these numbers into centimeters, a distance from peak to peak (in arbitrary units) is compared with the 0.4 cm. This distance corresponds to the space between crystals. The Figure 4.31 shows the position distribution of the pion beam on **(c)** configuration. The position calibration is applied and the histograms of particle position are shown in centimeters. About 6 columns of crystals (strips) are fired on the x-side, while in y-side 9 strips are fired resulting in a beam size of 2.4x3.6 cm^2.

A beam profile can be performed using x and y position. The 2D profile is shown for two beam position in Figure 4.32.

4.8.3. Response Time of LYSO

To calculate the time resolution for each device on NA64 detector, three methods were applied.

1. **Max sample**

   From the 32 time samples, the max amplitude is recorded and the time sample when this happened is set as the time t_0. This method is very sensitive to saturation of the ADC range. The scintillator counters reach easily the maximum ADC counts, and then timing will be independent of the max amplitude reached by the detector.

   The Figure 4.34a shows the t_0 distribution calculated with this method. The majority of the events from the counter $S1$ saturate the ADC, therefore, two sharp peaks are present at 237 ns($12.5 \cdot 19$) and 250 ns($12.5 \cdot 20$). A separation of exactly 12.5 ns shows that the counter is saturated at the same time sample, either in one ADC or in the next one.

2. **Center of Mass**

   This method estimates the center of mass of each pulse, and the result represents t_0. The center of mass for one pulse is calculated as :

   $$t_0 = \frac{\sum_{i=8}^{31} a_i \cdot i}{\sum a_i} \tag{4.45}$$

   which considers the amplitudes a_i after the time samples for pedestal estimation. Only the time samples after 8 are considered. Figure 4.34b shows the $t0$ distribution for $S1$

3. **Rising Edge**

   The last method calculates the intersection of the rising edge with the time axis to get the origin time (t_0). Again using the maximum of amplitude, the algorithm

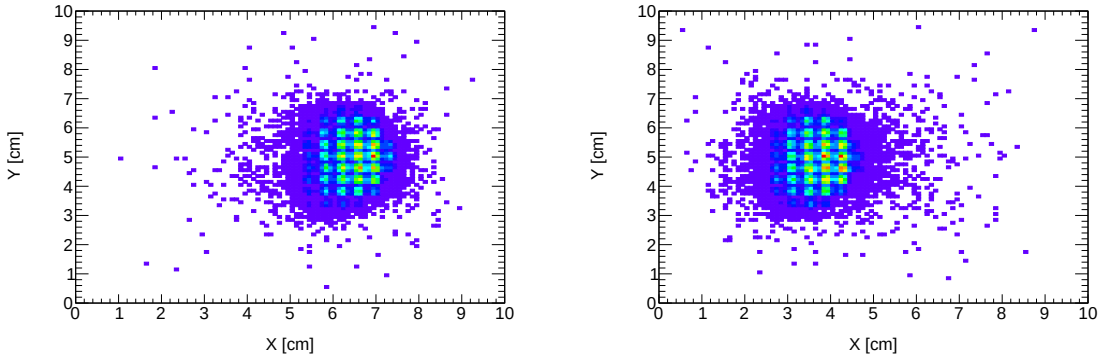

(a) Run 1467 **(b)** Run 1468

Figure 4.32: Beam profile for two different pion runs, with different detector's position.

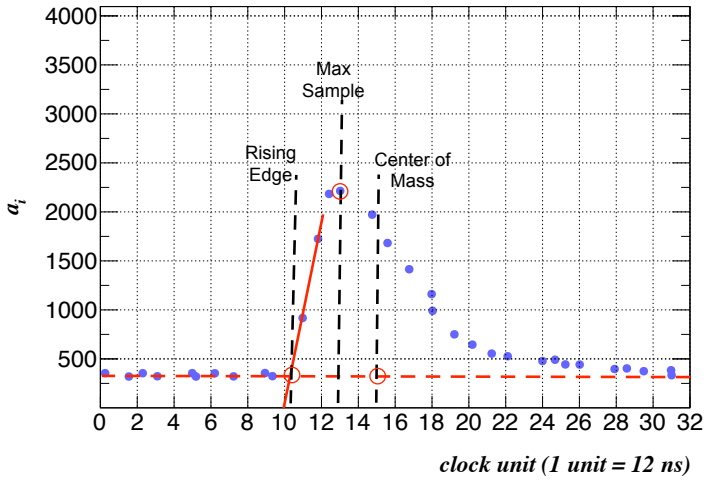

Figure 4.33: Timing methods on wave sample. The red line is calculated from the time sample above half of the maximum and the crossing point with the pedestal (0 amplitude)4.45. Each red open circle shows the time estimation according to its method.

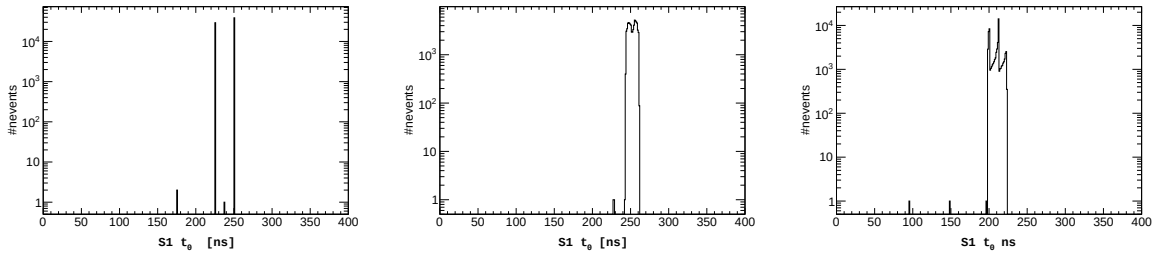

(a) Max Sample **(b)** Center of Mass **(c)** Rising Edge

Figure 4.34: Timing calculated for S1 with three different methods; Max sample, Center of Mass and Rising Edge.

looks for the time sample with half of the maximum or above and returns the index of the time sample. Afterwards, from the time sample with half of the maximum (a_j) and the previous one a_{j-1} it is possible to obtain the intersection of this linear with the axis time.

$$t_0 = t_j - \frac{a_j}{a_j - a_{j-1}} \tag{4.46}$$

This method presents the advantage of being non-sensitive to saturation, because of the use of two time samples before the saturation occurs. In the worst case when there are no time samples between the base line and the maximum, the origin time will be the time sample before the saturation.

4.8.4. Time Resolution

Using the Rising Edge method to estimate the origin time for each pulse, the time resolution for LYSO detector in the detector system can be performed respect to $S1$ the main counter. Since each crystal has its independent readout, the resolution can be estimated channel by channel referred to $S1$. For this measurement, the chosen configuration is where the detector is hit by pion beam from the side, therefore each channel on the x side will be fired at the same time. Afterwards the origin time for each crystal is compared with the counter $S1$,($\mathrm{T} = \mathrm{T}^{\mathrm{x}}_{\mathrm{LYSO}} - \mathrm{T}_{\mathrm{S1}}$)and the time difference for one channel is shown in Figure 4.35a.

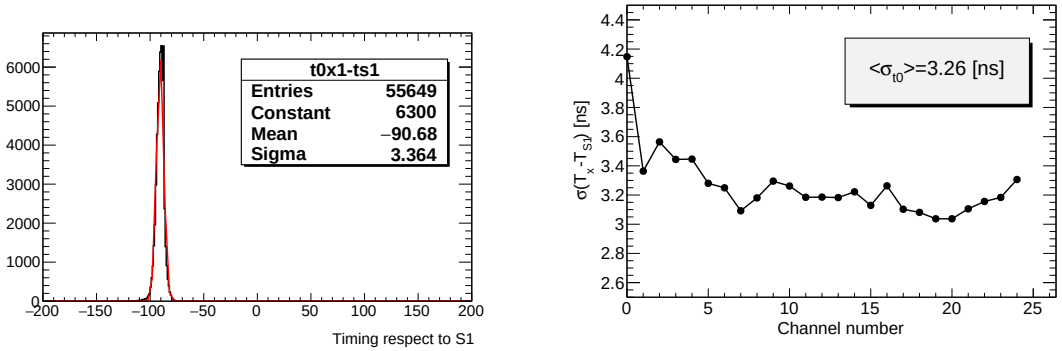

(a) Time distribution of Ch.1 respect to S1.

(b) $\sigma_T(T_{LYSO} - T_{S1})$ estimated from Gaussian fit for each channel.

Figure 4.35

Although the origin time distribution for $S1$ does not reproduce a Gaussian shape in Figure 4.34c, the time difference $\mathrm{T} = \mathrm{T}_{\mathrm{LYSO}} - \mathrm{T}_{\mathrm{S1}}$ does it. Therefore, a Gaussian fit is applied and where $\sigma_T(T_{LYSO} - T_{S1})$ shows a 3.3 ns of time resolution for this channel. The negative mean time for this differences does not have any physical meaning. Each ADC module sets a reference time respect to the Time Control System, and it is assigned according to the position of the detectors respect to the beam line, delay respect to signal cable length, etc.

For each single channel in x-side, the procedure is applied and the Figure 4.35b shows the σ parameter for each Gaussian fit. Hence, σ represents $\sigma_{t0} = \sqrt{\sigma_x^2 + \sigma_{S1}^2}$ where x is the channel number.

The readout from x-side provides on average a time resolution of $\hat{\sigma}_t^x = 3.26 \pm 0.22$ ns. On the other hand, the procedure can be applied to the two weighted signals YA and YB. Both are compared to the main counter $S1$ and the distribution of these events is shown in Figure 4.36. In both cases, the time resolution is about $\sigma \sim 2.3$ ns. This means that the time resolution for the y-side $\sigma_t^y = \sqrt{\sigma_{YA}^2 + \sigma_{YB}^2} \sim 3.1$ ns.

4.8.5. Intrinsic time resolution

With the run 1459, where all the channels are triggered, it is possible to measure the intrinsic time resolution by comparing the origin time from two neighbor channels.

The origin time is calculated with Rising edge method for each channel, and afterwards is compared with the previous channels. This time difference would be $T = T_x - T_{x-1}$, where x represents the channel number. Hence, we would have 24 comparisons. The Figure 4.37a shows a convolution of two Gaussian distributions, one narrow and another one wide. The narrow one (in blue) represents the majority of the events and it has a $\sigma \sim 1.3\,\text{ns}$. The rest of the events are represented by a wider Gaussian with a $\sigma \sim 3\,\text{ns}$ which can be explained by some light collection from the net of fibers provided by other crystals.

The Figure 4.37b shows the σ parameter of the narrow Gaussian (blue from the left picture) from the time difference between two contiguous channels.

Defining, $\sigma_T = \sqrt{\sigma_x^2 + \sigma_{x-1}^2}$ and we can suppose that both crystals has the same resolution, then $\sigma_x \approx \sigma_{x-1} \equiv \sigma_{int}$, therefore, the intrinsic time resolution would be $\sigma_{int} = \sigma_T/\sqrt{2}$. Using the average resolution obtained, the intrinsic resolution is $\sigma_{int} = \frac{\bar{\sigma}_{t0}}{\sqrt{2}} = \frac{1.06}{\sqrt{2}} = 0.75\,\text{ns}$.

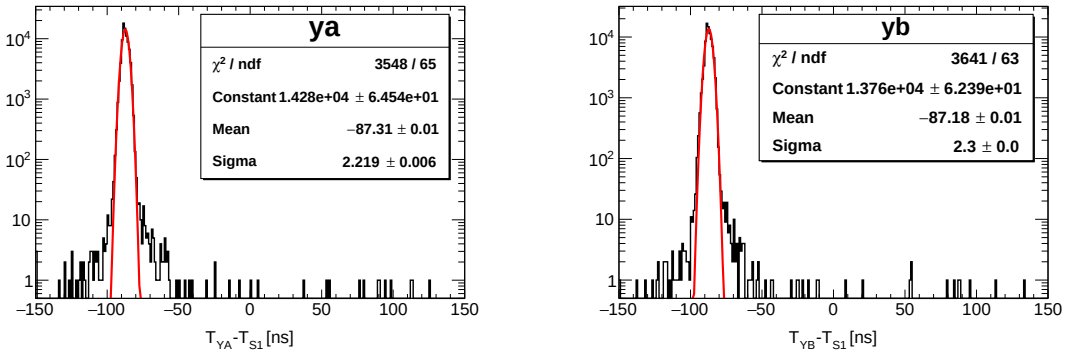

(a) $T_{YA} - T_{S1}$ **(b)** $T_{YB} - T_{S1}$

Figure 4.36: Time distribution of weighted signals YA and YB respect to the main counter.

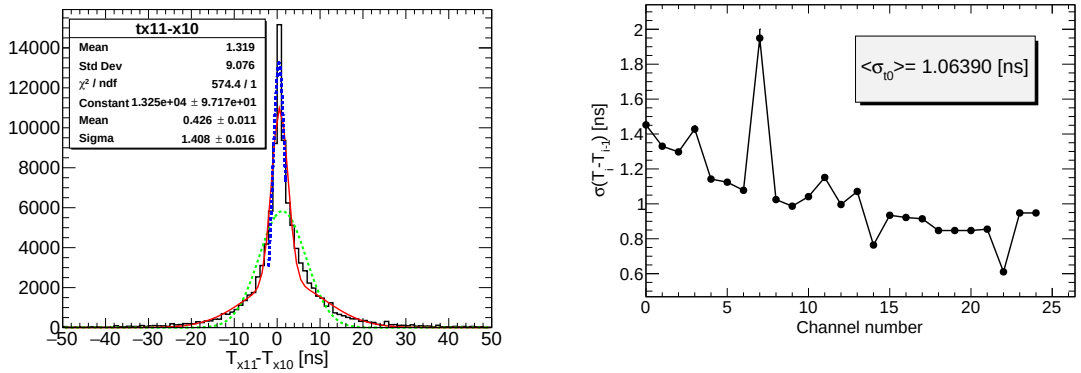

(a) Time distribution of $T_{x=11} - T_{x=10}$.

(b) Time resolution for each ch number compared to the previous one.

Figure 4.37: Intrinsic time resolution measurements. The left plot shows the time distribution of the difference between two contiguous channels. Two Gaussian fit are adjusted, a narrow and a wider one. The parameters in the plot represent the sigma for the convolution of the two Gaussian functions (in red). The plot on the right, is the collection of each σ_t for each comparison of two adjacent channels.

4.9. Hadron suppression with LYSO

During the first Run of the NA64 experiment, three options for synchrotron radiation were tested in the *invisible decay setup* Figure 4.6. For each SR detector, (**BGO, LYSO** and **Pb+Sc**) a set of data were taken with low and high intensity beam. Where low intensity means $\sim 10^5\,e^-/s$ while high intensity is close to the maximum intensity of the SPS beam, about $10^6\,e^-/s$ register on the main counter **S1**.

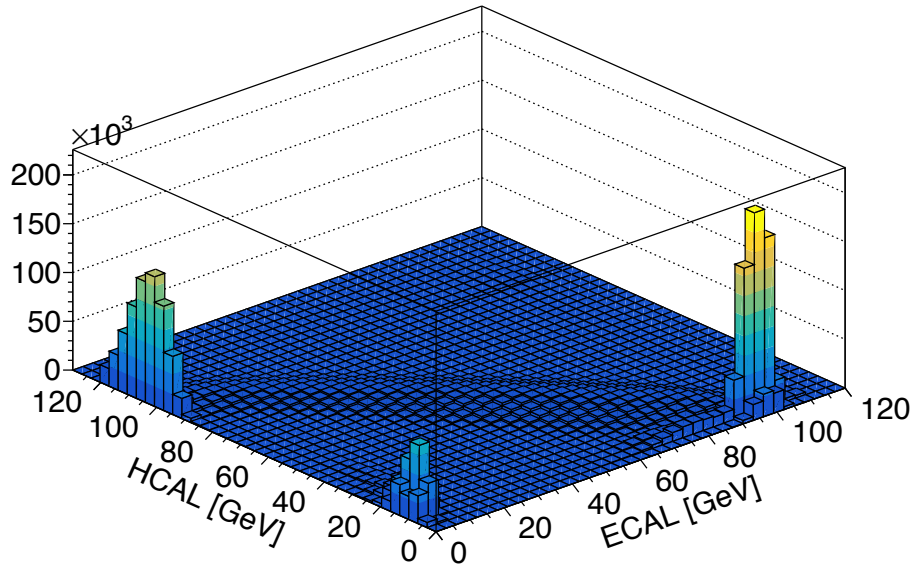

Figure 4.38: Distribution of events on HCAL and ECAL, for runs of low intensity. 100 GeV electron beam.

To identify the signature of SR from an electron or hadron, a selection cuts from the calorimeters (electronic and hadronic) were maid. The Figure 4.38 shows the distribution of events of the data set for low intensity, where LYSO was used as SRD.

The 2D energy histogram, shows the 100 ± 10 GeV electrons with a low deposition on HCAL ($HCAL < 6$) and the presence of hadrons on the beam with a energy deposition on hadronic calorimeter of 105 ± 15 GeV while less than a 1.5 GeV is deposited on ECAL. The third bump observed is the presence of muons in both calorimeters. Having these two clear selections, is possible to observe the energy spectrum for both particles on LYSO. Moreover, the selection of events require that the signals from the calorimeters, LYSO and main counter(S1) must be in-time ($0 < t_0 < 400$ ns). Therefore, the total selection to identify the signature of electrons and hadrons are the followings:

Electrons

- $90 \leq$ ECAL $\leq$ 110GeV
- HCAL $\leq$ 6GeV

Hadrons

- ECAL $\leq$ 1.5GeV
- $90 \leq$ HCAL $\leq$ 120GeV

Applying these criteria selection, we find a total of about 650.000 events which correspond to electrons identified and 350.000 events for hadrons. The energy deposition is calculated from the calibrated X-axis with a MIP particles as previously discuss in section 4.44. The energy spectrum observed on the LYSO detector is shown in figure 4.39. Most of the energy deposited from SR photons are in 11 MeV of energy for electrons (blue line), while the SR peak for Hadrons is accumulated in a couple of MeV.

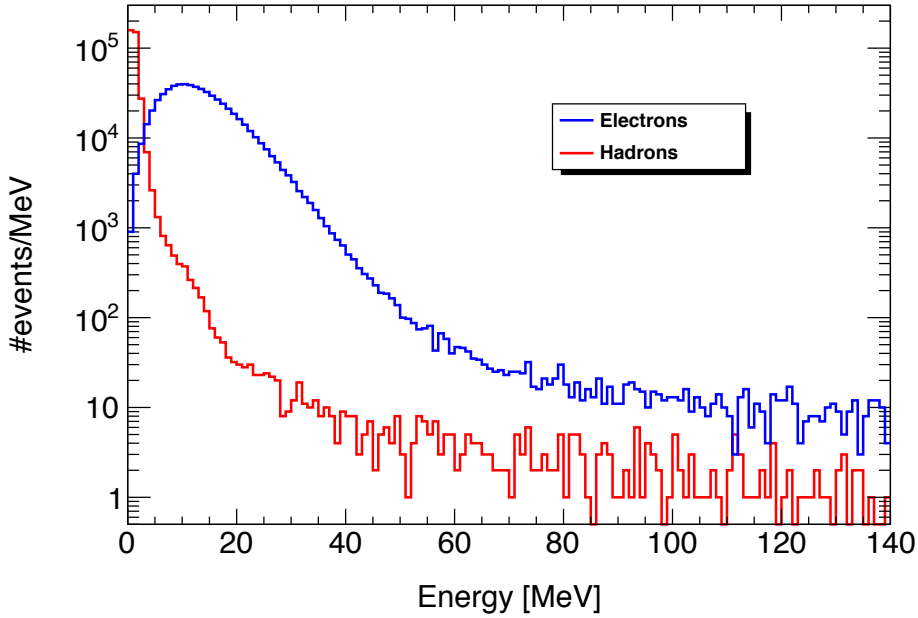

Figure 4.39: Synchrotron radiation on LYSO, for low intensity runs.

4.9.1. Energy deposition as tagging parameter

The main goal of this device is to reject events which correspond to hadrons by using the energy deposited (E_{th}) on LYSO as a rejection parameter.

The total power irradiated by hadrons is considerably lower than electrons, and the peak of the synchrotron distribution is just at a few keV. Therefore one can select events with higher energy deposition and the number of hadrons will be decreased. The figure 4.40a shows the two spectrum, for electrons and hadrons and the position where the electron energy deposition becomes important is higher than 3 MeV. A selection cut of events with different threshold of energy was performed using the electron efficiency (η) and the suppression factor (δ), defined as:

$$\eta = \frac{n_e}{N_e}, \quad \delta = \frac{n_h}{N_h} \tag{4.47}$$

where n_e is the number of electrons which survive the selection cut, and N_e the total amount of electron identified with the calorimeters cuts. The hadron follow the same logic with n_h as the number of hadrons which pass the test.

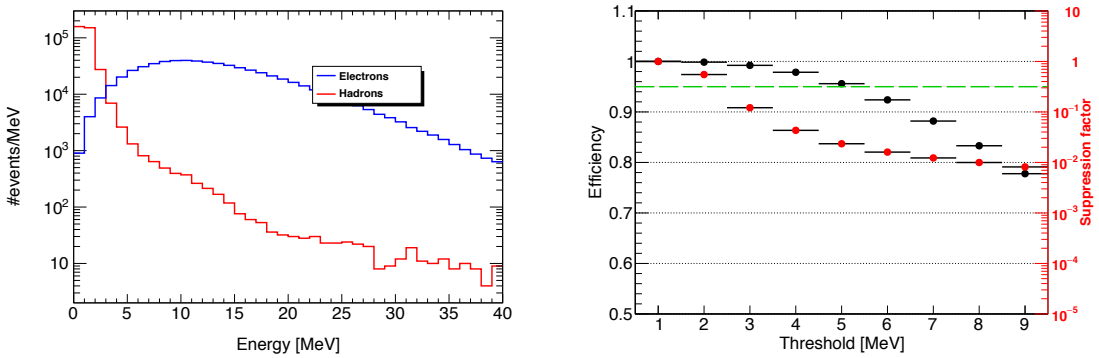

(a) Synchrotron radiation spectrum of electrons and hadrons on LYSO

(b) Hadron suppression and electron efficiency factors of Energy threshold

Figure 4.40: Total Energy threshold analysis

The electron efficiency and suppression factor are shown in Figure 4.40b by using the total energy as rejection parameter. The green line represents the 95% of electron efficiency that we don't want to cross. At the same time, we would expect to have a suppression factor of the order 10^{-4} or lower, however the rejection factor obtained is almost two orders.

A similar analysis is performed with the number of strips triggered as rejection parameter.

4.9.2. Strips as tagging parameter

The number of strips triggered on the x-axis will depend on how much energy is deposited on the detector. Moreover, the events coming from decay in-flight, e.g. electrons coming from ionization and low energy electrons can provide an specific signal; few strips triggered with high energy deposition. For this purpose the analysis of hadron rejection and other events than 100 GeV electrons can be rejected using the number of strips as rejection parameter.

The Figure 4.41a shows the number of strips triggered for electrons (blue) and hadrons (red). The electron distribution became important for more than 10 strips. Comparing with the energy analysis aforementioned, it is also important that the number of hadrons events when the distribution of electrons is higher than hadrons (more than 10 strips) must be low. However, there are still remaining hadron events

The suppression factor using the strip parameter is shown in Figure 4.41b, where for an efficiency higher than 95% (green line) the rejection factor is 2×10^{-2}.

For both analysis, the rejection parameter (energy and strips) is higher than 10^{-2}. This is related to the long tail of the SR distribution of hadrons.

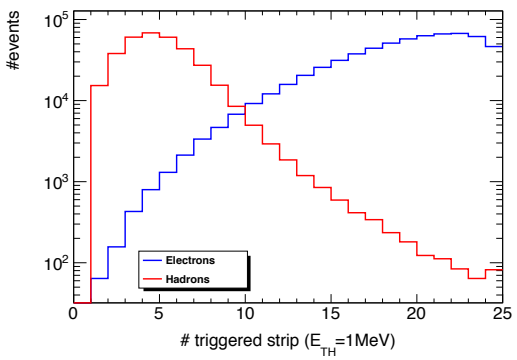

(a) Hadrons and electrons events for number of active strips with energy higher than 1 MeV on each strip.

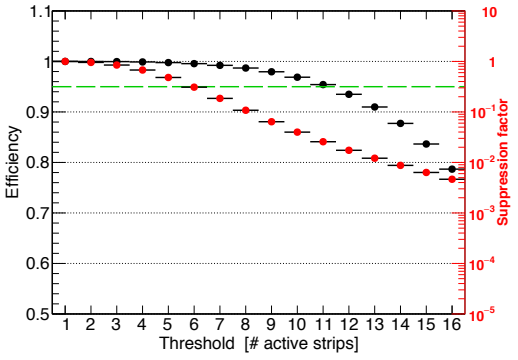

(b) Electron efficiency (black) and suppression factor (red) with number of active strips as selection parameter.

Figure 4.41: Number of strips triggered with energy above 1 MeV

4.9.3. Timing as an extra hadron-electron identification parameter

The presence of hadrons events with energy above the SR peak for electrons or multiple hadron events with more than 10 strips triggered, it prevents to achieve a lower hadron suppression factor less than two order of magnitude, hence a new parameter must be used.

Another feature from this detector is the small time decay constant ($\tau = 40\,\text{ns}$) compared to BGO, providing a good time resolution.

If we analyze the time distribution of events generated by SR from electrons and hadrons, they must be allocated in different time. By comparing the time distribution of the $T_{ECAL} - T_{LYSO}$ it can be possible to identify the two type of particles.

The Figure 4.42a shows the distribution of these events, taking in consideration the time signal from the X-side, where $T^{\text{X}}_{\text{LYSO}} = \sum_{i=0}^{24} t_i/25$, $T_{\text{ECAL}} = \sum_{i=0}^{35} t_i/36$ and t_i is the time stamp calculated using the rising edge method. For the Y-side, the time is the average of the two weighted signal (A and B).

The time distribution of ECAL refer to X and Y are shown in Figure 4.42. However, a more interesting picture is the 2D distribution of these events shown in Figure 4.43a where the separation of the events is clear. The Figure 4.43b exposes where these events are mostly localized and suggest a new rejection parameter.

Let's call $\hat{T}_X$ and $\hat{T}_Y$ as new variable of time described before. If we use a linear combination of $\hat{T}_X$ and $\hat{T}_Y$ such as the new axis, they can be oriented on the electron distribution while the new $\tilde{T}_X$ can have its origin in the transition region of hadrons and electrons events.

A linear regression is performed on the electron distribution which can be used to provide a rotation angle for the axis and a new origin for $\hat{T}_Y$. Using the two parameters for the linear regression, the $\hat{T}_Y$ axis is moved to $\alpha = 64.3\,\text{ns}$ and afterwards the axis are rotated by $\theta = 22.6^o$, giving a new set of axis:

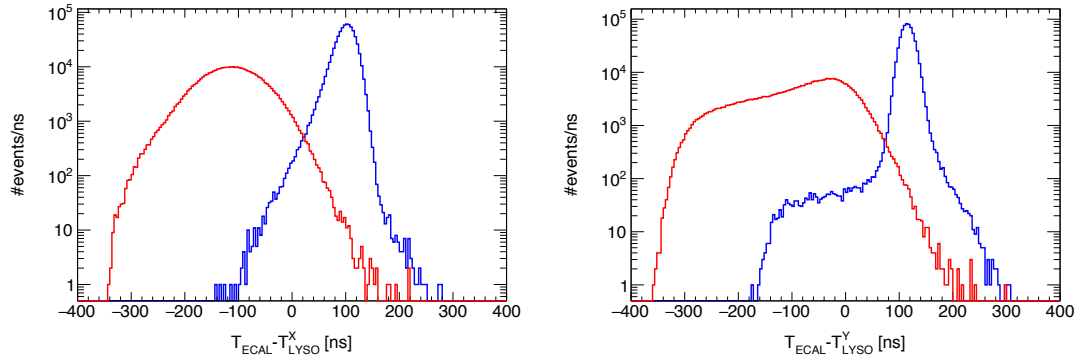

(a) Tx **(b)** Ty

Figure 4.42: Time distribution for X and Y axis with particle selection.

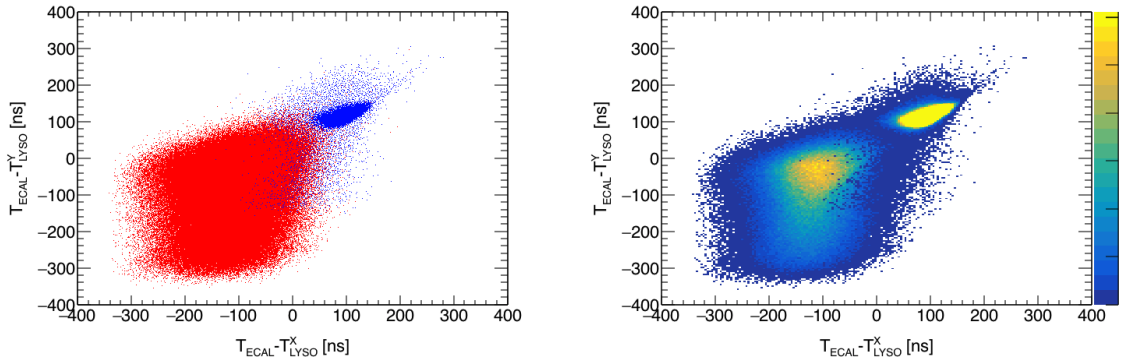

(a) Elecrons (blue) and Hadrons (red) **(b)** Particle concentration

Figure 4.43

$$\begin{pmatrix} \hat{\tau}_x \\ \hat{\tau}_y \end{pmatrix} = \begin{pmatrix} \cos\theta & \sin\theta \\ \sin\theta & -\cos\theta \end{pmatrix} \begin{pmatrix} \hat{T}_X \\ \hat{T}_Y - \alpha \end{pmatrix} \tag{4.48}$$

Since the hadrons events are localized on the negative part from τ_y, the use of $\tau_x > 0$ is enough to reject most of these events.

The Figure 4.44b shows the distribution of the estimator $\hat{\tau}_x$ with both selections criteria (hadrons and electrons).

The electron distribution became important for $\tau_x > 20\,\text{ns}$, where the level of hadrons events is around 10^{-2} and continue decreasing.

A similar analysis done for the total energy on LYSO and strips triggered is applied to τ_x. A selection of events with different τ_x is shown in Figure 4.45, where for $\tau_x > 10$ the level of suppression factor is below 10^{-2} with an efficiency close to 1. Clearly this method shown an improvement of two order of magnitude. By increasing the rejection value the rejection level can achieve 4 orders of magnitude, however a suppression factor of $6 \cdot 10^{-3}$ can be achieved without compromising the detection efficiency of electrons below 95%.

Since the rejection analysis is independent by using the energy and the time cuts as parameters, they can be applied simultaneously and the situation will improve.

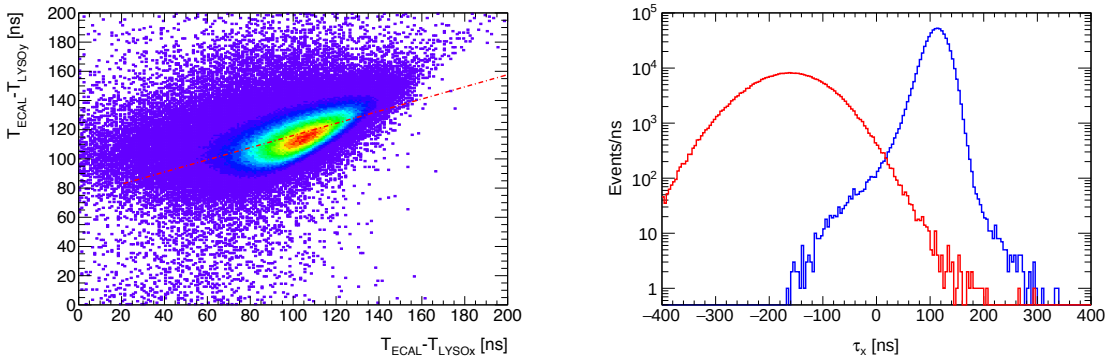

(a) Linear regression of the electron distribution events

(b) Time distribution for the new estimator $\hat{\tau}$

Figure 4.44

The new selection takes events from a fixed parameter $\tau_x > 76\,\text{ns}$ which corresponds to an efficiency of 95.2%, rejecting 4.6×10^4 hadron events. Afterwards the selection of events comes from the total energy or the amount of strips triggered. On the previous analysis with these two parameters, the maximum suppression factor was 10^{-2}, but with an efficiency below than expected.

It is possible to observe on Figure 4.46 and 4.47 the combined cuts from the parameter E, strips and τ. The combined cuts use a fixed parameter τ which removes immediately about 10^2 hadrons while the efficiency is not compromised. Applying the in-time condition with $\tau > 76\,\text{ns}$ and the total energy deposition or the amount of strips the hadron rejection could be done efficiently.

The two graphs show a hadron suppression below 10^{-4} with efficiency above 95%. However to achieve the 10^{-5} hadron suppression a higher statistics must be taken. A few tens of hadrons events remain after the synchrotron peak and hence a careful treatment must be applied with these events.

From the total of 350k hadrons events selected, the suppression factor achieved (10^{-4}) could be close to 10^{-5} while the efficiency drops below the 90%. A similar behavior is observed on the strips analysis. However, it is important to remark that for a suppression factor close to 10^{-5} or below, the amount of hadrons events must be at least of the order 10^6. Tens of hadrons events are after the synchrotron peak for electrons, therefore they could be misidentified by the ECAL or HCAL cuts. Hence a detailed treatment must be applied for these small statistics.

A total of 350k hadron events were identified, hence a suppression factor of 10^{-4} obtained from the Figure 4.46, where the threshold level of the energy is 2 MeV.

As it was explained before, a better level can be tested with a much bigger statistics than already collected.

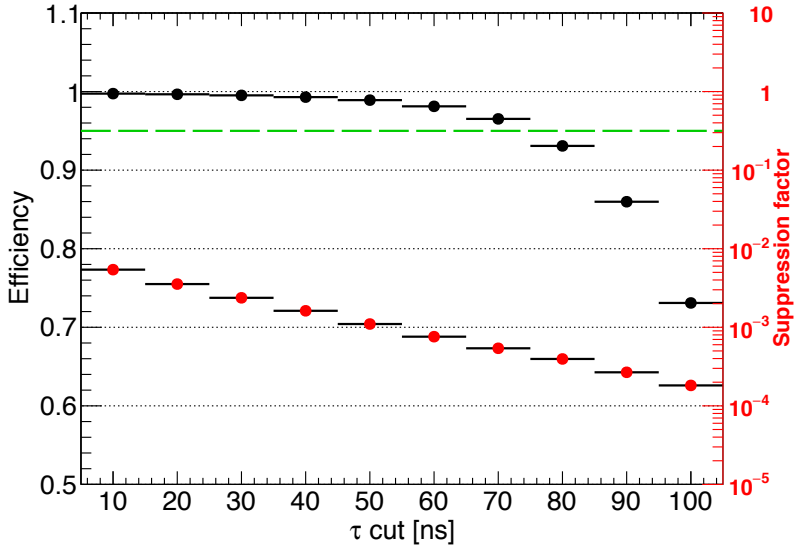

Figure 4.45: Electron efficiency and hadron suppression using the new time distribution as selection criteria. Improving the rejection by two order of magnitude.

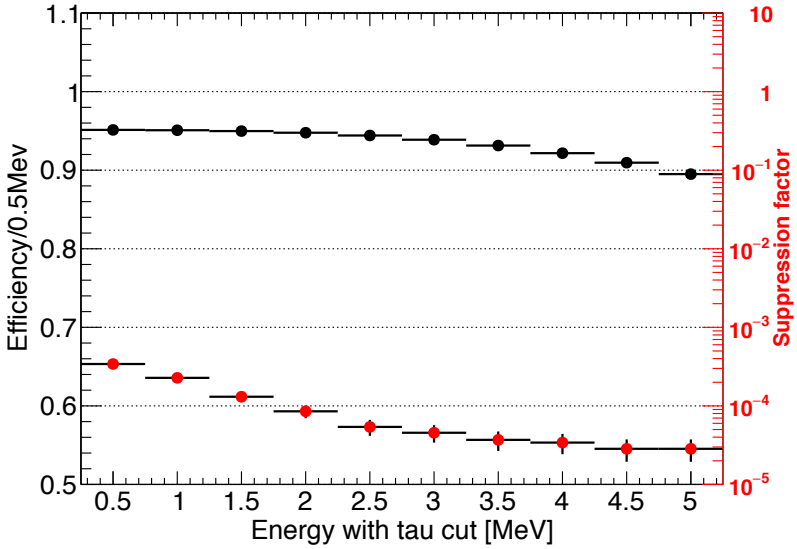

Figure 4.46: Total Energy and $\tau > 76$ ns selection.

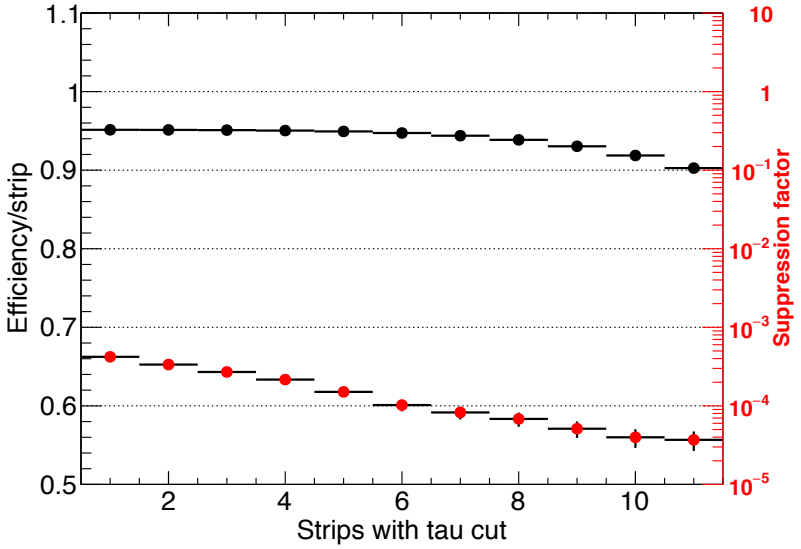

Figure 4.47: Strips and $\tau > 76$ ns selection.

4.10. Dark Photon invisible decay results

Finally we present the results from the first run of the NA64 experiment taken in 2016. The results come from 2.75×10^9 electrons on target, with a mixture of events taken with the three options of SR detector. The events were collected with the hardware trigger requiring an in-time cluster in the **ECAL** with the energy $E_{\mathrm{ECAL}} \lesssim 80\,\mathrm{GeV}$. The data sets from the different detectors were analyzed with similar selection criteria and finally summed up, taking into account the corresponding normalization factors.About 5×10^4 events were selected with the loose cut requiring in-time energy deposition in the SRD within the SR range emitted by e^-.

In order to avoid biases in the determination of selection criteria for candidates events, a blind analysis was performed. Candidate events are expected to have the missing energy in the range of $50 < E_{miss} < 100\,\mathrm{GeV}$, which was defined by taking into account the energy spectrum of A's emitted in the primary reaction $e^- Z \to e^- Z A'$ by $e^{\pm}$ from the e-m shower generated by the e^- beam in the $ECAL$ target.

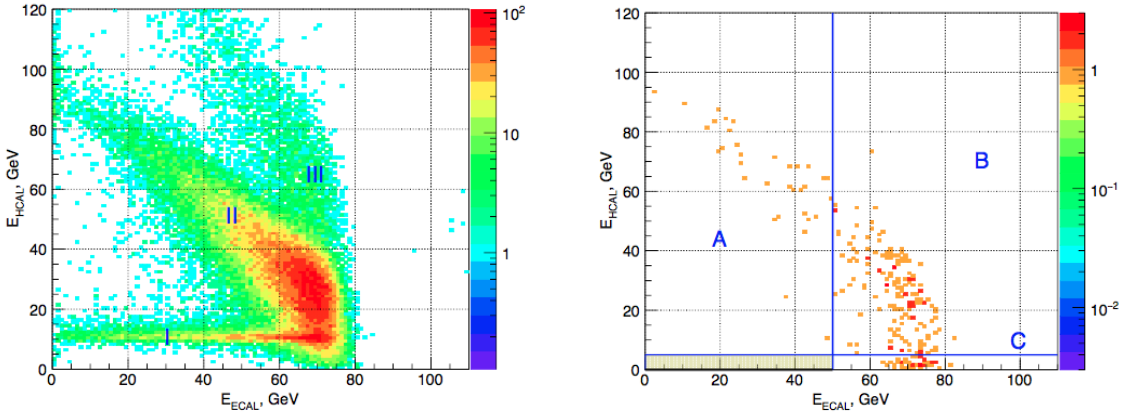

(a) Distribution of events $e^- Z \to$ anything in the ($\mathrm{E_{ECAL}}$;$\mathrm{E_{HCAL}}$) plane.

(b) Distribution of events with the dark photon selection criteria applied.

Figure 4.48: Three regions are identified in plot (a); the region I corresponds to the rare muon pair photo-production by hard bremsstrahlung photon conversion. The II region corresponds to the hadron electro-production in the target and the last region (III) corresponds to a small fraction of events due to pile-up e^- and hadrons presented on the beam. The plot (b) is divided in 4 sections, the section A and C are used to determine the background events, the section B correspond to punch through hadrons. The signal box is the shaded area and is increased in size for illustration purpose.

Events from the signal box ($E_{\mathrm{ECAL}} < 50\,\mathrm{GeV}$;$E_{\mathrm{HCAL}} < 1\,\mathrm{GeV}$) were excluded from the analysis of the data until the validity of the background estimate in this region was established.

So far, no events have been found with such signature. Results from the first run were published[25].

5. Conclusion

The thesis presented three different topics with a common thread, the understanding of modern detectors and the advantages of them. For each subject the detectors have been characterized, calibrated and tested under different conditions.

The work on the sTGC topic gave me the opportunity to be part of the full process of research and development of a new detector. We did not only characterize the detector but we did also set new process to test the characteristics. I was also involved in the construction process, where I learnt that every single detail of such detectors is important. To achieve such spatial resolution is not a trivial job.

The results obtained from the two early tests presented in the chapter 2, the x-ray and the γ-ray tests were part of a long list of trying. Finally we did not only obtain the results but we also set the new parameters for such tests and helped to the NSW collaboration to provide quality parameters. It has been a great achievement from the sTGC Chilean team work to build a detector which successfully passed all the tests.

The characterization team of the sTGC can now confirm that there is a detector which can fulfill the requirements for the new HL-LHC.

In the chapter 3, we faced a situation where the detector could not longer work properly and extra features had to be performed. The results obtained here will be shown to the GIF++ collaboration and GIF++ users. It will help to rethink their data and it may help to give them some answer to their issues. There may be interest from part of the collaboration to repeat such tests or not, but from now on, the understanding of how to work with pile-up events opens up the possibilities to addres the same problem with different detectors in various contexts.

Lastly, the participation in a young experiment from the beginning gave me the opportunity to help an international team and face all the problems of a detector system. I did not only work as a detector expert for LYSO, I also helped to build the four hadronic calorimeter modules, by gluing, assembling and testing. I was also part of the decode of the data structure from the DAQ and many other small tasks that are not described in this thesis.

For future work, the main focus in the short term will be the NA64 experiment. It is planned to be measured the η and η' decays from a charge exchange interaction using a pion beam. For this measurement a new active target has been built and it will be part of the 2018 runs for the NA64 experiment. A full characterization publication of the array of LYSO crystal will be sent in the next months.

In the long term, the main goal is to continue working on experimental search for dark

matter, as it is nowadays the main mistery to be solved in physics.

Bibliography

[1] ATLAS collaboration, *"Observation of a new particle in the search for the Standard Model Higgs boson with the ATLAS detector at the LHC"*, Physics Letters B **716** (2012) 1–29.

[2] CMS collaboration, *"Observation of a new boson at a mass of 125 GeV with the CMS experiment at the LHC"*, Physics Letters B **716** (2012) 30–61.

[3] L. Guan, *Trigger algorithms and electronics for the ATLAS muon new small wheel upgrade*, Journal of Instrumentation **11** (2016) C01083, `http://stacks.iop.org/1748-0221/11/i=01/a=C01083`.

[4] T. Alexopoulos et al., *A spark-resistant bulk-micromegas chamber for high-rate applications*, Nucl. Instr. and Meth. A**640** 110–118.

[5] V.Smakhtin et al., *Thin Gap Chamber upgrade for SLHC: Position resolution in a test beam*, Nucl. Instr. and Meth. A **598** (2009) 196–200.

[6] J. Jaeckel and A. Ringwald, *The Low-Energy Frontier of Particle Physics*, Ann. Rev. Nucl. Part. Sci. **60** (2010) 405–437, `arXiv:1002.0329`.

[7] J. D. Bjorken, R. Essig, P. Schuster, and N. Toro, *New Fixed-Target Experiments to Search for Dark Gauge Forces*, Phys. Rev. **D80** (2009) 075018, `arXiv:0906.0580 [hep-ph]`.

[8] S. N. Gninenko, *Search for MeV dark photons in a light-shining-through-walls experiment at CERN*, Phys. Rev. **D89** (2014) 075008, `arXiv:1308.6521 [hep-ph]`.

[9] G.Mikenberg et al., *Thin-gas gap chambers for hadronic calorimetry*, Nucl. Instr. and Meth. A **265** (1988) 223–227.

[10] The LEP Collaboration, *Precision Electroweak Measurements on the Z Resonance*, Phys. Rep. **427** (2006) 257–454.

[11] S.Majeski, *A Thin wire chamber operating in a high multiplication mode*, Nucl. Instr. and Meth A **217** (1983) 265–271.

[12] W. Blum, *Particle Detection with Drift Chambers*. Springer, 2008.

[13] Garfield++, *Project web page*, `http://garfieldpp.web.cern.ch/garfieldpp/`.

[14] R. Veenhof, *GARFIELD, recent developments*, Nucl. Instr. and Meth. A **419** (1988) 726–730.

[15] F.Sauli, *Principle of operation of multiwires proportional and drift chambers*. CERN, 1977.

[16] *sTGC construction's manual*, `https://edms.cern.ch/document/1399978/1`.

[17] *Mini-X Gun Datasheet*, `http://www.amptek.com/pdf/minix.pdf`.

[18] GIF++, *The new Gamma Irradiation Facility*, `https://espace.cern.ch/sba-workspace/gifpp/`.

[19] O.Sasaki et al., *ASD IC for the thin gap chambers in the LHC ATLAS Experiment*, IEEE Transactions on Nuclear Science **46** (1999) 1861–1864.

[20] G. Vasquez, S. Kuleshov, G. Mikenberg, P. Ulloa et al., *Performance of a full-size small-strip thin gap chamber prototype for the ATLAS new small wheel muon upgrade*, Nucl. Instr. and Meth. A **817** (2016) 85–92.

[21] M. J. et al, *A new irradiation facility to test large-area particle detectors for the high-luminosity LHC program*, International Conference on Technology and Instrumentation in Particle Physics (2014).

[22] T. Petrovič, M. Vencelj, M. Lipoglavšek, R. Novak, and D. Savran, *Efficient Reduction of Piled-Up Events in Gamma-Ray Spectrometry at High Count Rates*, IEEE Transactions on Nuclear Science **61** (2014) 584–589.

[23] C. Lian, L. Futian, L. Yuzhe, L. Feng, and J. Ge, *A FPGA-based pulse pile-up rejection technique for the spectrum measurement in PGNAA*, pp. , 1–3. June, 2016.

[24] NA64 Experiment, *Search for dark sectors in missing energy events*, `https://na64.web.cern.ch`.

[25] [NA64 Collaboration], *Search for Invisible Decays of Sub-GeV Dark Photons in Missing-Energy Events at CERN SPS*, Physical Review Letters **118** (2017) 011802.

[26] A. Andreas et al., *Proposal for an Experiment to Search for Light Dark Matter at the SPS*, CERN-SPSC-2013-034 **SPSC-P-348** (2013) 011802, arXiv:1312.3309.

[27] *SPS beam lines*, `http://cern.ch/sba`.

[28] S. Gninenko and N. Krasnikov, *The K_L invisible decays as a probe of new physics*, Physical Review D **92** (2015) .

[29] S. Gninenko, *Search for invisible decays of π_0, η,η', K_S and K_L: A probe of new physics and tests using the Bell-Steinberger relation*, Physical Review D **91** (2015) 015004.

[30] F. A. Cherry J. F. and S. I. M., *Neutrino Portal Dark Matter: From Dwarf Galaxies to IceCube*, arXiv: 1411.1071[hep-ph] (2014) .

[31] B. Brahmachari and A. Raychaudhuri, *Kinetic mixing and symmetry breaking dependent interactions of the dark photon*, Nuclear Physics B **887** (2014) 441 – 455, http://www.sciencedirect.com/science/article/pii/S0550321314002715.

[32] J. D. Bjorken, R. Essig, P. Schuster, and N. Toro, *New fixed-target experiments to search for dark gauge forces*, Phys. Rev. D **80** (2009) 075018, https://link.aps.org/doi/10.1103/PhysRevD.80.075018.

[33] D. Banerjee, P. Crivelli and A. Rubbia, *Beam Purity for Light Dark Matter Search in Beam Dump Experiments*, Adv. High Energy Phys. **105730** (2015) .

[34] e. a. J. Badier, Ph. Busson, *Shashlik calorimeter Beam-test results*, Nucl. Instr. and Meth A **348** (1994) 74–86.

[35] W. Busza, M. Chen and D. Luckey, *Application of synchrotron radiation for the identification of electrons in high energy beams*, Nucl. Instr. and Meth. **105** (1972) 613.

[36] J. S. Dworkin et al, *Electron identification using a synchrotron radiation detector*, Nucl. Instr. and Meth. A. **247** (1986) 412.

[37] R. Cryttenden, *Synchrotron radiation detector for tagging electrons*, Nucl. Instr. and Meth. A **276** (1989) 643–646.

[38] S. Gobain, *BGO Bismuth Germanate*, http://www.crystals.saint-gobain.com/products/bgo.

[39] [NA64 Collaboration], *High purity 100 GeV electron identification with synchrotron radiation*, Nucl. Instr. and Meth. A. **866** (2017) 196–201.

[40] S. Gobain, *Prelude 420 LYSO*, http://www.crystals.saint-gobain.com/products/prelude-420-LYSO.

[41] *LYSO data sheet, PreLude 420, Saint-Gobain*, http://www.crystals.saint-gobain.com/products/prelude-420-LYSO.

[42] *MPPC (multi-pixel photon counter), HAMAMATSU*, http://www.hamamatsu.com/us/en/community/mppc/index.html.

[43] *COMPASS Experiment*, http://wwwcompass.cern.ch/.

[44] A. Král and T. Liška, *COMPASS: New hadron run in the view of COOOL*, Czechoslovak Journal of Physics **55** (2005) A375–A381, https://doi.org/10.1007/BF03032025.